UNIVERSIDAD NACIONAL DE COLOMBIA

Exploring Dirac Materials and Two-Dimensional Magnet Using Green's Function Method and Quantum Magnetic Imaging

Jeyson de Jesús Támara Isaza

Universidad Nacional de Colombia
School of Science, Physics Department.
Bogotá D.C., Colombia
2023

Exploring Dirac Materials and Two-Dimensional Magnet Using Green's Function Method and Quantum Magnetic Imaging

Jeyson de Jesús Támara Isaza

Master's thesis proposal in compliance with a partial requirement to opt for the title:
Master in Science - Physics

Supervisor:
Wiliam Javier Herrera Ph.D.
Universidad Nacional de Colombia
Co-Supervisor:
Mark Jen-Hao Ku Ph.D.
University of Delaware

Universidad Nacional de Colombia
School of Science, Physics Department.
Bogotá D.C., Colombia
2023

Abstract

Thesis Title: *Exploring Dirac Materials and Two-Dimensional Magnet Using Green's Function Method and Quantum Magnetic Imaging*

The development of techniques and methods, from an experimental and theoretical view, to explore condensed matter systems is crucial to reveal the distinguishable features of their electronic or magnetic properties, characterize them and in this way uncover, understand, and control the footprint of exotic collective phenomena, novel quantum phases of matter, among others and in this way then further use them for specific technological application and/or to ground the foundational basis of condensed matter physics. Interestingly, many promises in quantum technological applications and novel exotic phenomena as well as quantum phases of matter have as a platform the very rich family of two-dimensional material, Some interesting phases that have been or it is predicted to be observed are quantum spin liquid, topological quantum phases, skyrmion textures, etc. In light of the aforementioned claims, our work presents several novel theoretical and experimental approaches to studying different types of condensed matter phases and properties in a wide range of materials but focuses on the family of graphene-like and Van der Waals (VdW) materials.

First, in our work we have been able to develop a novel Green function method for a microscopic generalized Dirac Hamiltonian to study quantum transport properties in physical systems such as topological insulators, cuprate superconductors, Weyl semi-metal, but in particular we applied the method for graphene-like materials. The technique accounts for the main physical system's properties, i.e. spin-orbit coupling, valley-spin coupling, intrinsic gap, external fields, etc., the specific edge condition of the system, and system size. These permit the exploration of exotic phenomena and phases from relevant materials such as Transition Metal Dichalcogenide (TMDs), Germanene, and Silicene by calculating quantities such as local density of states (LDOS), density of states, and scattering process, among others. Using this new approach, we find analytical and closed-form expressions that allow us to make low computational cost numerical calculations that determine a rich variety of phenomena. Some of them that we would like to highlight are the valley-dependent properties of the TMDs scattering process, the evident spin-valley locking electronic state distribution of this type of system, as well as the presence of concentrated edges state product of specific boundary conditions; from the Germanene and Silicene side, we find that they behave as a topological insulator in normal conditions but in particular that their topological properties are independent of specific edge condition over both system and by tuning a perpendicular external field their topological properties remains robust but beyond some critical field the system starts to behave as normal insulator. Our particular calculation paves the way for applications of TMDs as monolayer transistors or for valley-selective excitonic devices and on the other hand, in Germanene and Silicene, our results contribute to the use of them as topological field effect transistors or for effective magnetic to electric transfer in spin-torque

ferromagnetic resonance technique, to mention a few of the interesting impacts of our results for the specific application of our technique in this manuscript.

Secondly, a recently popular experimental method for magnetometry based on spin defect in diamond called quantum magnetic imaging (QMI) with nitrogen-vacancy (NV) centers in diamond has been implemented to study FGT and Co-doped FGT ultrathin VdW magnetic samples. Our method takes advantage of the NV center ensemble working as a local sensor; when the NV center is in resonance with a lab-controlled microwave (MW) field and an external target field from our sample, it allows us to detect optical emission changes of each local sensor next to the sample by capturing pixel by pixel light emitted by the spins, with it we get a map of the samples field. Then by appropriately magnetizing the VdW ultrathin films with a bias field, we are able to determine their magnetic phase at room temperature. Through our technique, we are able to reveal that FGT and Co-doped FGT present ferromagnetism at room temperature, and that our method allows us to screen multiple samples and find ferromagnetism in samples as tiny as 7 unit cells. Our results reveal that this type of VdW magnet has relevant thickness for spintronics devices and extends the portfolio of materials with ferromagnetic phase in that scale. Alongside this method, we develop a new modality of magnetometry based on NV center, all-optical and microwave-free at low field regime. Our new technique relies on two approaches, first the development of an experimental setup that can measure the photoluminescence emission from an NV ensemble when the magnetic field is systematically tuned and oriented in a desire orientation and second a proper model for simulating the fluorescence spectrum that accounts hyperfine coupling, quadrupolar interaction, and for interacting NVs with other defect centers in ensembles. The findings from our experimental and theoretical results show the relevant impact of spin cross-relaxation processes in the improvement of the method's sensitivity, the role that plays linear polarized light in the fluorescence and the importance of the NVs crystal plane orientation with respect to the magnetic field. Our results are promising for future exploration of VdW materials at cryogenic temperature and further understanding of the relevant physics that influence in the proposed new magnetometry modality at low magnetic field.

Finally, at the end of the document, we draw approaches where the aforementioned methods could complement each other and be used jointly to explore condensed matter systems of interest, and we describe how using some findings and insights from one method can be used in the other one to further understand and explore the object of study of interest.

Keywords: Green Function, Nitrogen-Vacancy center in diamond, Quantum Magnetic Imaging, All-optical Magnetometry, Dirac Hamiltonian, Graphene-like materials, VdW Materials .

Resumen

Título de tesis: *Exploración de materiales de Dirac e imanes bidimensionales usando el método de las funciones de Green e imágenes magnéticas cuántica*

El desarrollo de técnicas y métodos, desde un punto de vista experimental y teórico, para explorar los sistemas de materia condensada es crucial para revelar los rasgos distinguibles de sus propiedades electrónicas o magnéticas, caracterizarlos y de esta manera descubrir, comprender y controlar la huella de fenómenos colectivos exóticos, nuevas fases cuánticas de la materia, entre otros, y de esta manera utilizarlos posteriormente para aplicaciones tecnológicas específicas y/o para fundamentar las bases de la física de la materia condensada. Curiosamente, muchas promesas en aplicaciones tecnológicas cuánticas y fenómenos exóticos novedosos, así como fases cuánticas de la materia, tienen como plataforma la riquísima familia de materiales bidimensionales. Algunas fases interesantes que se han observado o se prevé observar son el líquido cuántico de espín, las fases cuánticas topológicas, las texturas de skyrmion, etc. A la luz de las afirmaciones anteriores, nuestro trabajo presenta varios enfoques teóricos y experimentales novedosos para estudiar diferentes tipos de fases y propiedades de la materia condensada en una amplia gama de materiales, pero se centra en la familia de materiales similares al grafeno y Van der Waals (VdW).

En primer lugar, en nuestro trabajo hemos sido capaces de desarrollar un novedoso método de función de Green para un Hamiltoniano de Dirac microscópico generalizado con el fin de estudiar las propiedades de transporte cuántico en sistemas físicos tales como aislantes topológicos, superconductores cupríticos, semimetales de Weyl, pero en particular hemos aplicado el método para materiales similares al grafeno. La técnica tiene en cuenta las principales propiedades del sistema físico, es decir, el acoplamiento espín-órbita, el acoplamiento valle-espín, la gap intrínseco, los campos externos, etc., la condición de borde específica del sistema y el tamaño del sistema. Esto permite explorar fenómenos y fases exóticas de materiales relevantes como los dicalcogenuros de metales de transición (TMDs), el germaneno y el siliceno mediante el cálculo de cantidades como la densidad local de estados (LDOS), la densidad de estados y los proceso de dispersión, entre otros. Utilizando este nuevo enfoque, encontramos expresiones analíticas y de forma cerrada que nos permiten realizar cálculos numéricos de bajo coste computacional que determinan una rica variedad de fenómenos. Algunos de ellos que nos gustaría destacar son las propiedades valle-dependientes del proceso de dispersión de los TMDs, la evidente distribución de estados electrónicos spin-valley locking de este tipo de sistemas, así como la presencia de estados de bordes concentrados producto de condiciones de borde específicas; por el lado del Germaneno y el Siliceno, encontramos que se comportan como un aislante topológico en condiciones normales pero en particular que sus propiedades topológicas son independientes de la condición de borde específica sobre ambos sistemas y al sintonizar un campo electrico externo perpendicular, sus propiedades topológicas permanecen robustas pero más allá de cierto campo

crítico el sistema comienza a comportarse como un aislante normal. Nuestro cálculo particular allana el camino para aplicaciones de TMDs como transistores monocapa o para dispositivos excitónicos selectivos de valle y por otro lado, en Germaneno y Siliceno, nuestros resultados contribuyen al uso de ellos como transistores topológicos de efecto de campo o para la transferencia efectiva magneto-electrica en la técnica de resonancia ferromagnética de spin-torque, por mencionar algunos de los impactos interesantes de nuestros resultados para la aplicación específica de nuestra técnica en este manuscrito.

En segundo lugar, se ha implementado un método experimental recientemente popular para la magnetometría basada en el defecto de espín en el diamante denominado imagen magnética cuántica (QMI) con centros de vacantes de nitrógeno (NV) en el diamante para estudiar muestras magnéticas VdW ultrafinas de FGT y FGT dopado con Co. Nuestro método aprovecha el conjunto de centros NV funcionando como un sensor local; cuando el centro NV está en resonancia con un campo de microondas (MW) controlado en laboratorio y un campo objetivo externo de nuestra muestra, nos permite detectar cambios de emisión óptica de cada sensor local próximo a la muestra capturando píxel a píxel la luz emitida por los espines, con ello obtenemos un mapa del campo de las muestras. A continuación, magnetizando adecuadamente las películas ultrafinas VdW con un campo de polarización, somos capaces de determinar su fase magnética a temperatura ambiente. Mediante nuestra técnica, somos capaces de revelar que las FGT y las FGT dopadas con Co presentan ferromagnetismo a temperatura ambiente, y que nuestro método nos permite estudiar múltiples muestras en una sola medición y encontrar ferromagnetismo en muestras tan pequeñas como 7 celdas unidad. Nuestros resultados revelan que este tipo de imán VdW tiene un grosor relevante para los dispositivos de espintrónica y amplía la cartera de materiales con fase ferromagnética en esa escala. Junto a este método, desarrollamos una nueva modalidad de magnetometría basada en el centro NV, totalmente óptica y sin microondas en régimen de campo magnético bajo. Nuestra nueva técnica se basa en dos enfoques, en primer lugar el desarrollo de un montaje experimental que puede medir la emisión de fotoluminiscencia de un conjunto de NV cuando el campo magnético se sintoniza sistemáticamente y se orienta en una orientación deseada y, en segundo lugar, un modelo adecuado para simular el espectro de fluorescencia que tiene en cuenta el acoplamiento hiperfino, la interacción cuadrupolar y la interacción de los NV con otros defectos. Las conclusiones de nuestros resultados experimentales y teóricos muestran el impacto relevante de los procesos de relajación cruzada de espín en la mejora de la sensibilidad del método, el papel que juega la luz polarizada lineal en la fluorescencia y la importancia de la orientación del plano cristalino de los NVs con respecto al campo magnético. Nuestros resultados son prometedores para futuras exploraciones de materiales VdW a temperatura criogénica y para una mayor comprensión de la física relevante que influye en la nueva modalidad de magnetometría propuesta a bajo campo magnético.

Por último, al final del documento, trazamos enfoques en los que los métodos mencionados podrían complementarse y utilizarse conjuntamente para explorar sistemas de materia condensada

de interés, y describimos cómo el uso de algunos hallazgos y conocimientos de un método puede ser utilizado en el otro para comprender y explorar más a fondo el objeto de estudio de interés.

Citations to previously published work

Part of this master thesis covers research reported in the following articles:

1. *"Microscopic Green's function approach for a generalized Dirac Hamiltonian"* **Jeyson Támara-Isaza**, Pablo Burset, and William J. Herrera. In preparation.

2. *"Above-Room-Temperature Ferromagnetism in Thin van der Waals Flakes of Cobalt-Substituted Fe5GeTe2"* Hang Chen, Shahidul Asif, Kapildeb Dolui, Yang Wang, **Jeyson Támara-Isaza**, V. M. L. Durga Prasad Goli, Matthew Whalen, Xinhao Wang, Zhijie Chen, Huiqin Zhang, Kai Liu, Deep Jariwala, M. Benjamin Jungfleisch, Chitraleema Chakraborty, Andrew F. May, Michael A. McGuire, Branislav K. Nikolic, John Q. Xiao, and Mark J. H. Ku. ACS Application Material Interfaces - January 2023

3. *"Revealing room temperature ferromagnetism in exfoliated Fe5GeTe2 flakes with quantum magnetic imaging"* Hang Chen, Shahidul Asif, Matthew Whalen, **Jeyson Támara-Isaza**, Brennan Luetke, Yang Wang, Xinhao Wang, Millicent Ayako, Andrew F. May, Michael A. McGuire, Chitraleema Chakraborty, John Q. Xiao, and Mark J.H. Ku. IOP 2D Materials - March 2022

Internships related to this work

Part of this master thesis is research developed during the following internship.

Chapter 3 of this thesis was done at the University of Delaware in the United States:

- *Summer Research Program at the Universidad of Delaware*. In the framework of the cooperation in between National University of Colombia and University of Delaware (UD) to student exchange to UD I was selected to make an internship at the Physics and Astronomy Departmenet working with the Prof. Dr. Mark Ku at the quantun matarials and engineering (QME) group from July to December of 2021.

- *Visiting graduate researcher invited by QME*. Following sucessful internship in 2021, Prof. Dr. Ku invited me to keep working in the related project from June to September of 2021 funded by the QME group

Chapter 4 of this thesis was done at the University of Maryland, College Park in the United States:

- *Visiting graduate researcher invited by Walsworth Group*. Invitation from Prof. Dr. Ronald Walsworth at the University of Maryland (UMD) to work in the quantum technology center (QTC) from October 2022 to April 2023 funded by Walsworth Group. Following sucessful internship in previous months at UMD, Prof. Dr. Walsworth invited me to keep working in the related project from July 2023 to October 2023.

Acknowledgments

Before joining the master program, I had many doubts about if it was worth it for me to try physics seriously as a way of living, the joy at the early years of the undergrad program disspeared at the time I ended it, losing the sense of meaning of what I was doing not just with my career but with my own life, which make me wonder if there was a point in keep trying something with physics. So far the master have been a challenging, rewarding, transformative and life changing experience which has showing me that I have in my hands the capability to be as succesfull as I decide to be, not just as a physicists but as a person. All the knowledge and lessons I have learnt in the last years that allow me to reach these conclusions are thanks to a group of people that will be highlighted in the following paragraph, however before I start, I truly believe that my words will not capture the real impact all of them have in my life.

Initially, I want to thank to my more recent supervisor Prof. Dr. Ronald Walsworth (Ron) for allowing me be part of his beautiful research team at the University of Maryland in the United States. A group of people who as a scientists are clever, collaborative and hardworkers, but as individuals are beyond fantastic, truly special human beings with a welcoming, positive and warming attitude. Ron through his general thoughts in group technical meeting and personal conversations have teaching me the views, approach and perspective in big leagues of science, this lessons about how science is made at the cutting edge have changed for good the views I have as a physicists. Also, I want to thank you Ron, for your comment on your different views about the possible application and impact of my project, your thoughts were valuable to dimension the real meaning of my work which motivates the chapter four of this thesis. Finally, I want to express my gratitude to Ron for always find a spot in his busy schedule to chat with me about future career plans and motivates my profesional goals with advices, recommendations and his support of every type.

I want to thanks to someone who opens me the door to work in experimental physics and filled me with trust in my skills to succeed as a researcher,Prof. Dr. Mark Ku, who I work with at the University of Delaware. Mark, in many ways contributed in my scientific but also in my personal life, through his support, advices and comment about questions of different matter, He was able to make a significant change in my life that my words of gratitude are not enough, thanks Mark. I want to thank Mark for all his help in this years, for recommend me with Ron, for pick me up in the list of candidate in the summer program 2021 at UD, for make me feel a valuable member of his recent new team at UD, for invite me again to re join the group in 2022 and for being my advisor during this thesis, all this things and many others were moments that reinfornced in myself a positive self-image that has boost my career to a point I never will reach without his encouragament. Finally, I want to thanks Mark for allowing me be part of several projects which made possible the third chapter of this thesis where I were able to explore and learn about the exciting field of quantum sensing with nitrogen vacancy centers applied to condensed matter

systems.

Now is the time to express my gratitude to my priceless advisor, Prof. Dr. William Javier Herrera from National University of Colombia. William since we started to work together have expressed his trust in my capacity as theoretical physicists and have nurture it by motivating my curiosity and wide range of interests through my whole career since undergrad, this have filled me of the confident to address the projects were I have been part of. In particular about the master program, William have encourage me to pursue and explore experimental and theoretical physics in parallel in the context of condensed matter physics. He always have making me think in ways where both approach can be complementary and enrich each other but mantaining common purposes, helping me in this way to make research with meaning. I thanks William for all the time have expended explaining me details about theoretical aspects of our work together, as well as strenghting our relationship by talking of topics beyond the projects, such as career path, future research projects for the group, plans for the future, and so on. I want to thanks William for including me in the project that motivate the chapter two of this thesis and for introduce me to Prof. Dr. Pablo Burset, both were fundamental in the interpretation of the numerical simulation results, and for the countless meeting to discuss about the progress of the project, all our effort have come to the realization of this document and a paper that soon will see the light. Beyond all this project and research related gratefullness, I want to extend to a bit more thank you to william for his relentless patience, guidance and help in all matters during my life at the university at the academic, administrative and personal level.

During the master I have met people who have made the research experience more rich, smooth and fun. To start with I want to thank to the people I met at University of Delaware. I want to thanks Shahidul Asif (Shah), PhD student at Ku's group, who with his natural engineering skills help me to debug many different problems related with coding, set up building as well as explaining me many fundamental steps in the measurement process in the lab, his help make the transition to the experimental side of physics much more easier to me and his kindness and assistance in different personal matters make my life at the USA at the beggining simpler for me. In addition I want to thanks to Hang Chen for his significant contributions to my work when working at Ku's lab. In addition I would like to thanks the people from Colombia I met at the Innternationale House, Felipe Reyes, Jalil Varela, Federico García, Julietta Mendivelso, Luis Herrera, Kenneth Rueda, Jose Falla, Sasiri Vargas and Tatiana Acero for their friendship, support and the sense of family we build at the Inn, thanks for bring to the internships so much fun and for being so supportive in key moments; to the international community at the Inn, Yuriy, Ali, Romain, Sudipta, Kaneil, Randy and many others who I find them as an international family who help me in many aspects living in Newark, which enriched the ways I see the world and make my time there very pleasant.

During the time I have been in the University of Maryland, I have had the luck to work with very

talented graduate students and posdocs that with the time have become something more than colleague but friends. To start with I would like to thanks to Xiechen Zheng (Chen), who allow me to work alongside with him in the all-optical quantum diamond magnetometer (AO-QDM) project, for mentoring me all this time, his guidance and support through the needed steps to make progress in the project was vital to have several milestons during the execution of the project. I believe that his skillfull capabilities as engineer and his clever physical intuition contributed hugely to the solution of the several obstacles we found during the projects execution, for all this thank you; in addition I want to thanks Chen for considering my thoughts and suggestion in many stages of the project, as well as giving me leadership in the Low-field AO-QDM side project that motivates the chapter four of this thesis; finally, I want to thanks Chen for be such a good friend during the time working together. In addition I want to thanks to others members of the AO-QDM team, Kristine Ung, John Blanchard, Paul Petruzzi and Connor Hart. To Paul Petruzzi and Kristine Ung for their thoughts and discussions during or group meetings. To John Blanchard thanks for allowing us using his Low-field NMR setup for the purpose of the Low-field AO-QDM project and for his several thoughts about electronics and use of several equipments needed for this project. To Connor Hart thanks for value and take into account many of my thoughts during our group meetings as well as his many advices about ways to overcome set backs during the project; I want to thanks Connor for be more a friend than a posdoc and have such a good vibe when talking to me about matters beyond science. Finally, I want to thanks Jner Tzern (JJ) Oon for valuable theoretical discussions that leads to many important results in the theoretical side of the Low-field AO-QDM project, without his thoughts and valuable physics conversations it was not be possible to get such as promising findings in our model; in addition I want to thanks JJ for his friendship and for all the great conversation about physics and differents topics we have had.

To wrap out how grateful I am with several people at Maryland. I would like to thanks they for being so welcoming, warm and make me feel part of the group in a short period the time to Reza Ebadi, Saipriya Satyajit, Kristine Ung, Smriti Bhalerao, Jiashen Tang, Zechuan Yin, Isaiah Villanueva, Lakshmi Kumar, JJ Oon and Chen, they frequenly hanged out with me on the weekends, always we had great conversations at the dinning hall or in lab, after work hours always we had extra time to have fun together, among many other things that each of them individually made for me that meaned a lot, for all that thank you guys.

During this journey have been timeless people who has been always for me that I want to thanks to them for their unconditional support. To start with I would like to thanks to Arnobio Rivera, Leyda Contreras and Manuela Rivera, my second family, who always have a spot in their house. They support me in many difficult moments during this experience and make my life a lot easier in many ways with their help, for that thank you so much. I am in gratitude with Arnobio and Leyda for make me feel part of their family in such a warming and welcoming way, for don't hesitate in any momement were I required help and for being so special with me from the beginning.

I would like to thank to my family, my dad Adelson, my mom Dubis, my siblings Andrés, Jesús and Marianella, my nieces Emma and Luciana, and my extended family Cruz Marina, Danna and Carla; their prescence, support and their spirit have been always present in my life when I have been away from hometown and count with their open arms always when I am back have been so recharging and motivating in many ways that have helped me to make it to this point. In particular I thanks my Mom for her infinite support, for believe in me in every moment even when she was not aware of exactly what I was doing and for show complete trust in my decisions even if they implied difficulties for my life at the short term, thanks for being so supportive and helpful, I am glad to be son of such a great women which with her attitude to life have taught me to many lesson beyond words, my words of gratitudes never will be enough to thank you for the unmessurable impact you have had in my life; I am really happy that during the time of the master I had lived again several times in home with you to exchange many experience and many thought, getting to know each other again not just as son and mom, but as friends. I would like to thanks to Andrés and Jesus for being so supportive and for their encouragement all this years, for make me feel part of their life so easily when I was back to home by inviting to play football, take a few drinks and have some fun together as brothers; better brothers and friend I couldn't ask to life, you are my forever best friends. Finally I want to thanks to the one who with his memory has been a huge inspiration for me, my dad Adelson, who unfortunately pass away when I was starting my master program due to COVID-19, his spirit, lessons, thoughts and memory have been my great company in many moment of solititude and in many other of joy in the last years and had give me the strength that I needed in many moments to overcome difficulties; I really hope that wherever you are, you can see that your legacy still alive in my actions and that all what you were in life is resonating loud in the life of all what we love you, we never ever will forget you. I hope you have been enjoying the little victories I have been getting in the years since you left, we miss you so much and we love you every day more.

Last but not least, I want to thanks to my beloved and wonderful partner: Leyda Juliana Rivera Contreras, I don't know if a life together will be enough to tell you all the reasons why I love you and why I am so grateful for having you in mine, thank you for always being with me. Thanks for this journey together full of love, trips, physics, interesting conversations, fun, experiences and more, this time together have been beyond any of my more happiest and wildest expectations or dreams. But to name a few specific things that I want to thanks you, thanks for waiting for me everytime I was far away from you and to enjoy so happily when we were close, thanks for the uncountable times we overcome not being together by calling us through WhatsApp to talk about our days meanwhile we were resting, learning that being together is a feeling and not a physical condition, thanks for always encourage me to give the best of me not just as a physicists but as a person, thank you for engage with me in many discussion about our research areas in physics (yes, so technical but too worth to mention), thanks for enjoy my cooking and share yours with me, thanks for giving me the best months of my life when we lived together

in the USA, thanks for walk next to me in the darkest paths we have found in our relationship (figuratively and literally) and trust that every will go good as long as we are next to each other; Thanks for being so virtuous, loving, charming, kind, wise, funny, and active listener and for your patience, just to mention a few of your qualities that make me feel so grateful for having you in my life. Talking about my master's program is summarized by remembering specific moments of our relationship and how you played a vital role in my success in this year, that's why just writing a paragraph of acknowledgment to you is not enough to express all my gratitude. I am happy and grateful to God (or whatever governs life) that at the moment I am writing this acknowledgment section, we have got to the point to start planning our wedding, that we have got to the point to be about to have start another chapter of our story in Australia with me having a new job and you pursuing your dream of doing a master overseas; that we are just about to have the life that we working hard for in many nights to get done our duties for the university while wishing that all that effort ends in a better life for us; I am glad that we have achieved this stage and that we can start planning our life together with happiness because everything in which we sacrifice ourselves as individuals and as a couple is paying off. I really wish that our new journey starts soon to have much more fun, experiment with life together, and navigate it with the patience, understanding, and love that have always characterized us. I couldn't ask life and God for a better partner in crime, colleague, friend, lover, girlfriend, soulmate, and future wife than you, I am so happy and blessed to have you. Thank you for everything Juliana, I love you.

Acknowledgments of Financial Support

First of All I would like to thanks the Physics Deparments from the School of Science of Universidad Nacional de Colombia to their financial support during my master studies by the scolarship "Beca Auxiliar Docente" during the semesters of 2021-II and 2022-I. In addition I want to thanks Universidad Nacional de Colombia and University of Delaware for their financial support during the summer internship program in 2021-II and to Prof. Mark Ku financial support during the internship in 2022-II with the National Science Foundation Project with award number 2203829. Also I would like to thanks Prof. Walsworth from the University of Maryland for their financial support from the project "All optical quantum diamond magnetometer for high magnetic field" during the internship program to made possible the chapter four of this thesis during 2022-II and 2023-I. Finally I would like to express my gratitude to Prof. William Herrera for his financial support through the project "Reflexiones no locales de Andreev en sistemas topologicas" with number 202010027542 and "Centro de excelencia en tecnologías cuánticas y sus aplicaciones a metrología" with number 205010039944 during 2022-II and 2023-I.

Contents

1 Introduction

In the last thirty years, condensed matter physics has been enriched by the discovery of a wonderland of exotic quantum matter phases (QMP). These QMP come from emergent or collective states of interacting particles, that are nothing like the solids, liquids, and gases of common experience, as well as a massive increase of the two-dimensional (2D) material's family since graphene first-time fabrication, the set of all this kind of phases of matter are the so-called quantum materials (QM). Boosted by the current new nanotechnology revolution driven by quantum computers, quantum materials have been exploited and explored with the goal of developing and creating the technology that will drive the world of tomorrow.

To highlight the interplay between QM and progress in quantum devices, let's consider specific cases such as topological insulators(TI) and quantum spin hall effect phases, topological superconductivity, and quantum spin liquid which are related to some of the families that belong to the current research in classify all phases of matter with topological numbers [1].

To start with, let us talk about the quantum spin hall effect (QSHE) predicted by B. A. Bernevig et Al in 2005 [2] without the need for an external magnetic field purely given by the high spin-orbit coupling, which was experimentally observed in HgTe quantum wells in 2007 [3] by doing hall resistance measurements at cryogenic temperatures. Then in 2014 [4] was predicted that 2D transition metal dichalcogenides (TMDs) are platforms to observe QSHE and useful building block for a topological field effect transistor, more recently was proved that at 100 K in a monolayer of TMDs measuring edge conductance [5].

A more striking fact is the intrinsic connection between QSHE and topological insulators (TI), both phenomena can be described by the Chern number or topological invariant reproducing the exact same physics, reason because each one is the synonym of the other [6]. Topological insulators were predicted and observed in 3D materials such as Bi_2Te_3, Bi_2Se_3 and $Bi_{1-x}Se_x$ using ARPES measurements of surface electronic band dispersion state, showing in this way Dirac cones at the surface at the QSHE state [7, 8, 9]. In addition, using TI Bi_2Se_3 at room temperature in 2014 was demonstrated that it provides a strong spin-orbit-transfer torque to a magnetic material, showing efficient electrical manipulation of magnetic materials useful for memory and quantum information applications. Afterward have been demonstrated giant spin orbit torque (SOT) using different TIs and reinforcing their utility as a promising material for spintronics applications [10, 11]. In addition to 3D TIs, 2D TIs have been predicted in graphene [12] however

due to their low spin-orbit coupling are less exciting than almost all the sub-family of 2D materials which are known as graphene-like materials, such as stanene, silicene, germanene, among others, are excellent platforms for TIs and for quantum anomalous hall effect (QAHE) due to their relative high-spin orbit coupling respect graphene [13].

An elusive topological state with promising groundbreaking application in quantum topological computation and fundamental physics is the topological superconducting state dominated by bound edges states called Majorana Fermions, a particle that is its own anti-particle which has been extensively hunted in particle physics [14]. The realization of this material has been initially predicted to be possible in the interface between of an s-wave superconductor and a topological insulator with strong SOC by Liang Fu and C.L. Kane [15]. Despite the effort in the community to demonstrate this topological state in this hybrid system [16, 17, 18], it is still unsuccessful because of the difficulty to distinguish between Andreev bound states and Majorana zero modes at the edge of this kind of material[19], given that both phenomena give rise to zero peak voltage, the principal landmark to prove TS; however, now the community, leading by Microsoft itself, have focused their research in the development of protocols to test several signatures of TS and not just zero peak voltage at the edge of the interfaces [20].

In the meantime, also twisted bilayers of graphene have been predicted to have topological superconductivity as well as TMDs, confirming how 2D materials are an excellent playground to many types of QMP [21, 22]. One of the main applications for TS as mentioned previously is related to QIS, due to their topologically protected states this assures an improvement in coherence time that will outperform current technologies [23].

Finally, to summarize some of the QMP, there are also quantum spin liquids, which have currently been observed only in non-stoichiometric magnetically doped materials or in 3D layered crystals of magnetic materials, not yet exfoliated into monolayers [24]. This phase could lead to a new paradigm for high-density, low-power data storage in the context of solid-state systems[3]. It is known that 2D magnets such as CrI_3 possibly can host this phase [25] and given their properties in general 2D magnets are also suitable platforms to observe skyrmions which are statically stable topological spin textures that have been observed experimentally in this class of materials using neutron scattering techniques as well as transmission electron microscopy methods [26], these are also a particular kind of QMP for magnetic materials. So, 2D magnets are two types of different QMP with crucial impact in data storage, QIS and low-energy consumption devices [24].

Each type of QMP described so far has a broad impact on several potential technologies, however, the key factor does not correspond to the existance itself of this phase but also to the community's capability to detect and predict each of them. Primarily all of them can be measured using electric, magnetic or optical measurements techniques sensible to electric or magnetic behavior. Hence, the development of techniques and methods, from an experimental and theoretical

view, to explore condensed matter systems is crucial to reveal the particular features of their electronic or magnetic properties, characterize them, and in this way uncover the footprint of QMP. In this thesis, we describe the development and application of novel theoretical and experimental methods to the study of quantun material phases.

The 2D materials have shown that are suitable platforms for most QMP. From the theoretical perspective, the 2D materials, that have been mentioned, describe a many-particle system. The properties of these kinds of systems are mostly described from a quantum field theory perspective where Green's function is a keystone. Using Green's function it is possible to explore superconductivity, superfluidity, as well as quantum magnets in 1D and 2D, two-dimensional materials, and topological materials, from classic to more modern applications [27].

Quantities such as response functions (e.g. electric susceptibility, conductivity, magnetic susceptibility), the local density of states, and the density of states, can be described given the hamiltonian from a particular physical system with the Green's function [28]. Besides, with the Green's function for a system and by means of the Dyson equation, it is possible to do the engineering of junctions of several materials, as well as create several kinds of interfaces using this method to explore the surface's or edge's state [29]. In addition, the Green function allows identifying the scattering processes in the interface of materials, e.g. reflection coefficient, transmission coefficient, etc [30]. Regarding these quantities, it is possible to calculate several magnitudes of high interest in studying novel phase phenomena as well as modeling real physical systems. Due to the broad information that could be found using Green's function given the hamiltonian and the boundary conditions for the system, the mathematical method is suitable to explore electric and magnetic properties of any kind of condensed matter system.

On the experimental side, quantum magnetic sensing based on nitrogen-vacancy centers in diamond is a new method that has been used to explore two-dimensional magnets such as $CrTe_2$ and CrI_3 [25, 31]. Also, the viscous flow of graphene's electrons has been revealed using this technique [32], this fact allows us to think that this technique also is useful to explore current flow in devices. In addition, magneto static twists in room-temperature skyrmions have been explored by spin texture reconstruction using this method [33]. Using this experimental approach it is possible to explore key magnetic properties of 2D materials, as well as electronic properties.

Quantum sensing with NV centers in a diamond can be pictured as a spin qubit system, where the electronic spin of the two-electron from the NV presents a three-level system. When the external magnetic field is applied to the NV occurs level transitions between the levels due to the field. The fluorescence emitted by the NV allows for finding the magnitude of the magnetic field using an appropriate protocol to manipulate the whole system with an external alternating electric field. This protocol allows for identifying the frequency of the fluorescence as well as exploring a particular magnetic material with specific conditions. Besides the ensemble of NV

center in a diamond magnetometer can be considered a leading modality for sensitive, high-spatial-resolution, wide-field-of-view imaging of microscopic magnetic fields due to the wide range of conditions that it could be operated, for instance from cryogenic to well above room temperature, the narrowband detector of the magnetic field over a range of frequencies from near DC to GHz, also full vector magnetic field sensing is possible using the distribution of NV orientation along the four crystallographic direction in a diamond[34].

In this thesis, we present the development and applications of techniques based on a novel approach using Green functions method and ensembles in NV centers in diamond. The methods are particularly applied to the wide family of two-dimensional materials. We explore several electronic and topological phases in the so-called Dirac Materials, i.e. materials that obey the Dirac Hamiltonian, but focus on the family of Graphene-like materials such as Germanene, Silicene, and Transition Metal Dichalcogenides (TMDs), with the Green function method which will allow us to reveal several quantum transport properties such as local density of state, density of states and scattering process. The beauty of the mentioned graphene-like materials is that they are also part of a new class of materials called Van der Waals materials, which in short can be described as those that present perpendicular bonding between layers, these properties allow easy engineering and fabrication of devices based on the family of two-dimensional materials. The method of quantum magnetic imaging using nitrogen-vacancy centers in diamond is used to explore magnetism in magnetic Van der Waals materials with thicknesses as low as 7 unit cells thick, due to their low thickness are called 2D magnets. Finally, further development on a new modality completely based on the optical emission of NV center, is done using nitrogen-vacancy centers at a low field regime (i.e. < 30 G), the emission of the NV centers is affected by the ensemble density of NVs, this dependency is described through a theoretical model and outlooks about the possible implementation of this method to explore condensed matter system is discussed.

The meaning of this work rests in the fact that the study objects, namely two-dimensional materials, are of key interest either for fundamental physics or technological application, however even if the study objects are important themselves, the methods through which the studies are done offer new paths to explore a wide range of new materials and as well as ways to engineer and simulate devices. So the purpose of this thesis is two-fold, first, develop methods that broadly can be used for a diverse range of two-dimensional materials and beyond, and second explore phases and properties of the novel family of graphene-like materials and Van der Waals magnets. Upon this is worth mentioning that both methods are complementary in the sense that features that are predicted or described by the theoretical method offered by the newly developed Green function technique can be later detected using the NV center ensembles, but further elaboration about this point will be presented in the outlook of this document.

This thesis is organized as follows. In the next chapter, the generalized Green function method for Dirac materials is described in detail, then the method is applied to relevant graphene-like materials and an exploration of the topological phase by applying an external fields. After, quantum magnetic imaging using NV centers in diamond is briefly introduced, then a description of the sample and experimental procedure is outlined, and finally, experimental results are shown and explained. Lastly, an all-optical magnetometer based on NV centers in diamond at low field is described, a theoretical method that predicts the behavior of the sensor is presented. The experimental results exploring the effects on the fluorescence of NV centers in diamond due to the external magnetic field and compared with theoretical calculation; as an outlook, it is discussed how the method can be used to explore relevant condensed matter systems. Finally, the thesis conclusions are presented and an outlook of the interplay between methods and materials for future research is done.

2 Generalized Green's function method to explore Dirac Materials

2.1 Introduction

Condensed matter physics is having an unprecedented expansion of novel phases of matter governed by the quantum laws of nature. In the zoo of the exotic quantum phase of matter, there are several types of phenomena that at first glance look fundamentally different among them, some of them are d-wave superconductors, topological insulators, or graphene-like materials, however, despite their differences, many of these materials share low-energy characteristics like the presence of nodal points or a linear band dispersion, tunable carrier density, and high mobility due to suppressed backscattering, in the infrared regime, charge carriers follow a relativistic Dirac equation yielding the same universal behavior for, e.g., the optical conductivity or the specific heat, this class of materials are called Dirac Materials[35, 36, 37, 37, 38, 39]. .

The origin of the Dirac-like behavior varies with the material, but in all cases, some specific symmetries protect the formation of Dirac nodes in the spectrum [35]. For example, in the recently discovered quantum spin Hall insulator [40, 41] time-reversal symmetry promotes and protects the formation of Dirac-like metallic one-dimensional (1D) edge states on an otherwise 2D insulator. Similarly, three-dimensional (3D) topological insulators feature 2D edge states described by a single (or an odd number of) Dirac cones [42, 36, 43].

Particularly, two-dimensional (2D) materials have become an excellent playground to predict several exotic quantum phases such as topological insulators, d-type superconductors, topological superconductors, among others. Examples include one- or few-atom thick materials like graphene, silicene, stanene, germanene, and TMDs, all of them are Dirac materials, and their properties make them up-and-coming candidates for quantum technology applications, and an excellent platform to study novel quantum phases.

Dirac materials are characterized by their band structure, [44, 45, 46, 47], in particular, nanoribbons and junctions of two-dimensional material have motivated the use of density functional theory and wave charge techniques to explore their electronic properties [48], and new materials have been predicted from this kind of numerical methods. Once identified, their microscopic properties are more easily accessed by numerical lattice calculations CITE, which can include

finite-size effects and the presence of edges. For the study of quantum transport, it is also important to include the effect of atomic-scale interfaces, or the presence of well-defined edges in layers of 2D materials; for example, the electronic spectrum of a graphene nanoribbon strongly depends on the edge orientation[49, 50].

In a complementary approach, low-energy, effective microscopic Hamiltonians offer a way to include all these effects (finite-size, edges and interfaces, etc.), while, at the same time, providing analytical results for the study of transport, for instance, in the absence of Coulomb interactions, a scattering theory can be derived from the Dirac Hamiltonian including interesting effects like edge orientation, spin-orbit coupling, magnetization, or even superconductivity[51, 52, 53, 54, 55]. A particularly interesting generalization of effective Hamiltonians are the green function method combined with Dyson's equation [52, 50]. In the past, green's function technique has facilitated the the study of correlations (interactions, superconductivity, etc) and naturally the computation of observables like differential conductance, the density of state, scattering processes among other quantities of hybrid quantum systems based on junctions of Dirac materials[29, 30].

However, although other methods have been implemented to predict or study 2D material's electronic band structures, there is a lack of knowledge of the effects of the specific boundary conditions at the edges of nanoribbons based on graphene-like materials, for instance there is literature that predicts the presence of topological phases in nanoribbons such as Germanene, Stanene, and Silicine when their edges are zig-zag, howevers there is no experimental evidence or theoretical predictions about what will be the behavior for the case of armchair edges [13].

In this work is developed a systematic and general method to analytically compute the microscopic Green function of systems with a Dirac Hamiltonian and 2D honeycomb structure. The resulting Green function accounts for the presence of well-defined edges or interfaces at the atomic scale. We then obtain the green function of relevant examples of Dirac materials, like germanene and TMDs, and obtain transport properties (density of states and scattering probabilities) of infinite, semi-infinite, and finite layers. Our general method can distinguish specific edge orientations like zigzag, which only involves one Dirac node or valley, and armchair that combines two valleys. In all cases, the method provides simple analytical formulas.
This document is organized as follows

2.2 Brief Overview of Dirac Materials

The most basic way to characterise condensed matter physics corresponds to use the low-energy excitations, because usually, this determines the system's response to external sources. For instance, metals and semiconductors fermions are usually described by the Schröndinger Hamil-

tonian for a free particle in the free electron gas model, however for the case of semiconductors an additional term is required to consider the gap, this difference makes a fundamental change in response to temperature for each system, where for metals is linear and for semiconductors is an negative exponential. For Dirac materials the low-energy excitations are described in general by the following Hamiltonian:

$$H_D = v_F \vec{\sigma} \cdot \vec{p} + m v_F^2 \sigma_z \tag{2-1}$$

In equation 2-1, the m corresponds to the effective mass of quasiparticles, $\vec{\sigma} = (\sigma_x, \sigma_y)$ and σ_z are the Pauli matrices, the quasiparticles described by this hamiltonian are called "Dirac Fermions" [35].

Dirac fermions with non-zero mass are qualitatively different from Schröndinger ones because the positive and negative energy eigenstate of the Dirac Hamiltonian is made from the sample space of spinor wave functions, which makes that the particles and holes have the same effective mass and are interconnected through their wave functions, this is directly related to the spectral gap $\Delta = 2mv_F^2$, in the case of semiconductors or metals, holes and particles are described by different Schrodinger equations.

Material	Pseudo-spin	Energy scale
Graphene, silicene, germanene	Sublattice	$1-3$ eV
Artificial graphenes	Sublattice	$10^{-8}-0.1$ eV
Hexagonal layered heterostructures	Emergent	$0.01-0.1$ eV
Hofstadter butterfly systems	Emergent	0.01 eV
Graphene–hBN heterostructures in high magnetic fields		
Band inversion interfaces: SnTe/PbTe, CdTe/HgTe, PbTe	Spin–orbit ang. mom.	0.3 eV
2D topological insulators: HgTe/CdTe, InAs/GaSb, Bi bilayer, …	Spin–orbit ang. mom.	<0.1 eV
3D topological insulators: $Bi_{1-x}Sb_x$, Bi_2Se_3, strained HgTe, Heusler alloys, …	Spin–orbit ang. mom.	$\lesssim$0.3 eV
Topological crystalline insulators: SnTe, $Pb_{1-x}Sn_xSe$	Orbital	$\lesssim$0.3 eV
d-wave cuprate superconductors	Nambu pseudo-spin	$\lesssim$0.05 eV
^{3}He	Nambu pseudo-spin	0.3 μeV
3D Weyl and Dirac SM	Energy bands	Unclear
Cd_3As_2, Na_3Bi		

Figure 2-1: The table summarizes the materials that behave as Dirac materials. In the table, the pseudo-spin degree of freedom for each material is pointed out as well as the energy scale were they are described by the Dirac material [35]

In figure **2-1**, can be observed several physical systems that are Dirac materials, in this list several difference in between systems can be observed, for instance, the Pseudo-spin for Graphene-like materials, topological insulators, and d-type superconductors are physically different, in addition, the microscopic nature of the Dirac fermions for each of them also are.

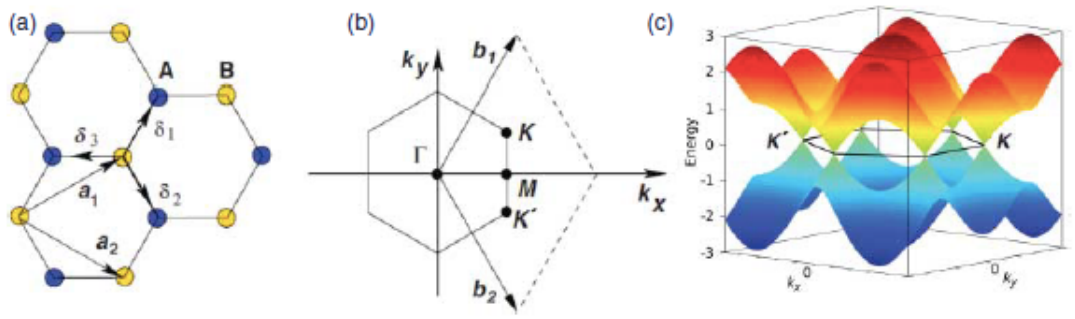

Figure 2-2: (a) Shows graphene crystal structure pointing out the two sublattices (one atoms in blue and others in yellow) (b) Reciprocal lattices of honeycomb systems. (c) Numerical simulations that shows the Dirac cones in honeycomb systems. Figure adapted from [35]

In the case of graphene each unit cell contains two carbon atoms, which give rise to two sublattices, A and B, each atom of sublattice A are surrounded by three nearest neighbors in sublattices B, as shows in **2-2A**. The system can be described by a tight-binding Hamiltonian which when are considered the first nearest neighbors and the energy spectrum is calculated around the K and K' points in the first Brillouin zone (**2-2B**),it is reduced to a hamiltonian of the form

$$H(\vec{k}) = \hbar v_F \vec{k} \cdot \vec{\sigma} = \hbar v_F \left(\tau k \sigma_x + q \sigma_y\right) \tag{2-2}$$

where $\hbar v_F = \sqrt{3} t a/2\ t \approx 2.7 eV$ and $a = 1.48$is the hopping constant and the relative distance in between C-C atoms, respectively. In figure (**2-2C**) can be clearly observed numerical calculations of Dirac cones around the inequivalent K and K' points.

In graphene, there are two spin degenerate cones in each of the two valleys, and the speudo spin corresponds to the sublattice degree of freedom. The Dirac fermions in graphene are derived from the electronic band structure and are thus charged quasiparticles[56].

In the case of a topological insulator, they have a strongly spin-orbit coupling with an insulating bulk but conducting surface states. In topological insulators the bands are separated by a finite energy gap in the entire Brillouin zone of the bulk materials, however in their surface they hos Dirac quasiparticles[14].

In this topological insulating systems there is a **bulk-boundary correspondence**, where the change of the invariant, $\Delta\nu$, across an interface of two materials is intimately tied to the occurrence of surface states, which closes the energy gap in the interface. These topologically protected surface states have a massless Dirac spectrum, where the momentum is locked to the spin, and thus results in a spin-helical metal[21]. This system is modeled a a dirac spectrum in one dimension, such chiral modes are also encountered at the edges of quantum hall systems. However,

in constrast to the QHE, which occurs in strong magnetic fields, topological insulators exist in the abscence of a magnetic field[22].

In topological insulators, spin-orbit coupling takes over the role of the magnetic field, and time-reversal symmetry is preserved at interfaces between a topological insulator and a normal insulator, unless further external perturbations, such as magnetic impurities, are present. Thus, Kramer's theorem is applicable and implies that the edge states must have a time-reversed counter part (opposite spin and momentum) at equal energy at topological insulator interfaces. In the simplest model, a topological insulator implements two copies of the Hamiltonian to describe pairs of counter-propagating time-reversed states[57]:

$$H_{TI}(\vec{k}) = \begin{pmatrix} H(\vec{k}) & 0 \\ 0 & H^*(-\vec{k}) \end{pmatrix} \tag{2-3}$$

2-3 is equivalent to 2-2, this is why we can consider that both are described by the Dirac Hamiltonian, because this preserve the time-reversal symmetry required by the system which is in nature different of the symmetries required for the graphene, which are just related to its crystallographic structure.

Regarding the superconductors cuprates which can be viewed as 2D materials, due to extensive experimental data, it can be phenomenologically described by a 2D spin-singlet superconductor where the gap is $\Delta_K = \Delta_0 \left[\cos(k_x a) - \cos(k_y a)\right]$, the gap close when $|k_x| = |k_y|$ in the Brillouin zone, where the nodal points are presented around the corners of the Brillouin zone, where $\Delta_K = 0$ cross the fermi surce $\varepsilon_{\vec{k}} = 0$ [35, 14]. In the nodal points the hamiltonian can be simplified by doing a k.p approximation into the the Bogoliubov-de Gennes hamiltonian to a anisotropic Dirac Hamiltonian with the form:

$$H_{BdG} = \hbar v_F k_\perp \tau_z + \hbar v_\Delta k_\parallel \tau_x \tag{2-4}$$

The previous mathematical and physical descriptions for the discussed systems show that the nature of the microscopic origin of Dirac Fermion excitation is different for each system. In addition to previous materials, also Weyl semi-metals and 3D Dirac semi-metal, are Dirac Materials.

In figure **2-3**a angle-resolved photoemission spectroscopy have been used to probe the linear band dispersion in Graphene, as well as for Ca-doped Bi_2Se_3 in figure **2-3**b with the addition of the locked behavior of the electronic spin to the surface Dirac cones states, which are pointed out by the red arrows that show the orientation of the spin over each band [14]. Finally in figure **2-3**c the Fourier transform of scanning tunneling spectroscopy shows the contours of constant energy below the conduction band were the fermi level is located, showing the nodal dirac lines in the corners of the Brillouin zone of a high-temperature superconductor cuprate $Bi_2Sr_2CaCu_2O_{8+\delta}$

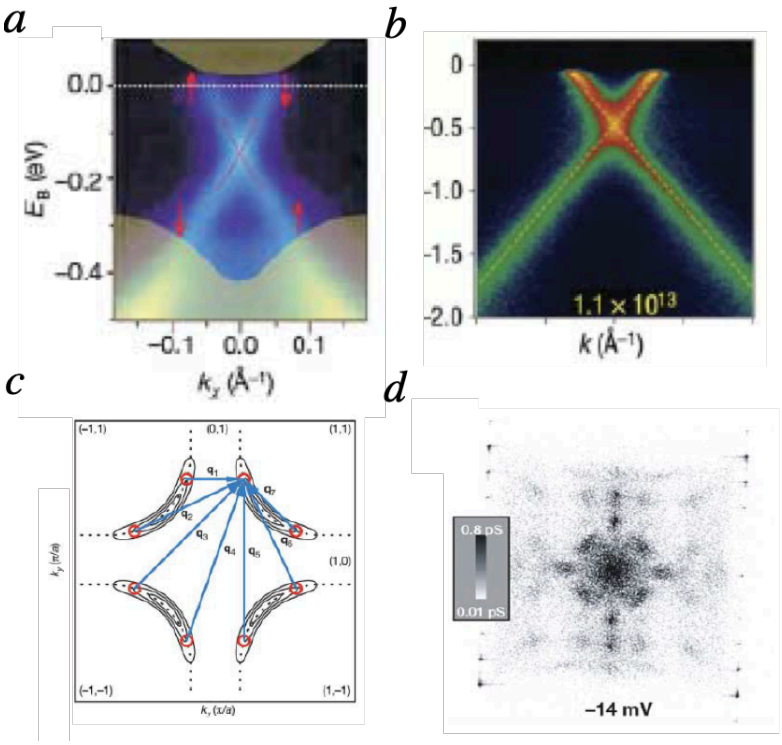

Figure 2-3: Experimental evidence of appearance of dirac nodal lines and shapes in a) Topological insulator. b) Graphene. c-d) High temperature superconductor

where concentration of states could be observed, in the figure **2-3**d can be observed the concentration and distribution of states around the corner of the Brillouin zone[15].

The universal properties of Dirac materials that will be pointed out are the ones connected to thermodynamics and to their dependence on magnetic fields. The low energy form of the DOS, $N_0(E)$, for Dirac materials around the Dirac point and for a d-dimensional dirac material is $N_0(E) \sim E^{d-1}$. This quantity influence in the thermodynamic response of this kind of material, characterized just by a power-law depending on the exponent of the dimensionality of the system, for instance the specific heat for Dirac Materials is $C(T)_{T\to 0} \sim T^d$, which is different from the linear dependence encountered for normal metals[35].

In the case of magnetic field dependence, the Landau quantization appears in Dirac Materials when the minimal substitution is done $\vec{p} \to \vec{p} + e\vec{A}$, where $\vec{A}$ is the vector potential. Introducing this in the 2D Dirac Hamiltonian it is possible to find that the energy depending on the field is $E_{n,\pm} = \hbar v_F \sqrt{\frac{2eB|n|}{\hbar}}$, in this case the dependency of the level index n is a square-root dependence which contrast of with the linear dependence for Schröndinger fermions. Other distintive feature is the zeroth landau level in this sistem is independent on the field and is located at zero energy, this level is shared by electrons and holes to equal amounts. Its existence also gives rise

to a quantum hall effect with quantization of the hall conductance at half-integer values, this feature is a hallmark of magnetotransport dominated by Dirac carriers[57, 13].

There are also relevant transport properties in Dirac materials such as effects like suppressed backscattering, Klein tunneling, creation of midgap states, universal minimum conductivity, weak antilocalization, suppression and restoring of Anderson localization, and scattering off random (pseudo)-magnetic fields have all been investigated theoretically. Many of these effects have also been realized in experiments on graphene[35].

2.3 Graphene-like materials

2.3.1 Crystal structure

The discovery of graphene, the first 2D material, has led to joint efforts in the scientific community for the synthesis of new 2D materials. The graphene-like family presents a similar crystal lattice with honeycomb structures as in figure **2-4A**, where blue and yellow atoms belong to their own sublattices[44, 58]. The observation that such a single free-standing sheet of atoms is stable was already quite a surprise since Mermin and Wagner theorem states that 2D crystal cannot exhibit long-range order at any finite temperature, however in 1987 Nelson et Al[59]. performed a theoretical study on the intricate interplay between crystalline orden and thermal fluctuations showing that this plays a crucial role in the stability of membrane due to anharmonic coupling. Material such as graphene shows this behavior that allows them to have this exotic phase. Other examples are germanene, silicene, transition metal dichalcogenide (TMD), arsenene, h-BN, among others[60].

In the case of graphene, monolayer do not have a buckled structure. Silicene and germanene present buckle structures as shown in figure **2-4B** and **C**. Si-Si or Ge-Ge have larger interatomic distances which weakness the π-π overlaps, so it cannot maintain the planar structure anymore, this results in a low-buckled structure with sp^3-like hybrid orbitals. Silicene and Germanene due to their larger atomic number have stronger spin-orbit coupling, a reduction in the buckling of the system will increase the SOC by an order of magnitude. This change can open a small gap in this system allowing topological-protected gapless helical modes at the edges of the 2D material and a QSHE characterized by spin current transport.

The TMDs are another type of graphene-like material, which in contrast with previous materials, can exist in three common structural phases as shown in image **2-4D**, this of course, depends on the type of chalcogen and transition metal atoms. The structural phase depends on how the three atoms are stacked in each atomic plane[61, 62]. The 2D phases correspond to ABA in which chalcogen atoms in different atomic planes occupy the same position A and are on top

of each other for the same vertical line. In the case of 1T is characterized by an ABC order. 1T' form exists as a metastable form. The 2H form is formed for instance by Mo and W and the 1T for Ti and Re, either with S, Se, or Te as chalcogen atoms[63].

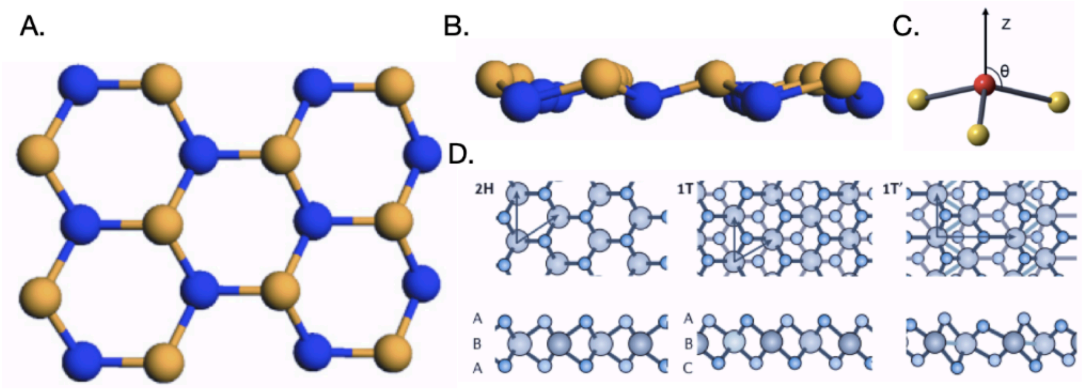

Figure 2-4: A. Shows the honeycomb structure of germanene and silicone. B. and C. Exhibit the buckled structure for this type of honeycomb system. D. presents the different crystal structures of TMDs, in particular, we will explore the TMDs type 2H. Figure adapted from [47] and [64]

2.3.2 Electronic band structure

In this section, we will focus on germanene, silicene and TMDs. Initially using DFT calculations with them in planar form has been observed that it has an unstable phase, however introducing a slightly buckled structure results energetically favorable at the expense of lowering the point group symmetry from D_{6h} to D_{3d} [65, 66]. The band structures for germanene and silicene are shown **2-5**, for the same material but varying the buckled height, will change the gap around the Dirac points and will change the linear dispersion[44, 58]. The DFT studies shows that the range for the height could be in between $6.4 - 7.4$nm. For the actual crystal structure, each material presents a spin-orbit coupling that is splitted around the K corners, in contrast with graphene. For the case of silicene, the spin-orbit coupling is aroun 1.55 meV at a temperature of 18 K, which is observed in **2-5A**, for Germanene it is 23.9 meV at room temperature[65]. The presence of this gap assures the appearance of topological properties for silicene and germanene.

The structural and electronic properties of germanene can be significantly modified by interaction with the underlying substrate ranging from weak physisorption to strong chemisorption[67]. One mechanism that has been proven to be relevant for the magnitude of the buckling is lateral strain, appearing deposited structures due to improper matching between the lattice constants of the substrate and adsorbed layer[66]. In this case, silicene is more reactive than graphene.

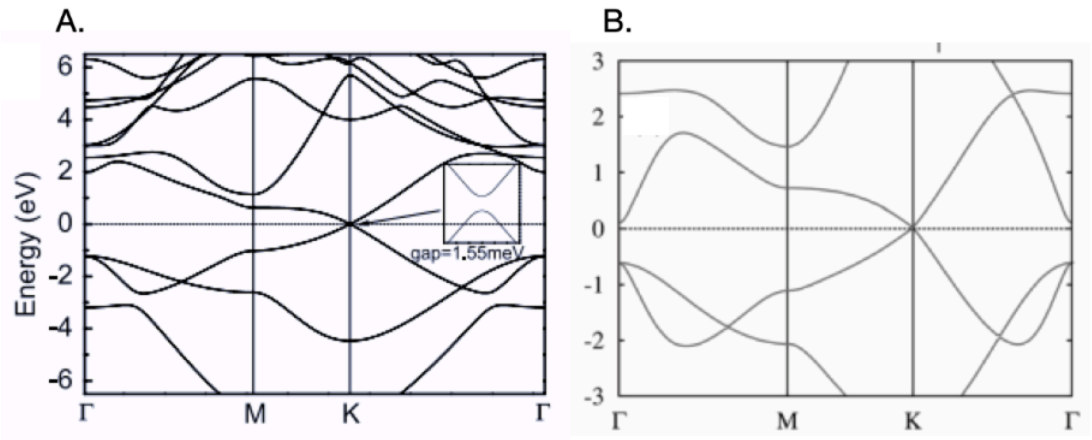

Figure 2-5: The figure shows the electronic band structure for Silicene (A) and Germanene (B), inset in A zoom in to expose the gap due to spin orbit coupling. Adapted from [44] and [58]

The substrate-absorbent interaction in silicene on Ag(1 1 1), for instance, is considerable, and although the adsorption preserves the hexagonal structure of silicene, the Ag substrate induces a sizable ot-of-plane buckling of the Si atoms, the hybridization between the silicene and the Ag states leads to a large perturbation of the silicene electronic structure, such behavior is also shown by germanene[68].

In the case of TMDs, their diversity of chemical compositions and structural phases of TMDs result in a broad range of electronic properties, both from the point of view of the band structure character (metallic or insulating) and of the emergence of correlated and topological phases [61, 70]. This section will be focused on the band structure of TMDs formed by group VI transition metals Mo and W combined with S and Se due to their semiconducting properties.

In their thermodynamically stable 2H phase, MoS_2, $MoSe_2$, WS_2, and WSe_2 are semiconductors. This property drew attention to these TMDs as 2D materials for electronic devices. The evolution of the band structure of 2H-MoS2 as calculated from DFT upon reducing its thickness from bulk to monolayer is shown in figure **2-5**. The positions of the valence and conduction band edges change with decreasing thickness and the indirect bandgap semiconductor bulk material turns into a direct bandgap semiconductor monolayer, this observed in **2-5** MoS_2 and WS_2, this is a shared properties for TMDs of this family[62, 61].

The calculated values for the bandgap of bulk and monolayer 2H-MoS_2 are 0.88 and 1.71 eV, respectively. The experimental value for the bandgap of monolayer 2H-MoS_2 is 2.16 eV[70]. Importantly, the valence band maximum and the conduction band minimum are located at the two inequivalent high-symmetry points K and K′, which correspond to the corners of the hexagonal Brillouin zone[47]. This property is common to monolayer 2H-MoS_2 (and other group VI

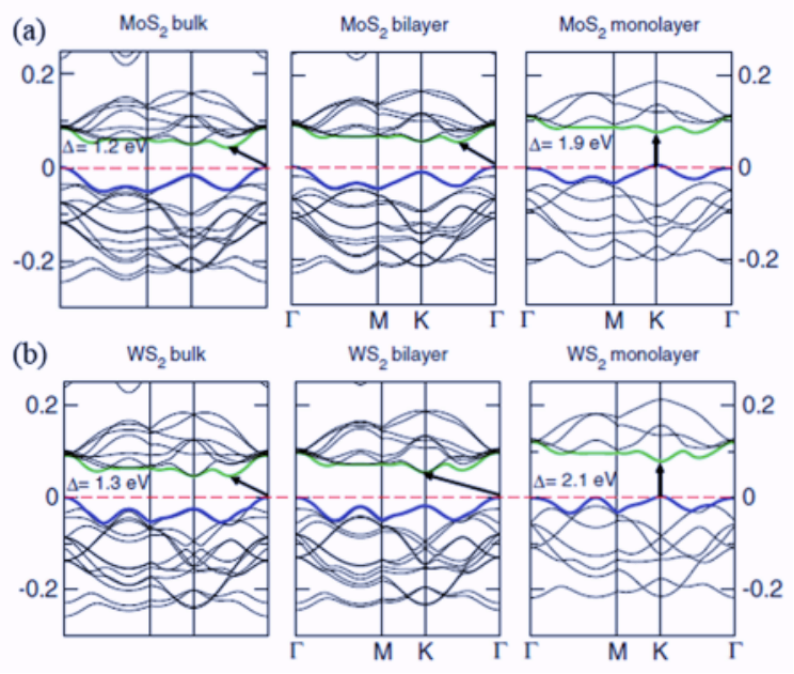

Figure 2-6: Electronic band structure from bulk to monolayer in semiconductor TMDs MoS_2 (a) and WoS_2 (b). Adapted from [61, 69]

monolayer 2H-TMDs) and to graphene, and enables the observation of valley-dependent physical phenomena and potential valleytronics applications[61, 69].

Another important peculiarity of monolayer 2H-TMDs is that they lack inversion symmetry, which results in a spin splitting of the electronic bands driven by the spin–orbit interaction. Because points K and K′ do not correspond to the time-reversal invariant momenta, the spin degeneracy of the conduction and valence band extrema at these points is lifted[61, 69]. This effect is particularly strong in the valence band, in which spin-splitting values range from 0.15 eV in monolayer 2H-MoS_2 to 0.46 eV in 2H-WSe_2. This trend is understood by considering that the spin–orbit interaction is a relativistic effect and hence is stronger for heavier elements. Even though the spin splitting of the conduction band is about an order of magnitude weaker, it is not negligible. Because of time-reversal symmetry, the spin splitting of bands at K and K′ is opposite; the resulting band structure of monolayer 2H-MoS_2 is relevant to realistic charge-carrier concentrations. This property is referred to as spin–valley coupling and implies that the valley polarization of charge carriers is automatically translated into their spin polarization[70]. This intrinsic property of TMDs may be used to design spintronic devices that do not involve magnetic materials[63].

2.3.3 Experimental evidence

The experimental realization of the graphene is mainly realized by micromechanical cleavage of bulk graphite, the same technique that allowed the isolation of graphene for the first time[71, 72]. After fine-tuning, the technique now provides high-quality graphene crystallites up to 100 μm in size, which is sufficient for most research purposes, like in figure **2-7A** and **B**.

Superficially, the technique looks no more sophisticated than drawing with a piece of graphite or it's repeated peeling with adhesive tape until the thinnest flakes are found. A similar approach was tried by other groups but only graphite flakes 20 to 100 layers thick were found[73, 74]. The problem is that graphene crystallite left on a substrate is extremely rare and hidden in a 'haystack' of thousands of thick (graphite) flakes. So, even if one were deliberately searching for graphene by using modern techniques for studying atomically thin materials, would be impossible to find those several micrometer-size crystallites dispersed over, typically, a 1 cm^2 area [71, 72]. For example, scanning-probe microscopy has too low a throughput to search for graphene, whereas scanning electron microscopy is unsuitable because of the absence of clear signatures for the number of atomic layers[73].

The critical ingredient for success was the observation that graphene becomes visible in an optical microscope if placed on top of a Si wafer with a carefully chosen thickness of SiO_2, owing to a feeble interference-like contrast with respect to an empty wafer as is shown in figure **2-7A**, where for instance zig-zag and armchair edges can be observed. If not for this simple yet effective way to scan substrates in search of graphene crystallites, they would probably remain undiscovered today[73]. Indeed, even knowing the exact recipe, it requires special care and perseverance to find graphene. For example, only a 5% difference in SiO_2 thickness (315 nm instead of the current standard of 300 nm) can make single-layer graphene completely invisible. Careful selection of the initial graphite material (so that it has largest possible grains) and the use of freshly cleaved and cleaned surfaces of graphite and SiO2 can also make all the difference[71]. Note that graphene was recently found to have a clear signature in Raman microscopy, which makes this technique useful for a quick inspection of thickness, even though potential crystallites still have to be first hunted for in an optical microscope[72].

Similar stories could be told about other 2D crystals (particularly, dichalcogenide monolayers) where many attempts were made to split these strongly layered materials into individual planes. However, the crucial step of isolating monolayers to assess their properties individually was never achieved. Now, by using the same approach as demonstrated for graphene, it is possible to investigate potentially hundreds of different 2D crystals in search of new phenomena and applications[63].

The MoS_2 and WS_2 are probably the only TMDs that occur in nature in the form of a layered

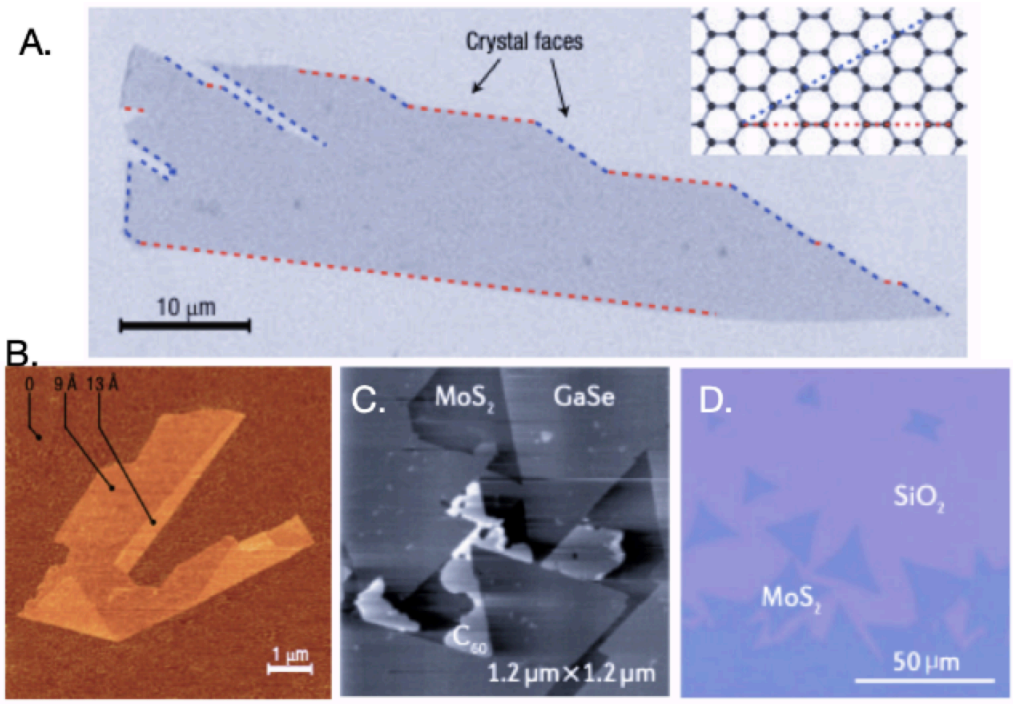

Figure 2-7: Experimental evidence of fabrication of graphene (A and B) and TMDs (C and D). Adapted from [71, 72, 61]

crystal[61]. The first high-performance transistors made of monolayers of MoS_2 were obtained from crystals of the naturally occurring mineral molybdenite. Bulk crystals of other TMDs are grown using the chemical vapor transport method , which enabled the first studies of the optical and electrical properties of MoS_2, $MoSe_2$, and WSe_2 crystals in the 1960s[47]. Such a technique results for this kind of material can be observed in figure **2-7**.

High-quality natural or synthetic crystals can be used as a source of thin flakes. Similarly to graphene, which can be obtained by mechanical exfoliation with sticky tape from graphite, single crystals of TMDs can serve as a source of monolayers[62, 75]. Because micromechanical exfoliation requires only bulk crystals, a decent optical microscope and adhesive tape, which is a very popular method for the rapid prototyping of devices based on TMDs and other layered materials and has greatly contributed to the rapid expansion of research in this area. However, this method is not scalable; moreover, the relatively small areas of uniform material and the haphazard nature of material deposition can be limiting factors for more extensive studies[69].

Liquid-phase exfoliation based on organic solvents is a scalable alternative to mechanical exfoliation and allows the production of solutions containing flakes with a controllable thickness[61]. The first experiments on liquid-phase exfoliation through Li intercalation date back to the 1970s, with a report on solutions containing single-layer MoS_2 from the 1980s[62]. The drawbacks of

exfoliation through Li intercalation including reported phase transitions from the semiconducting 2H to the metallic 1T phase and the limited size of the flakes, which results in overlaps between the flakes and in a large in-plane resistance of the films. One of the more scalable method developed for the direct growth of TMDs was molecular beam epitaxy, results using this technique can be observed in **2-7C**

The synthesis of germanene and germanene-related materials do not have a general recipe due that their fabrication still topic of research, however it was on the preparation and exfoliation of germanane (GeH), Germanane, i.e. hydrogen-terminated germanene, was successfully prepared via the topochemical deintercalation of $CaGe_2$[65]. Germanane sheets can be obtained by simple exfoliation of the layered van der Waals solid. At ambient conditions, germanane is very stable and only oxidizes in a time span of several months. This stability is an important prerequisite for the usage of germanane in any technological application[60].

As pointed out in the preceding section free-standing germanene is stable against local lattice distortions. To date germanene has been reported to be synthesized on only a few substrates[65, 66]. In July 2014 was reported the growth of germanene on Pt(111). Germanium was deposited on a pristine Pt(111) substrate at room temperature under ultrahigh vacuum conditions from a germanium rod mounted in an electron-beam evaporator. Other techniques have focues in the manipulation and use of differents substrate such as Au (111), Ge_2Pt, among others. A sample of germanene in substrate of Ge_2Pt with nearest neighbor distance of 25 nm, observed with a scanning tunneling microscope appears in figure **2-8A**, where a clear honeycomb structure is observed[66].

To date, germanene has only been grown on metallic substrates. It is very likely that the relevant electronic states of germanene near the Fermi level hybridize with the electronic states of the metallic substrate and destroy the 2D Dirac character of the germanene[76]. It would be a huge step forward if germanene could be synthesized on a wide band gap material. A possible candidate would be hexagonal boron nitride (hBN), h-BN has a band gap of about 6 eV and its lattice constant (2.5 Å) is almost identical to the nearest neighbor's distance of germanene[68].

An equivalent material is a silicene, which despite the theoretical prediction of it down to 2004, the breakthrough in the experimental synthesis of silicene took place in the year 2012, when several groups reported in parallel the successful preparation of monolayer silicene sheets on Ag (111)[77, 78]. It should be noted that the successful synthesis of silicene on another substrate, ZrB_2(001), was achieved independently around the same time [76]. Following the successful preparation of silicene, the studies on silicene see a sudden burst in the following few years. A silicene honeycomb 2D structure grown in Ag(111) is presented in figure **2-8B**, observed by using scanning transmission microscopy[46].

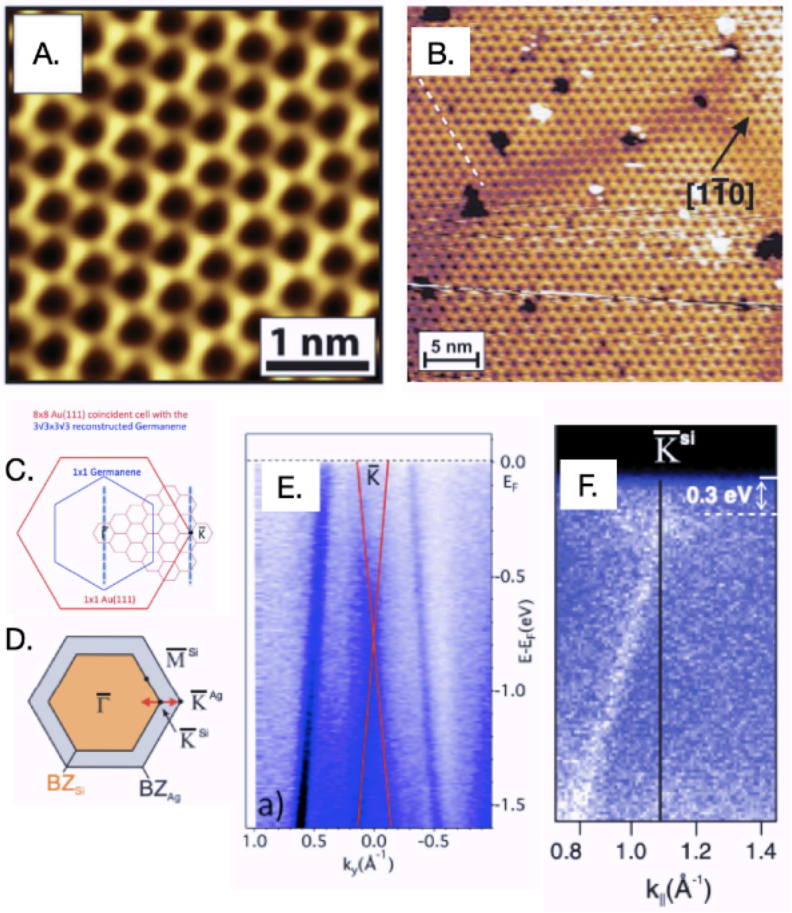

Figure 2-8: A. The honeycomb structure of Germanene in Ag substrate. B. Synthetized silicone on Ag substrate. C and D are Brillouin zone representations of the region where ARPES is calculated. E and F, correspond to experimental evidence of linear dispersion in Germanene and Silicene, respectively. [66]

Angle-Resolved Photoemission is used to study the formation of linear dispersion of states for germanene and silicene[76]. The figure **2-8C** is shown that the ARPES is studied in the K point along the dashed line for the Germanene and Au substrate [67, 66], where in the figure **2-8E** is observed the signature of Dirac cone pointed out by the red lines around the K points from Au, which recovers the features from the germanene sample[60, 65]. In addition **2-8D** shows that formation of the linear dispersion of a Silicene monolayer over a substrate of Ag(111) is studied over the K point of the silicene honeycomb structure [68], with the direction pointed out by the red arrows, the Dirac cones kind of shape is observed in figure **2-8F** where there is a gap or around 0.3 eV which is a product of the interaction in between the substrate and the monolayer[66].

2.3.4 Hamiltonian

In this section, we will discuss the common Hamiltonian considered for TMDs, silicene, and germanene in the k.p approximation around the k points[70, 76].

For instance, a well-known Hamiltonian that describes the TMDs, that captures features such as the linear dispersion and the spin-splitting in the valence band is described by the equation:

$$H_{TMDs} = \hbar v_F \left(\eta k \sigma_x + q\sigma_y\right) + \frac{\Delta}{2}\sigma_z - \lambda_{SOC}\frac{\sigma_z - 1}{2}s\eta \tag{2-5}$$

Where v_F is the fermi velocity, Δ corresponds to the band gap, σ are the pauli matrices for the pseudospin degree of freedom given by the sublattices, η corresponds to the valley index, s can be 1 or -1 if the electron spin is up or down, respectively. k and q are the projections of the wave number into the *x* and *y* direction.

This model correctly captures the large, spin-splitting of the valence band, predicts the valley-dependent optical selection rule and express the coupled spin vand valley physics in accordance with experiments [70, 79].

In addition, silicene and germanene can be described by an equivalent hamiltonian, which is described as:

$$H_{Si/Ge} = \hbar v_F \left(\eta k \sigma_x + q\sigma_y\right) + s\eta\lambda_{SOC}\sigma_z \tag{2-6}$$

where the main feature related to the Dirac cones at low energy near the fermi energy is fully described by this equation. The opening of the gap is due to the spin-orbit coupling as predicted by DFT calculations [80, 44].
In general this Hamiltonian can be compacted in the following way:

$$\check{H}_{s\eta}\left(\mathbf{k}\right) = \mu_{s\eta}\hat{\sigma}_0 + \hbar v_F \left(k\hat{\sigma}_x + \eta q\hat{\sigma}_y\right) + m_{s\eta}\hat{\sigma}_z \tag{2-7}$$

Where $\mu_{s\eta}$ is an effective chemical potential and $m_{s\eta}$ is an effective mass for the Dirac fermions around the K points, each can be written as:

$$\mu_{s\eta} = -E_F + \eta s\lambda_{SO}, \tag{2-8}$$

$$m_{s\eta} = -\eta s\lambda_{SO} + \frac{\Delta}{2}. \tag{2-9}$$

Typical external field sources that previously have been reported correspond to the use of electric field perpendicular to the monolayer of Germanene and Silicene, which introduces an additional term in the equation 2-9 of the form $\lambda_z = lE_z$, where l correspond to the relative distance in between planes in the buckled structure in this kind of materials and E_z is the external electric field[81, 53]. Also, a magnetic-induced field due to the presence of magnetic materials in contact with the monolayer can be taken into account by adding a term $s\lambda_B$ where s correspond

to the effect into the term due to the electron's spin orientation when the hamiltonian at the interface is studied[64].

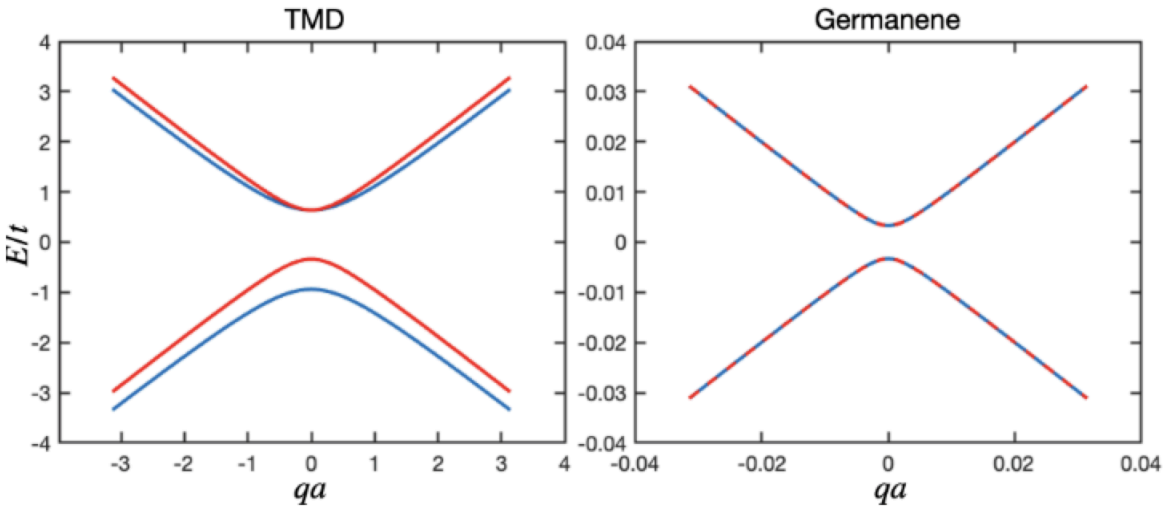

Figure 2-9: Energy diagram around K points for TMD (left) and Germanene (right) for electons with spin up (blue) and down (red)

The figure **2-9** show the energy plots for electron's with spin up and down in Germanene and TMD. For the case of TMD, in this case WSe_2, we observe the break of degeneracy for the valence band and not for the conduction band; the energy diagram for spin up and down electron around K point is inverted around K' points, i.e. energetically spin down electrons in K behaves as spin up electrons in K; the gap of a few eV exhibit the semiconducting properties of this type of TMD. For the germanene, the scale used is one hundred times smaller than for TMDs, where a small gap of a few mV is observed revealing in this way their properties as semi-metalic, in this type of system there is not breaking of spin degeracy at least an external field is applied.

2.3.5 Applications

Graphene

Transparent conductive coatings are frequently utilized in electronic applications, such as touch screens, e-paper, and organic light-emitting diodes (OLEDs). These coatings require low sheet resistance and high transmittance (over 90%), depending on the specific application. Graphene meets these requirements with a sheet resistance of 30 V per square of 2D area in highly doped samples and an excellent transmittance of 97.7% per layer. Although indium tin oxide (ITO) still has slightly better characteristics, graphene's quality keeps improving every year and ITO deposition is already expensive, making graphene a potential contender for securing a good portion

of the market[82, 74].

Research is being conducted to open a bandgap in graphene for transistor use, but so far, none of the approaches have been successful in creating a bandgap wider than 360 meV, limiting the on/off ratio to about 10^3 [73]. New transistor designs are emerging that exploit the modulation of the work function of graphene, allowing for vertical transport through various barriers[71, 72]. These devices can achieve on/off ratios of 10^6, but more work on integration is required to enable the use of graphene for logic applications.

Graphene photodetectors have a wide spectral range from ultraviolet to infrared and high operating bandwidth, making them suitable for high-speed data communications[71, 73].

Graphene's unique properties make it ideal for sensor applications, from measuring magnetic fields to DNA sequencing and from monitoring the velocity of surrounding liquids to strain gauges. Graphene sensors' multi-functionality allows for multidimensional measurements, such as strain, gas environment, pressure, and magnetic field. With the development of increasingly interactive consumer electronic devices, such sensors will likely become more prevalent in many products[71, 72].

Finally, graphene has potential applications in bioengineering, such as drug delivery, tissue engineering, and regenerative medicine. Its unique mechanical properties make it ideal for imaging biomolecules in transmission electron microscopy, and chemically-functionalized graphene could lead to fast and ultrasensitive measurement devices capable of detecting a range of biological molecules[82, 74].

TMDs

Determining charge carrier mobility is essential in understanding quantum transport properties. For 2D TMDs, electron mobility is predicted to be in the range of $10 - 10^3$ $cm^2V^{-1}s^{-1}$ at room temperature and increases up to 10^5 $cm^2V^{-1}s^{-1}$ at low temperature. However, experimental results show that point defects and disorders limit its practicality. The first transistor based on a monolayer of MoS_2 using encapsulation on HfO_2 has been fabricated, but mobility decreases at temperatures above 200 K due to impurities. Encapsulations with h-BN, combined with graphene as the contact between the metal and MoS2 layer, have resulted in the highest low-temperature measured to date, with hall mobility of 34000 $cm^2V^{-1}s^{-1}$ and 100 $cm^2V^{-1}s^{-1}$ for six layers and monolayer, respectively[47, 82]. These results pave the way for observing fundamental phenomena such as shibnikov-de has oscillation in electrical conductivity at low temperatures and high magnetic fields[63].

The high strength of 2D TMDs makes them good for strain engineering as they can endure strains

of up to 10% before breaking. When subjected to tensile strain, they can be turned into indirect semiconductors, and their bandgap would fully close at a level of biaxial tensile strain of 10% [47, 69]. Strain can also modulate other properties such as charge carrier effective masses, thermal conductivity, dielectric properties, spin-orbit coupling and on-state currents in TMD transistors [75]. Therefore, strain engineering is a viable approach for creating electronic, optoelectronic, electromechanical and spintronic devices with tunable characteristics[61].

TMDCs have attracted interest as materials that could host exotic electronic phases. Theoretical predictions have shown the existence of the quantum spin Hall phase or 2D Z_2 topologically insulating phase in certain types of TMDs[69]. These phases are characterized by the presence of helical edge states immune to backscattering. TMD-based quantum spin Hall insulators could enable technological applications of this topological electronic phase[47, 62].

The 2D TMDs are more suitable for practical applications than other quantum spin Hall insulators. Polymorphs of these materials were predicted to host a Weyl semimetal phase, which was, to some degree, experimentally confirmed[70].

The superconducting behavior of bulk TMDs persists in the 2D limit. Recently, the first experimental evidence for intrinsic 2D superconductivity in TMDs was reported for monolayer 2H-$NbSe_2$. The superconducting state in monolayer TMDs is characterized by an Isinglike polarization of spins in the out-of-plane direction, making it more robust against in-plane magnetic fields. Ising superconductors could be useful for observing topological superconductivity and as an alternative route to engineer Majorana fermions in solid-state systems[61].

Germanene and Silicene

Silicene, a silicon version of graphene, has a buckled honeycomb lattice and a tunable two-dimensional monolayer, making it a promising material for nanoelectronic devices[78, 76]. The material has the potential for a variety of predicted electronic properties, including the quantum spin Hall effect, chiral superconductivity, giant magnetoresistance, and other field-dependent states. Despite recent progress in epitaxial synthesis and investigation of its electronic properties, no experimental silicene devices have been reported due to air stability issues. Here, we report a silicene field-effect transistor that exhibits ambipolar Dirac charge transport, with a measured room temperature mobility of approximately 100 $cm^2V^{-1}s^{-1}$ attributed to acoustic phonon-limited transport and grain boundary scattering[68, 76]. These results were achieved through a growth-transfer-fabrication process known as silicene encapsulated delamination with native electrodes[58].

Applications of silicene and germanene in spintronics require the introduction of magnetism[58]. This can be achieved through the magnetic proximity effect with a magnetic insulator. For ex-

ample, in a junction of silicene/ferromagnetic/silicene, the conductance of charge, valley, and spin oscillate with the length of the ferromagnetic silicene[64, 57]. There is coupling between the valley and spin degrees of freedom, which can be tuned using local gate voltage. This allows for tuning of valley- and spin-polarization and achieving a fully valley-spin-polarized current. Such applications make these materials useful for efficient manipulation of spin/valley degree of freedom.

Other fundamental interest in germanene and silicene lies in their capabilities to host phenomena such as anomalous quantum hall effect and quantum spin hall effect. In particular, let's remember that graphene has been discussed to host this type of phenomenon however, their negligible SOC has avoided the direct observation of it. In this the strong SOC in germanene and silicene has allowed the existence of such effects. In particular, the anomalous quantum hall effect is on of the most powerful ways to check whether a 2D material is indeed a Dirac fermion system[46, 64].

2.4 Generalized green function method for Dirac Hamiltonian

In this section, we will describe the general Hamiltonian for 2D Dirac materials, as well as the solutions of the Hamiltonian for general crystallographic structure. Then, the green function for an infinite system is shown, and the perturbative method using the Dyson equation is fully described with the purpose of finding the semi-infinite and finite system green's function considering specific boundary conditions.

2.4.1 Generalized hamiltonian for 2D Dirac Materials

We consider the following general Dirac Hamiltonian, acting on a two-dimensional space

$$\check{H}(x,y) = -i\hbar v_F(\check{\alpha}_x\partial_x + \check{\alpha}_y\partial_y) + \check{V}(x,y), \tag{2-10}$$

with v_F the Fermi velocity and $V(x,y)$ an electrostatic potential. Here, $\check{\alpha}_{x,y}$ are $2N \times 2N$ matrices acting on the $SU(2)$ degree of freedom that defines the Dirac Hamiltonian and the N-dimensional space containing the rest of degrees of freedom.

In the following, we assume translation invariance along the y-axis, with $k_y \equiv q$ a conserved quantity, and consider inhomogeneous systems along the x direction. Then, equation 2-10 reduces to

$$\check{H}_q = -i\hbar\partial_x\check{\alpha}_x + q\check{\alpha}_y + \check{V}(x), \tag{2-11}$$

which obeys the eigenvalues problem

$$\check{H}_q\psi_q(x,y) = E_q\psi_q(x,y), \tag{2-12}$$

with solutions of the form

$$\psi_q(x,y) = e^{iqy}\left[\psi_n^+ e^{ik_n^+ x} + \psi_n^- e^{ik_n^- x}\right], \tag{2-13}$$

for $V(x) = 0$, where $\psi_n = (\psi_n^+, \psi_n^-)^T$ are $2N$-dimensional spinors in the $SU(2)$ space spawned by $\check{\alpha}_x$, with n labeling the other quantum numbers.

The states $\psi_n^{\pm} e^{ik_n^{\pm} x}$, where, usually, $k_n^- = -k_n^+$, represent right (ψ_n^+) and left (ψ_n^-) moving solutions along the x direction, with probability flux current given by $J_{n,x}^{\pm} = v_F \psi_n^{\pm\dagger} \check{\alpha}_x \psi_n^{\pm} = \pm v_F$. However, these states are not orthogonal. To obtain an orthogonality relation, we must define the states

$$\tilde{\psi}_n^{\pm} = \pm \check{\alpha}_x^{\dagger} \psi_n^{\pm}, \quad (\tilde{\psi}_n^{\pm})^{\dagger} = \pm (\psi_n^{\pm})^{\dagger} \check{\alpha}_x, \tag{2-14}$$

which then fulfill

$$(\tilde{\psi}_n^{\varepsilon})^{\dagger} \psi_m^{\varepsilon'} = \delta_{nm} \delta_{\varepsilon\varepsilon'}, \tag{2-15}$$

with $\varepsilon = +, -$. Combining $\psi_n^{\pm}$ and $\tilde{\psi}_n^{\pm}$ states we also find the completeness relation

$$\sum_{\varepsilon,n} \psi_n^{\varepsilon} (\tilde{\psi}_n^{\varepsilon})^{\dagger} = \check{1}, \tag{2-16}$$

with $\check{1}$ being the $2N \times 2N$ unit matrix.

2.4.2 Green function for infinite 2D Dirac system

The green function for an infinite system corresponds to the solution of the following equation,

$$\left(E\check{1} - \check{H}_q\right) \check{G}_q(x,x') = E\delta(x-x')\check{1}. \tag{2-17}$$

When $k_n^- = -k_n^+ = -k_n$, with $k_n \geq 0$, the Green's functions of the unbounded (bulk) system become

$$\check{g}^{<}(x < x', x') = \frac{-i}{2\hbar v_F} \sum_n f_n^-(x-x')\, \psi_n^- (\bar{\psi}_n^-)^T, \tag{2-18a}$$

$$\check{g}^{>}(x > x', x') = \frac{-i}{2\hbar v_F} \sum_n f_n^+(x-x')\, \psi_n^+ (\bar{\psi}_n^+)^T. \tag{2-18b}$$

Here, the x-dependence is encoded in the functions $f_n^{\varepsilon}(x) = e^{i\varepsilon k_n x}$, and the states $\bar{\psi}_n^{\varepsilon}$ are solutions to the transposed Hamiltonian in equation 2-10. Transposing a Dirac Hamiltonian results in the exchange $\mathbf{k} \to -\mathbf{k}$, so the transposed states can be related to the left and right moving states in equation 2-13 as

$$\bar{\psi}_n^{+T} = \left(\check{\gamma}\psi_n^-\right)^T, \quad \bar{\psi}_n^{-T} = \left(\check{\gamma}\psi_n^+\right)^T, \tag{2-19}$$

with $\check{\gamma}$ a matrix such that the scalar product $\psi^{\dagger}\check{\gamma}\psi$ is invariant under Lorentz transformations and spatial inversion [52].

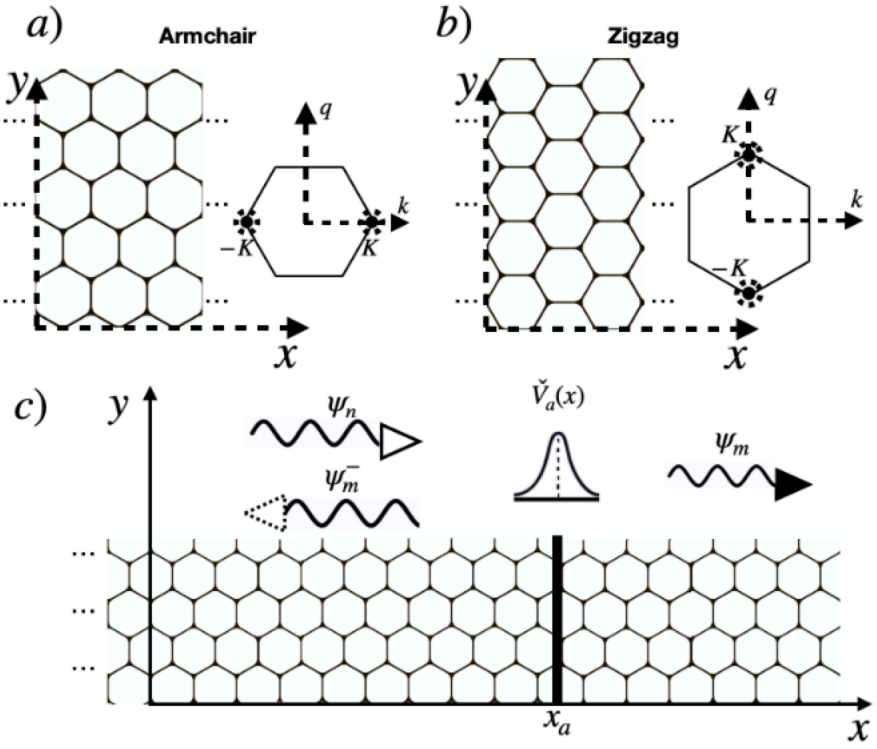

Figure 2-10: a) and b) corresponds to the real-space orientation for edge type of boundary condition. The hexagon next to each lattice case is the corresponding reciprocal unit cell where the valley K and K', i.e.-K, are shown. c) Corresponds to a semi-infinite monolayer generated due a Dirac-like potential at a particular x_a coordinate, the arrows correspond to the incident (ψ_n) and reflected wave function (ψ_m and ψ_{-m}) at the edges.

2.4.3 Green function for semi-infinite 2D Dirac system

We can define a sharp edge localized at $x = x_a$ by means of the perturbation potential $\check{V}(x) = U_a \check{\tau} \delta(x_a - x)$, with U_a the potential strength that takes the limit $U_a \to \infty$ when we consider the edge of a semi-infinite layer. Here, $\check{\tau}$ is a matrix that encodes the specific boundary conditions at the edge. The perturbed green function by this potential is given by Dyson's equation as

$$\begin{aligned}\check{G}_a(x,x') &= \check{g}(x,x') + \int \mathrm{d}x_1 \check{g}(x,x_1)\check{V}(x_1)\check{G}_a(x_1,x') \\ &= \check{g}(x,x') + \check{g}(x,x_a)U_a\check{\tau}_a\check{G}_a(x_a,x')\,. \end{aligned} \tag{2-20}$$

The solution for $\check{G}_a^{RR(LL)}(x,x')$ when $x,x' > x_a$ ($x,x' < x_a$) are on the right (left) of x_a takes the form

$$\check{G}_a^{RR(LL)}(x,x') = \check{g}^{<(>)}(x,x') + \check{W}^{>(<)}(x)\,\check{g}^{<(>)}(x_a,x')\,, \tag{2-21}$$

where we have defined

$$\check{W}^{>(<)}(x) = \check{g}^{>(<)}(x, x_a)\, U_a \check{\tau}_a D^{>(<)}, \tag{2-22}$$

$$\check{D}_a^{>(<)} = \left(\check{1} - \check{g}^{>(<)}(x_a, x_a)\, U_a \check{\tau}_a\right)^{-1}. \tag{2-23}$$

In what follows, it is more insightful to write explicitly the subspace spawned by the left and right moving solutions of 2-10, that is, the $N \times N$ matrices $\hat{\tau}^{\varepsilon\varepsilon'}$. Henceforth, we use the symbol $.\hat{.}.$ to denote the 2×2 matrices in the left and right mover space.

It is possible to transform the equation 2-23 in a more compact way as follows,

$$\check{G}_a^{RR}(x, x') = \check{g}(x, x') \tag{2-24}$$
$$+ \sum_{nm} f_n^+(x - x_a)(\hat{r}_a^{+-})_{nm} f_m^-(x_a - x')\psi_n^+(\bar{\psi}_m^-)^T,$$

with $\hat{r}_a^{+\varepsilon} = \hat{D}_a^+ \hat{\tau}_a^{+\varepsilon}$, where,

$$\hat{D}_a^\varepsilon = \frac{-iU_a}{2\hbar v_F}\left(1 + \frac{iU_a}{2\hbar v_F}\hat{\tau}_a^{\varepsilon\varepsilon}\right)^{-1}. \tag{2-25}$$

and $\hat{\tau}_a^{\varepsilon'\varepsilon}$, are the entries of the matrix $\hat{\tau}$ projected in the right and left moving states.

$$\check{\tau} = \begin{pmatrix} \hat{\tau}^{++} & \hat{\tau}^{+-} \\ \hat{\tau}^{-+} & \hat{\tau}^{--} \end{pmatrix}. \tag{2-26}$$

Equivalently we have

$$\check{G}_a^{LL}(x, x') = \check{g}(x, x') \tag{2-27}$$
$$+ \sum_{nm} f_n^-(x - x_a)(\hat{r}_a^{-+})_{nm} f_m^+(x_a - x')\psi_n^-(\bar{\psi}_m^+)^T.$$

Here, $\check{r}_a$ corresponds to the scattering matrix of reflection amplitudes. For a potential acting on x_a, we can define the transmission amplitudes as $\hat{t}_a^{\varepsilon\varepsilon} = \hat{1} + \hat{r}_a^{\varepsilon\varepsilon}$, and the scattering matrix results in

$$\check{S}_a = \check{1} + \check{r}_a = \begin{pmatrix} \hat{t}_a^{++} & \hat{r}_a^{+-} \\ \hat{r}_a^{-+} & \hat{t}_a^{--} \end{pmatrix}, \tag{2-28}$$

which fulfills the unitarity condition $\check{S}_a \check{S}_a^\dagger = \check{S}_a^\dagger \check{S}_a = \check{1}$.

The semi-infinite system requires a hard edge at $x = x_a$, which we obtain taking the limit $U_a \to \infty$. Then, $\hat{D}_a^\varepsilon \to -(\hat{\tau}_a^{\varepsilon\varepsilon})^{-1}$. The scattering matrix for the semi-infinite system thus reduces to

$$\check{S}_a = \begin{pmatrix} 0 & (\hat{\tau}_a^{++})^{-1}\hat{\tau}_a^{+-} \\ (\hat{\tau}_a^{--})^{-1}\hat{\tau}_a^{-+} & 0 \end{pmatrix}, \tag{2-29}$$

where the transmission amplitudes are zero at the edge. As a result, the matrix of reflection amplitudes is unitary, $(\hat{r}_a^{+-})^\dagger = (\hat{r}_a^{+-})^{-1}$, and, therefore, $[(\hat{\tau}_a^{++})^{-1}]^\dagger(\hat{\tau}_a^{+-})^\dagger = (\hat{\tau}_a^{+-})^{-1}\hat{\tau}_a^{++}$.

2.4.4 Nanorribbon

A 2D nanorribbon of Dirac material correspond a more realistic quantum system in experimental situations, due to this, in the following we will explore what happend to the green function such system.

We can picture a nanorribbon as a an infinite system with two delta Dirac potential's in two different position along x, it is represented as $\check{V}(x) = \sum_{j=a}^{b} U_j \check{\tau}_j \delta(x_j - x)$. In general the problem could be solved considering both potential simultoneaously and using the Dyson equation can de calculated the perturbated green function for the system, however in our method we consider each perturbation sequentially, then the perturbed green function when the second potential is taken into account is calculated by using as unperturbed the green function the one calculated for the semi-infinite system amd applying the Dyson equartion in the following way,

$$\check{G}_{ab}(x,x') = \check{G}_{a}(x,x') + \check{G}_{a}^{<}(x,x_b)\, U_b \check{\tau}_b \check{G}_{ab}(x_b,x') \tag{2-30}$$

Then using similar procedure as previous section we can find another form of the Dyson equation that depends uniquely of the semi-infinite Green function and other known quantities,

$$\begin{aligned}\check{G}_{ab}(x,x') = \check{G}_{a}(x,x') + \check{G}_{a}^{<}(x,x_b)\, U_b \check{\tau}_b \\ \times \left(1 - \check{G}_{a}^{<}(x_b,x_b)\, U_b \check{\tau}_b\right)^{-1} \check{G}_{a}^{>}(x_b,x'),\end{aligned} \tag{2-31}$$

The Green function can be reduced to the following form after taking the limit of $U_b \to \infty$,

$$\check{G}_{ab}^{LL}(x,x') = \frac{-i}{2\hbar v_F} \sum_{\substack{n,m \\ \varepsilon,\varepsilon'}} f_n^{\varepsilon}(x)\, (\check{w})_{nm}^{\varepsilon\varepsilon'} f_m^{\varepsilon'}(-x')\, \psi_n^{\varepsilon} (\bar{\psi}_m^{\varepsilon'})^T, \tag{2-32}$$

where 6-45 reduces to

$$\check{w}^{>} = \begin{pmatrix} \hat{D}^{++} & \hat{D}^{++}\hat{r}_a^{+-}(x_a) \\ \hat{r}_b^{-+}(x_b)\,\hat{D}^{++} & \hat{r}_b^{-+}(x_b)\,\hat{D}^{++}\hat{r}_a^{+-}(x_a) \end{pmatrix}, \tag{2-33a}$$

$$\check{w}^{<} = \begin{pmatrix} \hat{D}^{++}\hat{r}_a^{+-}(x_a)\,\hat{r}_b^{-+}(x_b) & \hat{D}^{++}\hat{r}_a^{+-}(x_a) \\ \hat{r}_b^{-+}(x_b)\,\hat{D}^{++} & \hat{D}^{--} \end{pmatrix}, \tag{2-33b}$$

with

$$\hat{r}_a^{+-}(x_a) = \hat{f}^{++}(-x_a)\hat{r}_a^{+-}\hat{f}^{--}(x_a), \tag{2-34a}$$

$$\hat{r}_b^{-+}(x_b) = \hat{f}^{--}(x_b)\hat{r}_b^{-+}\hat{f}^{++}(-x_b), \tag{2-34b}$$

$$\hat{D}^{++} = \left[\hat{1} - \hat{r}_a^{+-}(x_a)\,\hat{r}_b^{-+}(x_b)\right]^{-1}, \tag{2-34c}$$

$$\hat{D}^{--} = \left[\hat{1} - \hat{r}_b^{-+}(x_b)\,\hat{r}_a^{+-}(x_a)\right]^{-1}. \tag{2-34d}$$

The later equations allow us to obtain the bound states of the finite region by taking the condition $\hat{D}^{\pm\pm} = 0$, or, analogously, $\hat{r}_a^{+-}(x_a)\hat{r}_b^{-+}(x_b) = \hat{1}$. Consequently, the bound states of the finite region are tied to the reflection matrices at each independent edge.

2.5 Method applied to graphene like materials

2.5.1 Dirac system with zig zag edges

Definitions

The equation 2-7 correspond to the hamiltonian of to the zig zag edge, solving the eigenvalues problem from the hamiltonian we found the energy spectrum for the system, as expressed below

$$E_{\pm,s\eta}(\mathbf{k}) = +\mu_{s\eta} \pm \sqrt{m_{s\eta}^2 + \hbar^2 v_F^2 (k^2 + q^2)}. \tag{2-35}$$

There are a few auxiliar definitions that are going to be frequently used, these are:

$$e^{\pm i\alpha} = \hbar v_F \frac{k \pm iq}{\sqrt{(\mu_{\sigma\eta} - E)^2 - m_{s\eta}^2}}, \tag{2-36}$$

$$N^2 = \frac{\sqrt{E - \mu_{\sigma\eta} - m_{s\eta}}}{\sqrt{E - \mu_{\sigma\eta} + m_{s\eta}}}. \tag{2-37}$$

From the retarded green function we define the spectral density of states as

$$\rho(E, q, x) = \frac{1}{\pi} \operatorname{Tr}\left[\operatorname{Im}\left\{\check{G}(E; q; x, x)\right\}\right], \tag{2-38}$$

and the DOS is then

$$\hat{\rho_T}(E, x) = \int \rho(E; q; x)\, \mathrm{d}q. \tag{2-39}$$

The bulk spectral density adopts the simple form $\hat{\rho} = 1/(\pi\hbar v_F k)$ and it is calculated in figure **2-11** for several infinite layer of graphene-like materials, the DOS is also shown in **2-12**. We now proceed to define and apply the edge potentials to obtain the GF of a semi-infinite and a finite layer, or nanoribbon, with zigzag edges.

Semi-infinite layer

For zigzag edge orientation, the matrix that encodes the boundary conditions for border of A and B atoms are, respectively

$$\check{\tau}_A = \begin{pmatrix} 1 & 0 \\ 0 & 0 \end{pmatrix}, \quad \check{\tau}_B = \begin{pmatrix} 0 & 0 \\ 0 & 1 \end{pmatrix}. \tag{2-40}$$

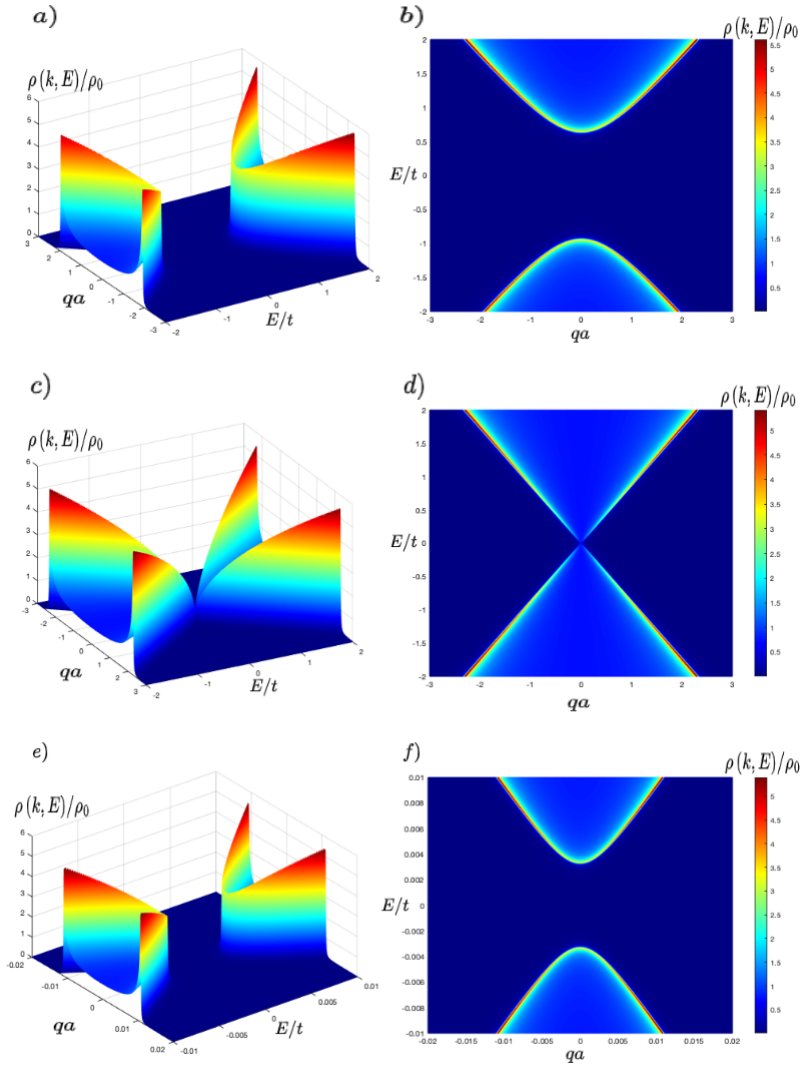

Figure 2-11: spectral density of states (LDOS) for Graphene (A and B), TMDs (C and D) and Germanene (E and F) infinite layer.

The main feature of equation 2-24 corresponds to the inclusion of the coefficients $\hat{r}_a^{+-}$. Referring to equations 2-28 and 2-29, is easy to see $\hat{r}_a^{+-} = (\hat{\tau}_a^{++})^{-1}\hat{\tau}_a^{+-}$, for instance $\hat{\tau}_a^{++}$ corresponds to the projection of matrix $\hat{\tau}$ onto right propagating states and their respective transposed states. Then, $\hat{r}_a^{+-} = -e^{i\alpha}$, for border B the procedure is the same but $\hat{r}_b^{+-} = e^{-i\alpha}$. Finally the coefficient have an additional phase given by the position of the potential,$\hat{r}_a^{+-}(x_a) = -e^{i\alpha-2ikx_a}$, where for border B we have a similar result $\hat{r}_b^{+-}(x_b) = e^{-i\alpha-2ikx_b}$. Pluging $\hat{r}_a^{+-}(x_a)$, into 2-24, is found at $x = x_a$ that $\rho = \text{Im}(iNe^{i\alpha})/\pi\hbar v_F$ and for border B $\rho = \text{Im}(ie^{i\alpha}/N)/\pi\hbar v_F$. For more details regarding previous calculations, refers to 6-73.

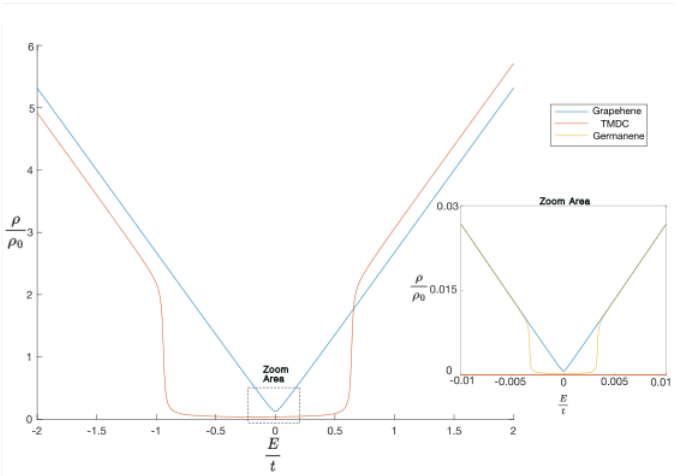

Figure 2-12: DOS for several graphene-like materials. Inset: zoom-in of DOS for germanene showing the lack of states due to the gap generated due to spin-orbit.

The LDOS at the edge of the semi-infinite layer is calculated by using this method for the case of TMDs and Germanane, in **2-13** and **2-14**, respectively.

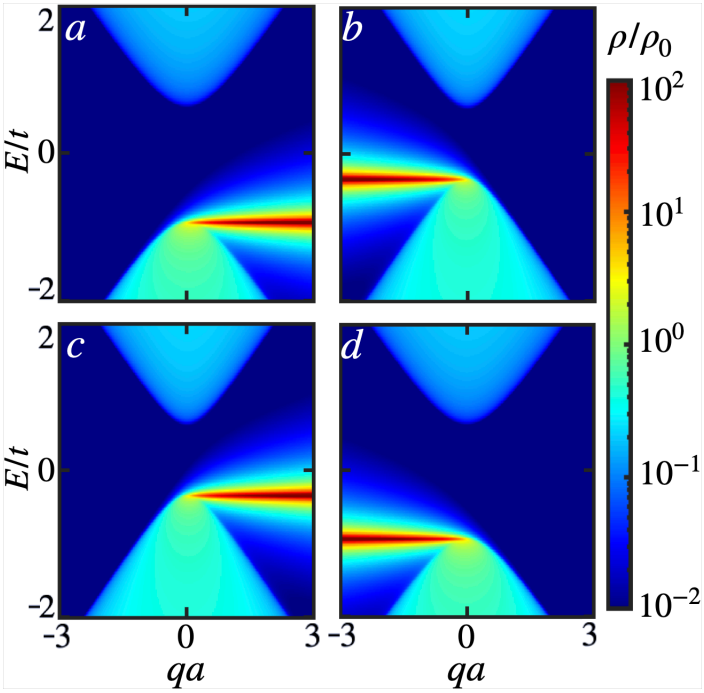

Figure 2-13: Edge LDOS for a semi-infinite monolayer of TMDs, WSe_2. The left and right plot corresponds to LDOS at the valley K' and K, respectively. The top and bottom plots correspond to spin-up and spin-down electrons, respectively.

In both cases, there are gaps, however, for the germanene case, it is at energy scales one hundred

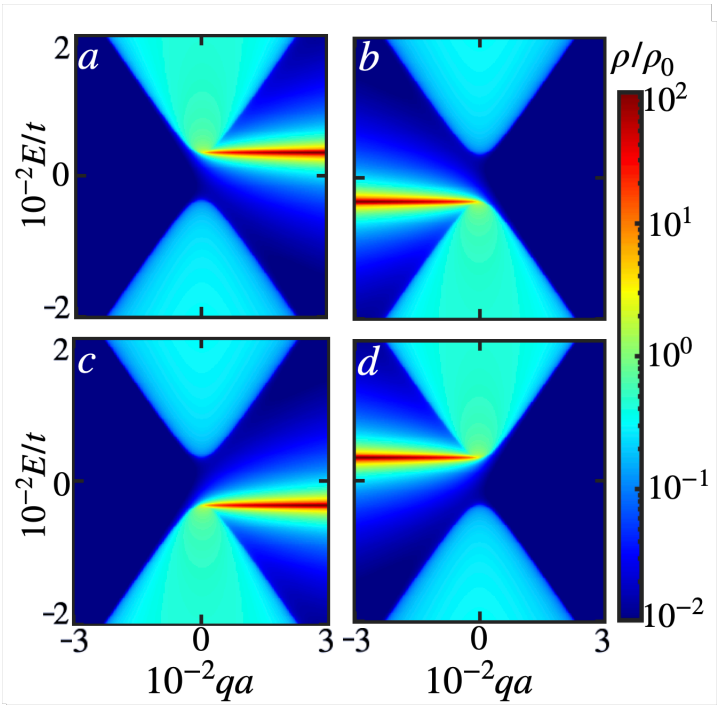

Figure 2-14: Edge LDOS for a semi-infinite monolayer of Germanene. The left and right plot corresponds to LDOS at the valley K' and K, respectively. The top and bottom plots correspond to spin-up and spin-down electrons, respectively.

times lower than TMDs, because of the semiconductor and semi-metallic behavior of TMDs and Germanene, respectively. The asymmetry present in the case of TMDs is due to the combined effect of SOC and intrinsic gap; this contrasts with the symmetry in the case of germanene due to the gap that appears just because of SOC.

A striking features of both figures correspond to the intense state at the border of conduction or valence band. In the case of TMDs, the state is always on the edge of the valance band; it is different for germanene, where the spin up at valley K and spin down at valley K' are in the conduction band and in the valence band for the other cases.

There is a transfer of state in between bands at the edge of each band for the case of TMDs and Germanene. For the TMDs, the transfer is done in between valance bands from different valleys, which means that there is a crossing of the states at the zero of the Brillouin zone, it implies that in the case of spin-up electrons, the transfer is done at opposite velocity respect to the spin-down case. For the Germanene, there is a transfer between the conduction band and valance band, from valley K and K' or vice-versa, depending on the spin orientation; this implies the presence of states that close system's gap at the zero of the Brillouin zone, which means that Germanene is a topological insulator.

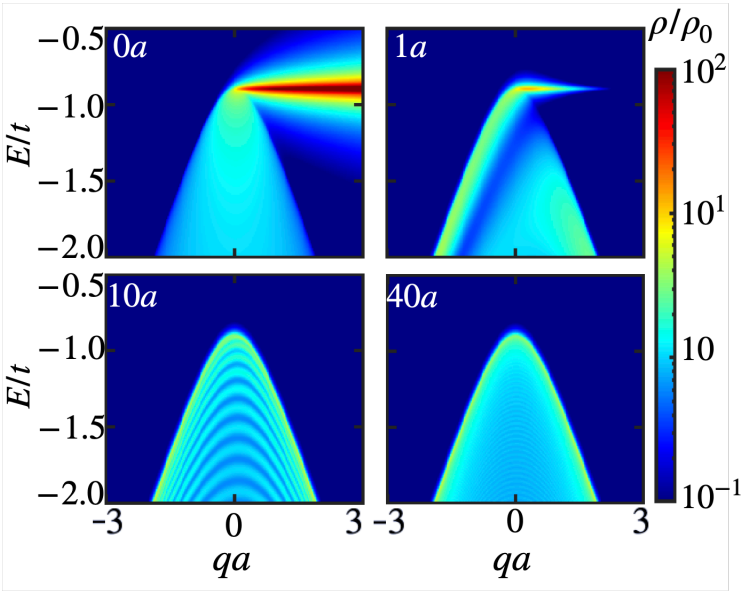

Figure 2-15: LDOS of spin-up electrons at the balance band in the valley K' of a semi-infinite monolayer of TMDs at different positions from the edge.

In figure **2-15** is shown what happens when LDOS is calculated for different distances from the edge of the semi-infinite layer. The figure **2-15** shows that the intense state at the border of the valence band is highly concentrated at the edge of the semi-infinite layer. At 10 unit cells away from the edge, the behavior shows a periodic concentration of the states, and for 40 unit cells from the border, the LDOS behaves as the case of an infinite layer. .

The figure **2-16** summarizes the obtained spectral properties of zigzag germanene, **2-16**(a), and TMDs, **2-16**(c), showing the lowest energy spin-valley bands and the dispersion of the edge states (red and blue lines). Notice the important inversion of the bands when the nanoribbon edge type is changed from A to B in **2-16**(a). Analogously, we also sketch the lowest band dispersion for armchair germanene, **2-16**(b), and TMDs, **2-16**(d). We explore this edge termination in more detail below

Nanoribbon

For this case we will build the Green function given by refeq:finite-GF, to do so we have to look for the terms which define the equation 2-33 and 2-34. We already have found $\hat{r}_a^{+-}(x_a)$ and $\hat{r}_b^{+-}(x_b)$. By doing a similar process as before we are able to find the $\hat{r}_{a,b}^{-+}(x_{a,b})$ coefficients, which are $\hat{r}_a^{-+}(x_a) = -e^{-i\alpha+2ikx_a}$ and $\hat{r}_b^{-+}(x_b) = e^{i\alpha+2ikx_b}$. Plug in the coefficients into 2-33 and 2-34 and we are able to find at the edge A at x_a 2-32, given by

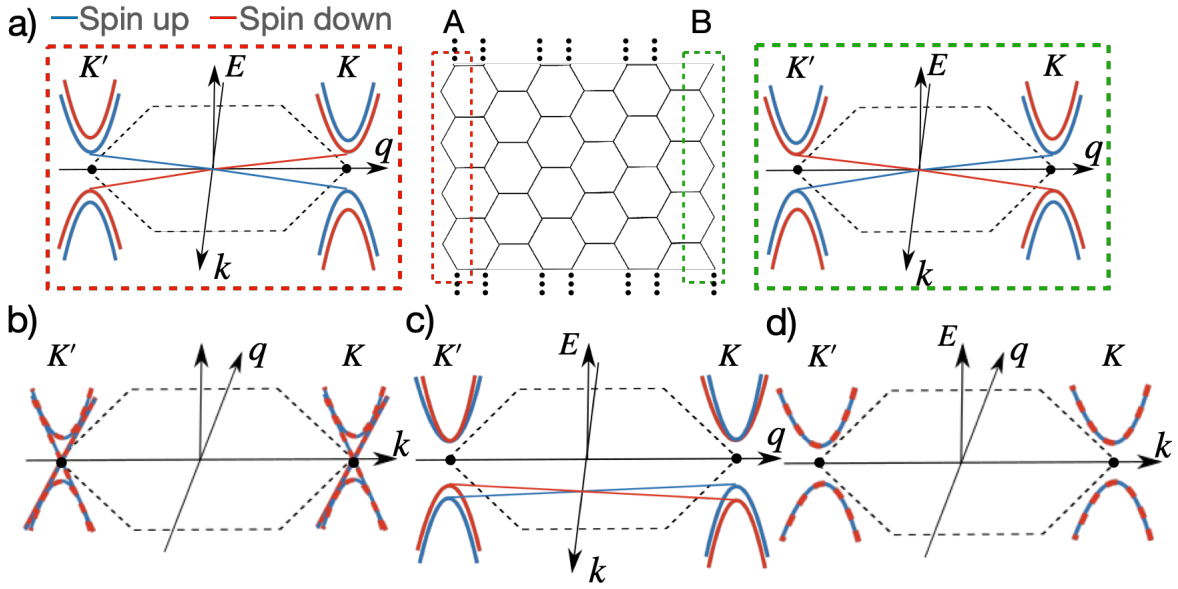

Figure 2-16: Summary of the different band dispersion for TMDs and germanene nanoribbons. a) Sketch of the honeycomb lattice of a zigzag nanoribbon (middle) and band dispersion for the A (left in red) and B (right in green) type of terminations, for germanene nanoribbons. b) Edge electronic band structure for armchair germanene. c,d) Edge electronic bands of a TMDs nanoribbon with zigzag (c) or armchair (d) edges.

$$\check{G}^{>}_{ab}(x_a, x_a) = \begin{pmatrix} 0 & -i\frac{1+e^{2i(\alpha+kW)}}{1+e^{2i(\alpha+kW)}} \\ 0 & -iN^2 e^{i\alpha}\frac{1-e^{i2kW}}{1+e^{2i(\alpha+kW)}} \end{pmatrix} \tag{2-41}$$

Then ρ in the edge is,

$$\rho(x_a) = \frac{1}{\pi\hbar v_F}\,\mathrm{Re}\left(\frac{N^2 e^{i\alpha}\left(1-e^{i2kW}\right)}{1+e^{2i(\alpha+kW)}}\right) \tag{2-42}$$

In previous equations, 2-42 and 2-41, W corresponds to $x_b - x_a$. When, $W \to \infty$ then the result in 2-42 is equal to the semi-infinite layer case.

Features such as intense states at the edge of bands and electronic properties for the semi-infinite layer are observed in the case of a nanoribbon, as shown in **2-17**. In the figure, the gap on the germanene is not observed due that for both cases the energy scale is the same. The interesting behavior corresponds to the fact that the states are concentrated in sub-bands that appears periodically, and this periodicity depends on the width of the nanoribbon.

The figure **2-18** shows the behavior of the states when one end of the nanoribbon tends to infinity, i.e. when tends to a semi-infinite layer, as mentioned before this reinforces the fact that the nanoribbon case has all the features from a semi-infinite layer. Upon this, another

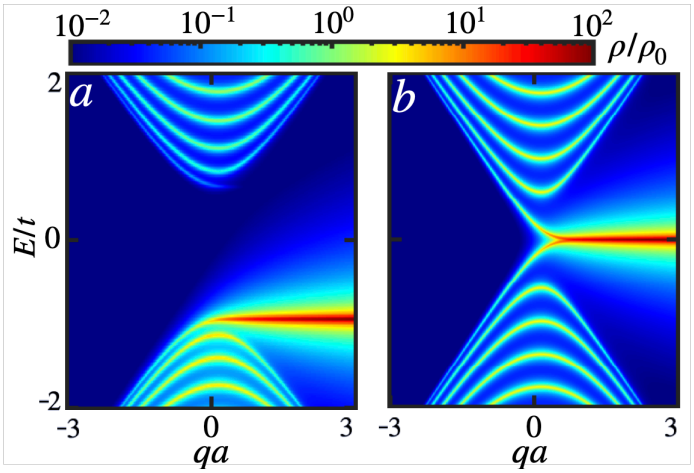

Figure 2-17: Edge LDOS for TMDs (left) and Germanene (right) for a nanoribbon monolayer with a width equal to four unit cells, in both cases, the LDOS corresponds to electrons at valley K' and with spin up.

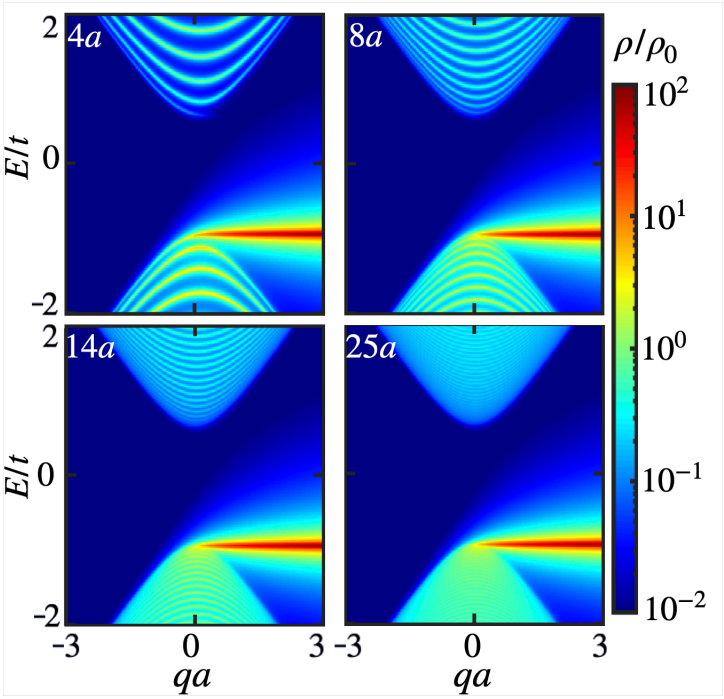

Figure 2-18: Edge LDOS for nanoribbon monolayer of TMDs with electrons at the valley K' with spin up. Each case corresponds to different nanoribbon width.

remarkable property corresponds that the number of sub-bands is the same number of units of cell width for the nanoribbon.

2.6 Dirac system with armchair edges

General Definitions. The hamiltonian in this case is:

$$\check{H}_{s\eta}\left(\mathbf{k}\right) = \mu_{s\eta}\hat{\sigma}_0 + \hbar v_F\left(q\hat{\sigma}_y - \ \eta k\hat{\sigma}_x\right) + m_{s\eta}\hat{\sigma}_z \tag{2-43}$$

There is a direct change in the structure of the system's eigenfunction due to a nonnormalizable phase given by x direction boundary conditions and the inclusion of a new degree of freedom given by the valley index, which explicitly increase the dimensionality of the spinors by a factor of two, one valley respect another is distinguished by a $'$, when this notation appears transforms in the following way, $k_x \to -k_x$, $e^{i\alpha} \to -e^{-i\alpha}$ and $e^{-i\alpha} \to -e^{i\alpha}$, also when this notation appears holds $\eta = -1$. As before, the orthogonal and transposed states are calculated as described in equations 2-14 and 2-19 , but in this case

$$\check{\alpha}_x = \begin{pmatrix} \hat{\sigma}_x & 0 \\ 0 & -\hat{\sigma}_x \end{pmatrix}. \tag{2-44}$$

$$\check{\gamma} = \begin{pmatrix} \hat{\sigma}_z & 0 \\ 0 & -\hat{\sigma}_z \end{pmatrix}. \tag{2-45}$$

This is consequent with the increase of the dimensionality in the spinors states. Full eigenfunctions are shown in 6-79, 6-80, 6-81, 6-82 and 6-83 in the appendix.

2.6.1 Semi-infinite.

For this case the structure of the matrix which encodes the boundary conditions for border A is a bit more complex than for zig-zag case,

$$\check{\tau} = \begin{pmatrix} \hat{\sigma}_x & \hat{\sigma}_x \\ \hat{\sigma}_x & \hat{\sigma}_x \end{pmatrix}. \tag{2-46}$$

As before, we are looking for equation 2-24, at the edge has the form of

$$\check{G}^{<}_{RR}\left(x_0, x_0\right) = \begin{pmatrix} \hat{M}^{--}_{11} + r^{+-}_{11}\hat{M}^{+-}_{11} & r^{+-}_{11'}\hat{M}^{+-}_{11'} \\ r^{+-}_{1'1}\hat{M}^{+-}_{1'1} & \hat{M}_{\tilde{1}'\tilde{1}'} + r^{+-}_{1'1'}\hat{M}^{+-}_{1'1'} \end{pmatrix}. \tag{2-47}$$

Where,

$$\hat{M}^{\epsilon\epsilon'}_{nm} = \psi^{\epsilon}_{n}(\bar{\psi}^{\epsilon'}_{n})^{T} \tag{2-48}$$

As before we are interested in $\hat{r}^{+-} = (\hat{\tau}^{++})^{-1}\hat{\tau}^{+-}$ and $\hat{r}^{-+} = (\hat{\tau}^{--})^{-1}\hat{\tau}^{-+}$, however, in this case, they are matrices where each entry corresponds to the projection of the matrix into the valley degree of freedom, for instance, the entry $\hat{r}^{+-}_{11'}$ of $\hat{r}^{+-}$ corresponds to the reflection amplitude of a propagate state from the right to the left which goes from valley K to K'. Then doing the

calculations similarly to the zig-zag case, we can find that for example the coefficient r_{11}^{+-} holds that $r_{11}^{+-} = \frac{h_{11'}^{++}}{h_{11'}^{-+}}$ where $h_{nm}^{\epsilon\epsilon'} = \tilde{\varphi}_n^{\epsilon\dagger}\varphi_m^{\epsilon'}$, here ϵ and ϵ' can be $+$ or $-$, n and m can be K or K'. This means that each coefficient correspond to the projection of one state into another. Then taking into account the calculated coefficients as described before, we can calculate the spectral density of states:

$$\rho(E,q) = \text{Re}\left(\frac{4(1+e^{i(\alpha-\alpha')})N^2N'^2}{\pi v_F\hbar(N^2e^{i\alpha}+N'^2e^{-i\alpha'})}\right). \tag{2-49}$$

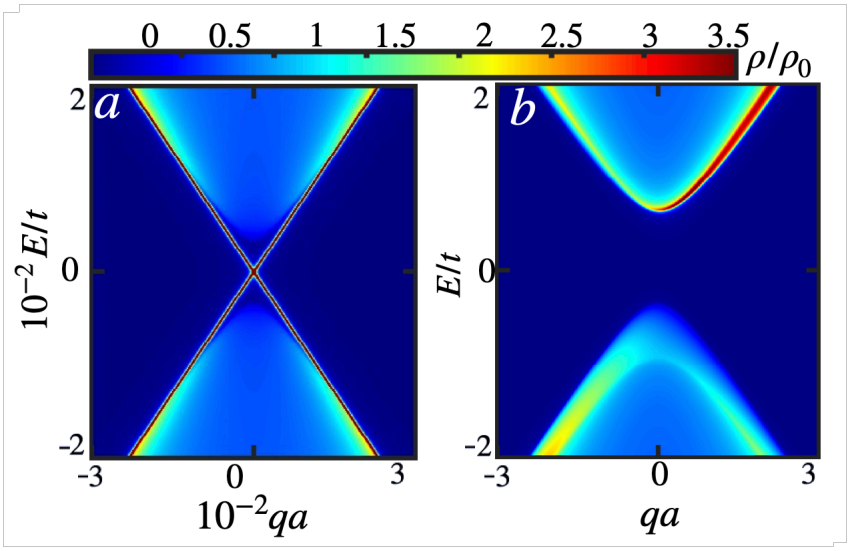

Figure 2-19: Edge LDOS for Germanene (left) and TMDs (right) armchair semi-infinite monolayer.

In figure **2-19** the LDOS from the semi-infinite armchair system is presented. The case of TMDs presents an asymmetry respect q which is not presented in the case of the germanene, this comes from the effects of the combined effect of spin-orbit coupling and the intrinsic electronic gap. In addition to this is worth mentioning that in the case of germanene, there is a concentrated state that closes the gap, which reinforces the fact that the germanene behaves as a topological insulator independently of the edge orientation; this is not shared by TMDs, which shows a semiconductor behavior.

In figure **2-20** is shown the coefficient reflection amplitude at $q = 0$ for intervalley and intravalley dispersions for TMDs and Germanene at a semi-infinite monolayer. The germanene shows that the intravalley processes are mainly concentrated at the edge of each band, this is a behavior that is equivalent to previous results reported for graphene. In contrast, TMDs show that the intravalley processes are dependent on the valley index, in valley K' the reflections are saturated at the valence band with states concentrated in a region of energy two times bigger than in valley K where the processes occur at the conduction band. Finally, for both materials, the intervalley processes are saturated with the increase of the absolute value of energy.

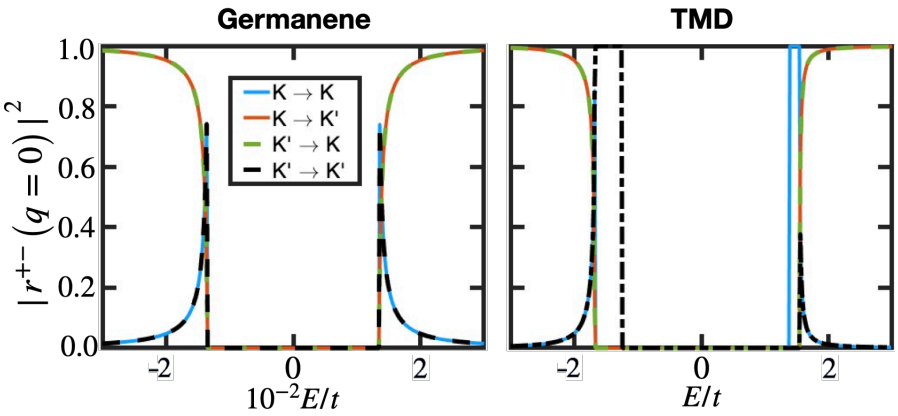

Figure 2-20: Electron reflection coefficient at the armchair border of a semi-infinite monolayer of Germanene and TMDs at $q = 0$. In this plot intravalley (blue and black) and intervalley (red and green) scattering are shown.

2.6.2 Nanoribbon.

the Green Function Matrix corresponds to a 16×16, where each entry can be understand as a 4×4 matrix projected in the valley space, for example, the first entry:

$$G^{>}_{KK}(x,x') = \hat{f}^{++}_{11}(x,x')\,\hat{r}^{>,++}_{11}\hat{M}^{++}_{11} + \hat{f}^{--}_{11}(x,x')\,\hat{r}^{>,--}_{11}\hat{M}^{--}_{11} + \hat{f}^{+-}_{11}(x,x')\,\hat{r}^{>,+-}_{11}\hat{M}^{+-}_{11} + \hat{f}^{-+}_{11}(x,x')\,\hat{r}^{>,-+}_{11}\hat{M}^{-+}_{11}. \quad (2\text{-}50)$$

In the previous equation, the reflection coefficient has a complex structure as shown in 2-33. A complete description of each entry for GF for this kind of system is presented in the supplementary material.

Numerically implementation for the closed form of GF for this system allows us to find the LDOS as shown in **2-21**, on here we observe the same periodical band behavior of the LDOS for nanoribbons of TMDs and Germanene of 6 unit cells width. Similarly to the case of a semi-infinite layer, we have a state that closes the gap in the germanene layer for the nanoribbon. This is not surprising because the properties of the semi-infinite case are shared with the case of a nanoribbon layer. However, there is an additional striking effect that is found in this type of system, In **2-22**, when the width of the germanene layer is multiple of 3, the germanene is a topological insulator, otherwise the sub bands split and degerancy is broken, this last behavior also happens for the case of a TMDs.

2.7 Germanene Voltage Manipulation

Now, let's assume there is an electric field applied perpendicular to a sheet of Germanene. In this context, we focus on a semi-infinite monolayer of Germanene.

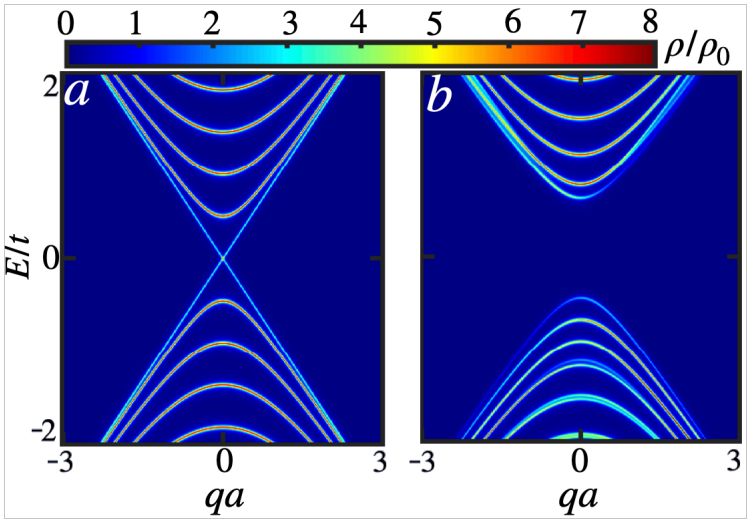

Figure 2-21: Edge LDOS for Germanene (left) and TMDs (right) armchair nanoribbon monolayer.

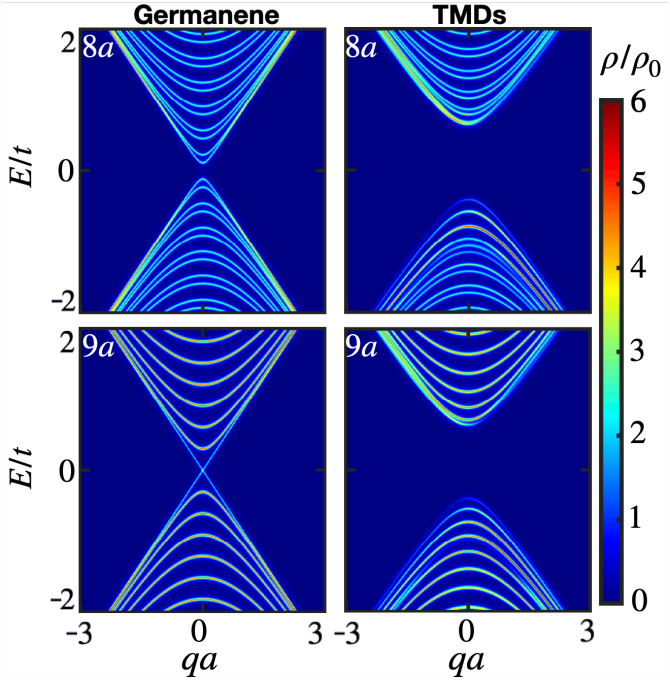

Figure 2-22: LDOS at the armchair edge of Germanene and TMDs nanoribbon monolayer for widths of eight unit cells (top) and nine unit cells (bottom).

Calculating the DOS as appearing in **2-23** for different voltages we are able to observe that in a region where the voltage is around from $-\Delta \times 10^{-3}$ to $\Delta \times 10^{-3}$, Germanene behaves as Topological insulator. For higher voltages behave as a semiconductor and then as an insulator.

As can be observed in LDOS for several voltages **2-24**, when the voltage is increased, the state

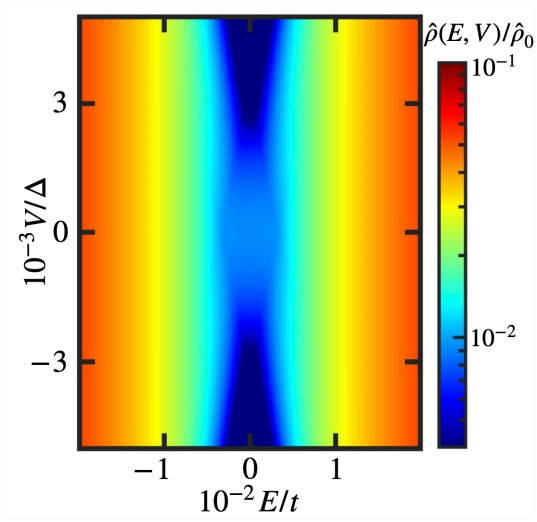

Figure 2-23: Edge DOS of a semi-infinite armchair monolayer of Germanene subjected continuously to different perpendicular voltages

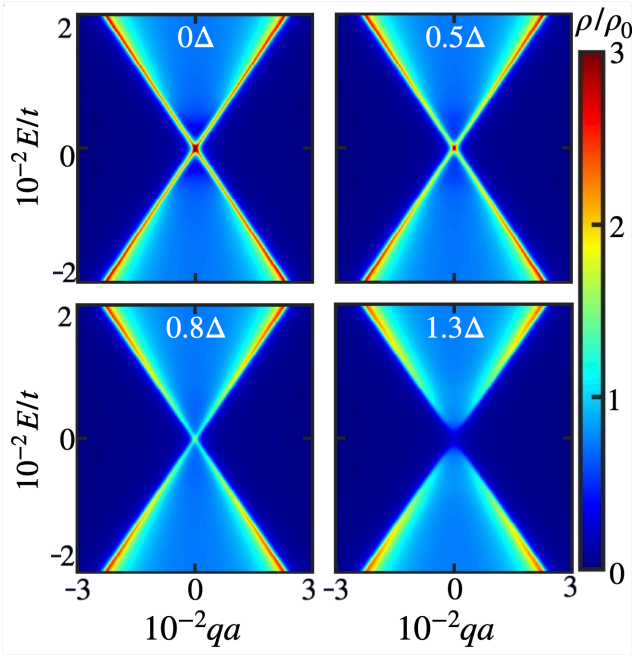

Figure 2-24: Edge LDOS for semi-infinite germanene armchair monolayer subjected to different perpendicular voltages to the monolayer

at the gap gets less intense until the gap is closed, but the system behaves as a semi-metallic material when the voltage is equal to the magnitude of the system's gap, and then for magnitudes of a voltage higher than the amplitude of the system behaves as a semiconductor.

In **2-25** we present the DOS at zero energy when the SOC and the applied voltage are tuned.

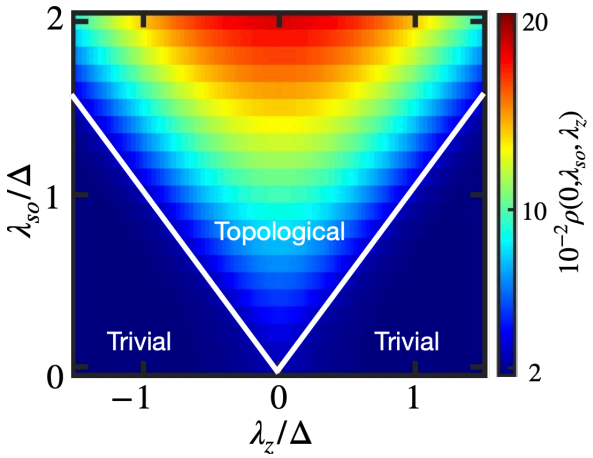

Figure 2-25: DOS at zero energy for a semi-infinite armchair monolayer of Germanene subjected to several voltages and with tunable spin-orbit coupling.

Regarding recently developed methods for gap engineering [83, 84] it is interesting to understand the electronic behavior of these materials due to this effect, given that in the zero-energy we are able to observe the presence of the topological state, we focus on that particular spot to assess how the intensity of the state change according with this parameters. This plot clearly identifies the topological region and the non-topological ones.

2.8 Summary

- Our method allows us to study infinite, semi-infinite, and nanoribbon systems based on Dirac materials, considering boundary conditions and physical properties of the system; in the graphene-like case, our method allows us to account for the zig-zag and armchair edges, as well as physical properties of relevant graphene-like materials such as spin-orbit coupling, valley-spin coupling, intrinsic gap.

- Our findings for the case of graphene-like materials reveal the possibility of finding closed-form results and analytical results that allow us to numerically calculate with low computational cost quantities such as reflection coefficients, LDOS, and DOS.

- Our results show that Germanene in normal conditions behaves as a topological insulator when the boundary conditions correspond to a zig-zag and armchair. In addition, we find that TMDs behave as a semiconductor with spin-valley locking in LDOS maps, this behavior shows a spin-valley dependent in the scattering process for this type of semiconducting 2D material.

- Further exploration of topological phases in Germanene by applying an external electric

field, shows that the topological state at zero energy is robust to external field perturbation, however, there is a range of voltage where this is true.

- Some miscellaneous findings correspond to the fact that for a nanoribbon of TMDs or Germanene, there is tuning in the degeneracy of orbital-like levels depending on the divisibility of the width of the nanoribbon, for width multiples of three there is degeneracy for both and the presence of a topological state for germanene, in other cases the orbital degeneracy is broken and a couple of orbital appears close to each other. Our simulations shows that in the limit where one edge of a nanoribbon tends to infinitely our results tend to the semi-infinite case, this shows that most of the principal features are shared by nanoribbon and semi-infinite system; the key difference rests in the fact that for the nanoribbon system, orbital-like states appear in the LDOS, either for TMDs or Germanene.

3 Quantum Magnetic Imaging based on Nitrogen-Vacancy center in diamond to explore Van der Waals material

3.1 Introduction

Van der Waals (vdW) material such as Fe_5GeTe_2 (FGT) and Cobalt substituted materials, like Co-FGT with their long-range ferromagnetic ordering near room temperature, has significant potential to become a platform for implementing novel spintronic and quantum devices [85]. To enable their applications, it is crucial to determine the magnetic properties when the thickness of such materials reaches the few-layers regime[86]. However, this is highly challenging due to the need for a characterization technique that is local, highly sensitive, artifact-free, and operational with minimal fabrication. Prior studies have indicated that Curie temperature T_C can reach up to close to room temperature for exfoliated Fe_5GeTe_2 flakes, as measured via electrical transport [87, 85]; there is a need to validate these results with a measurement that reveals magnetism more directly.

On the other hand, although Fe_nGeTe_2, with $n = 3, 4, 5$, have demonstrated to have room temperature T_c, there is still a need to extend the portfolio of materials that offer these magnetic properties at room temperature. In previous work, has been demonstrated that Fe_5GeTe_2 offers diverse rich properties when is Cobalt substituted (CFGT), for example, it could be an antiferromagnet or a polar ferromagnet if the concentration of cobalt is above 40%, also when there is a presence of around 30% previous results have shown the increase of the Curie temperature in bulk material indicating the potential for above-room-temperature ferromagnetism in thin Fe_5GeTe_2 with intermediate Cobalt substitution [88, 89, 90]. However thin flakes generally have lower T_C compared to bulk crystals, hence appears the question of if CFGT flakes are able to exhibit room-temperature magnetism remains to be explored.

Nitrogen Vacancy (NV) centers in diamond are a quantum system used for sensing purposes that function at ambient conditions, and have magnetically, electrically, and thermally sensitive electronic spin ground states with long coherence lifetimes[91, 92]. The NV spin state can be initialized, and the evolution of the spin states can be detected optically, thus allowing precision

sensing of magnetic fields and other effects. Magnetic field sensitivity and spatial resolution are determined by the number of NVs in the sensing volume, the resonance linewidth, the resonance spin-state fluorescence contrast, the collected NV fluorescence intensity, and the NV-to-sample separation [93, 94].

Variation of the experimental setup and measurement protocol allows NV-diamond magnetic imaging to be adapted for a wide range of applications in different fields of research[95, 96]. Although the desired capabilities for each magnetic imaging application vary widely, common requirements include good field sensitivity within a defined frequency range, fine spatial resolution, large field of view, quantitative vector magnetometry, wide field and frequency dynamic range, and flexibility in the bias field and temperature during measurement[97].

Previous described properties and qualities from NV center in diamond magnetometry make it suitable for exploration of magnetic properties in thin flakes of FGT and CFGT. In the next section, we make an overview of quantum diamond microscopy, then the description of the experimental methods implemented to study FGT and CFGT samples are fully explained after the results are discussed and finally the conclusion and outlook are presented.

3.2 Overview of Quantum Diamond Microscopy

3.2.1 Crystal and Electronic Structure of NV centers in diamond

The NV center in diamond consists of substitutional nitrogen adjacent to a vacancy in the carbon lattice as shown in figure **3-1**A. Although NV centers can exist in three charge states (NV^-, NV^0, NV^+), only the negatively-charge state, NV^-, with two unpaired electrons, is conventionally used for sensing. Well protected inside the diamond lattice, a negatively-charged NV has six electrons, with two electrons from nitrogen, one electron from each of the three carbon atoms, and an additional electron from the lattice. These electrons occupy four sp^3 atomic orbitals with electronic spin quantum number $S = 1$. These sp^3 orbitals linearly combine to form four molecular orbitals comprising the ground electronic configuration.

The lowest energy state of the ground configuration is the orbital singlet, spin triplet state, $^3A_2$, which has fine, Zeeman, and hyperfine structures in their electronic transition states, in figure **3-1**B are shown fine and Zeeman splitting. The four molecular orbitals also give rise to electronically excited states: orbital-doublet spin-triplet ^3E, and spin-singlet orbital-singlet $^1A_1$ shown also in figure **3-1**B [100].

The ^3E is coupled to the $^3A_2$ ground state by an optical 637 nm zero-phonon line (ZPL). The $^3E \leftrightarrow {}^3A_2$ have a radiative transition that generally conserves the electron spin state ms as a result of

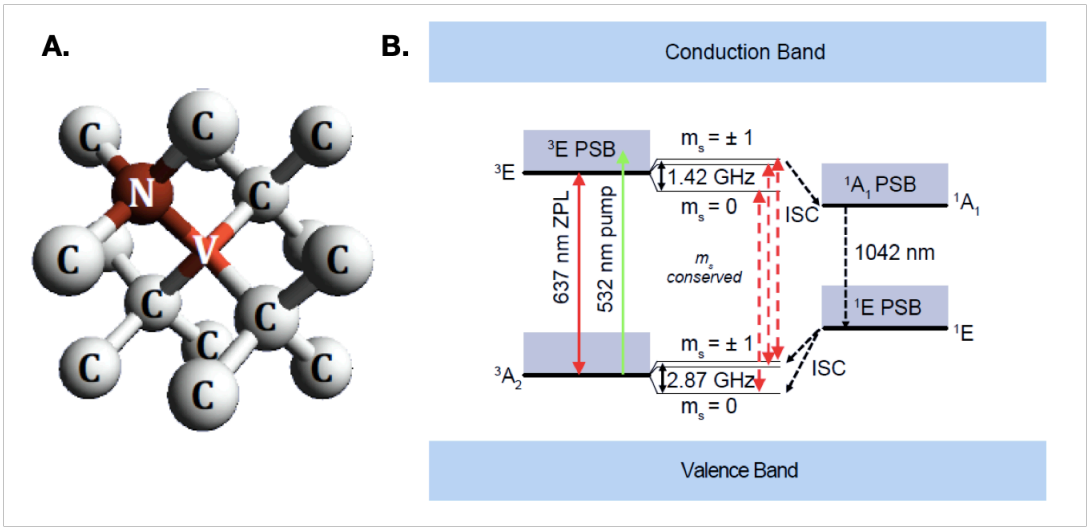

Figure 3-1: Crystalographic and electronic structure of NV centers in diamond. A.) Pictorial representation of the nitrogen and a vacancy in the diamond lattice. B.) Representation of electronic structure of NV centers showing optical pumping excitation (green arrow), spin conserving energy levels transition (red arrows) and intersystem crossing pathway (dashed black arrows.). Adapted from [98, 99]

weak spin-orbit interaction[101]. The $^3E \rightarrow {}^3A_2$ ($^3A_2 \rightarrow {}^3E$) transitions works for longer [shorter] wavelengths in fluorescence [absorption] as a result of the phonon sideband (PSB) [**?**]. The **3-1**B also shows the radiative, spin conserving $^1E \leftrightarrow {}^1A_1$ transition which has an infrared 1042 nm ZPL and its own sideband structure.

Nonradiative transitions between states of different spin multiplicity exist between ^3E and $^1A_1$, and between ^1E and $^3A_2$. These nonradiative transitions are caused by an electron-phonon mediated intersystem crossing (ISC) mechanism and do not conserve spin. The probability of the ISC transition occurring for the ^3E to $^1A_1$ is only non-negligible for $m_s = 1$ states of ^3E and is characterized by the ISC rate of transition. Similarly, the ISC transition probability from ^1E to the $m_s = 0$ state of $^3A_2$ is approximately 1.1 to 2 times that of the ISC transition from ^1E to the $m_s = 1$ states of $^3A_2$. These state-selective differences in the ISC transition rate allow for spin polarization of the NV under optical excitation, typically from 532 nm laser illumination, the photodynamics of light emitted by NV centers when no field is applied due to previous described spin-fluorescence dependent is shown in figure **3-2** [92, 102]

3.2.2 Spin polarization and optical pumping

In order to realize measurements using NV centers, initially an optical driving field from a pump laser is applied in order to spin polarize the NV electronic state. This pump laser is also used at the end of measurement to read out the final NV spin state through the fluorescence intensity.

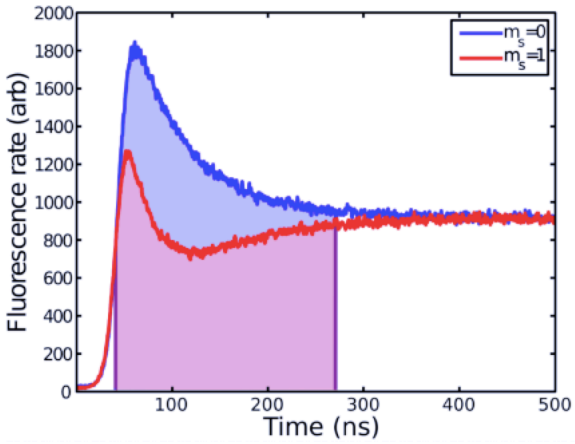

Figure 3-2: NV centers spin photodynamics. NV^- centers prepared in the ms= 0 state emit more photons than centers prepared in the ms=1 states. This spindependent fluorescence forms the basis of conventional NV^- readout. [103]

The NV optical pumping takes advantage of the m_s selective nonradiative ISC decay pathway. An NV that is optically excited from $^3A_2$ to ^3E state by a 532 nm photon, decays along either the optically radiative $^3E \rightarrow {}^3A_2$ pathway or the non-optical, ISC mediated by $^3E \rightarrow {}^1A_1 \rightarrow {}^1E \rightarrow {}^3A_2$ pathway.

The m_s-selectivity of the ISC will preferentially depopulate the $m_s = +1$ spin projection states. NVs starting in the $^3A_2$ $m_s = +1$ sublevel are eventually pumped (on average, after a few pump photon absorption cycles) into the $^3A_2$ $m_s = 0$ sublevel. Typically only $\sim$ 80% of NVs in an ensemble can be initialized into the $m_s = 0$ state, where they remain in a cycling transition[104, 105, 106]. The ^1E state is metastable with a $\sim$ 200 ns lifetime at room temperature. The ^3E upper state has a $t_{^3E} \sim 13$ ns lifetime, and the $^3A_2 \rightarrow {}^3E$ absorption cross section at $\lambda = 532$ nm is $\sigma = 3.1 \times 10^{-17}$ cm^2 (although there is disparity in the reported 532 nm absorption cross-section value and saturation intensity). Considering this quantities it is possible the intensity needed to saturate the excited state using the equation $(\hbar c)/(\lambda \sigma t_{^3E}) \approx 0.9$ MW/cm^2, where c is the speed of light [107, 108].

The ISC is also responsible for the reduced fluorescence intensities of NVs in the $m_s = \pm 1$ sublevels, since they emit fewer optical photons when returning to the $^3A_2$ state through the ISC mediated pathway. The fractional fluorescence difference between NVs in the $m_s = \pm 1$ sublevels and NVs in the $m_s = 0$ sublevel is called the fluorescence contrast and can be as large as $\sim$ 20% for a single NV [109]. The fluorescence intensity from an optically pumped NV diamond chip, therefore, indicates the percentage of the NVs in the $m_s = 0$ state, or in the $m_s = \pm 1$ states. A transition of NVs from the $m_s = 0$ to the $m_s = \pm 1$ state, e.g., induced by a resonant MW field, drops the fluorescence as more NVs follow the ISC-mediated decay

transition. This is the mechanism underlying optical readout using NV centers in diamond as sensors.

3.2.3 Ground state hamiltonian

The NV centers in diamond as a sensor uses their spin-state-dependent fluorescence from electronic state transitions to detect changes to the $^3A_2$ ground state configuration that result from coupling to a sample magnetic field. Therefore, focus is placed on the physics of the $^3A_2$. The NV centers have C_{3v} point-group symmetry, and are spatially invariant under the C_{3v} symmetry transformations. NV centers also have a quantization axis along the NV avis, usually in that orientation z-axis is placed [110].

The $^3A_2$ electronic ground state is an orbital singlet and spin triplet with ground state hamiltonian,

$$\frac{\hat{H}_{gs}}{\hbar} = \hat{S} \cdot \mathbf{D} \cdot \hat{S} + \hat{S} \cdot \mathbf{A} \cdot \hat{I} + \hat{I} \cdot \mathbf{Q} \cdot \hat{I} \tag{3-1}$$

where $\hbar$ is Planck's constant and $\hat{S} = \left(\hat{S}_x, \hat{S}_y, \hat{S}_z\right)$ and $\hat{I} = \left(\hat{I}_x, \hat{I}_y, \hat{I}_z\right)$ are the dimensionless electron and nitrogen nuclear spin operator, respectively. The first term is the splitting due to the electronic spin-spin interaction known as fine structure, where **D** is the fine structure tensor. The second term correspond to the interaction in between the NV electrons and the nitrogen nucleus mediated by the **A** tensor. The last term correspond to the nuclear electric quadrupole interaction where **Q** is the electric quadrupole tensor [111, 91]. The tensors are diagonal in the NV coordinate of system, then the hamiltonian can be written as,

$$\frac{\hat{H}_{gs}}{\hbar} = D(T)\left[\hat{S}_z^2 - \hat{S}^2/3\right] + A^{\parallel}\hat{S}_z\hat{I}_z + A^{\perp}[\hat{S}_x\hat{I}_x + \hat{S}_y\hat{I}_y] + P\left[\hat{I}_z^2 - \hat{I}^2/3\right] \tag{3-2}$$

Here, $D(T)$ is the fine structure term called the zero-field splitting (ZFS), $A^{\parallel}$ and $A^{\perp}$ are the axial and transverse hyperfine terms, and P is the nuclear electric quadrupole component. Two important features of the ground states are evident from the Hamiltonian. First, in the electronic state $^3A_2$ the sublevels $m_s = \pm 1$ and $m_s = 0$ have difference in energy equals to $D(T)$, which depends on the temperature because the electronic spin-spin interaction changes with the lattice spacing, at room temperature $D(T) \sim 2.87$ GHz and it change linearly with temperature $dD/dT \approx -74.2$ kHz/K at room temperature. Second, the $^3A_2$ electronic states have an additional hyperfine energy splitting due to nitrogen nucleus, where $I = 1$ and $I = 1/2$ correspond to nitrogen isotopes ^{1}4N and ^{1}5N respectively [112]. In this case the hyperfine parameters are $A_{14N}^{\parallel} \approx -2.14$MHz, $A_{14N}^{\perp} \approx -2.70$MHz, $P_{14N} \approx -5.01$MHz, $A_{15N}^{\parallel} \approx 3.03$MHz, $A_{15N}^{\perp} \approx 3.65$MHz [113, 105, 114, 115].

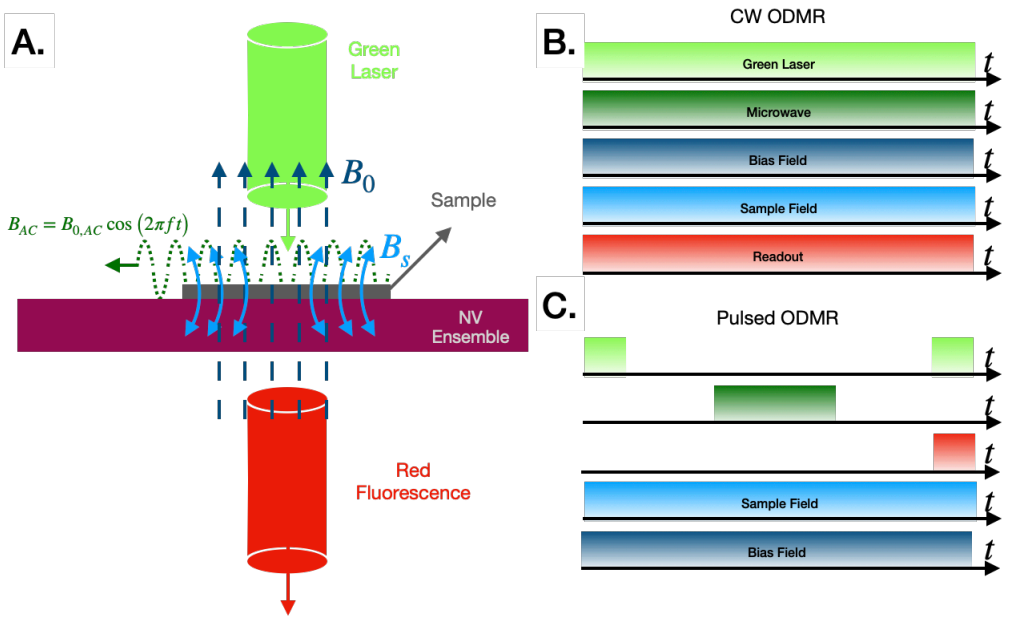

Figure 3-3: Schematics of NV ensemble quantum magnetic sensing and typical protocols. A. Diagram representing typical sensing measurement with NV enters. In this target sample field (in light blue), bias magnetic field (dark blue), MW field (doted green), green laser light and red fluorescence are presented, as well as NV ensemble and sample. B. CW-ODMR protocol C. Pulsed ODMR protocol with a predefined spam of time for the microwave pulse.

3.2.4 Optically detected magnetic resonance in NV ensemble

Optically detected magnetic resonance (ODMR) is a robust and simple method that can determine a magnetic field's vector components when applied over an NV center. Due to easy implementation, ODMR is the most common technique used for magnetometry applications with NV centers in diamonds. The technique can be pictured as a continuous green laser pumping, with a sweeping Microwave (MW) driving field with frequency f, a known bias magnetic field and fluorescence readout, are performed simultaneously as shown in figure **3-3**A. In the figure, the NV ensemble refers to the synthetic diamonds with NV centers distributed in the crystal structure, when it is doped with NVs it tends to have a purple color due to red spontaneous fluorescence.

The laser is used to pump the NVs into the ms = 0 spin state and probe the population's spin states via the NV red fluorescence. The frequency of the MW drive is swept in time and synchronized with the readout. A decrease in fluorescence occurs when the MW frequency matches the NV resonance due to the spin state dependence of NV photon emission described previously when the external magnetic field, i.e. sample and bias field, is applied. When the technique is applied continously is called Continuous-wave ODMR (CW ODMR), the sequence of each ap-

plied quantity is shown in figure **3-3**B, where the sample field is the quantity to be determined by using the resonance frequency f.

CW ODMR suffers from laser repumping of the NV spins through the entire measurement. This simultaneous laser pumping and MW drive spoil the measurement sensitivity as a result of the competing processes of initializing the spin state (laser) and driving transitions (MW drive). In order to mitigate this power broadening, a pulsed ODMR protocol uses a temporally separated laser initialization, a MW control π-pulse with time T_π, and a laser readout pulse as demonstrated in **3-3**C. This leads to the decreased linewidths as compared to CW ODMR. Alteration of the MW power changes the necessary duration, T_π, of a π-pulse, and must be optimized to balance linewidth and contrast of ODMR resonance features. As well as these methods, there are additional protocols for static and AC magnetic fields, which will not be discussed in this document, for more information refers to [97].

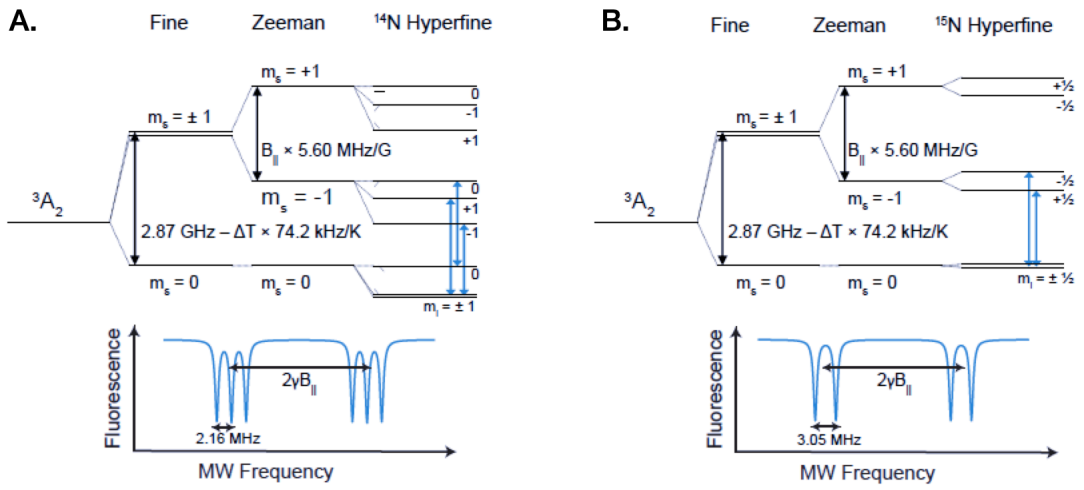

Figure 3-4: Electronic energy levels depending on the nucleas spin of the nitrogen isotope and expected ODMR spectrum depending on it. A. Nitrogen 14 and B. Nitrogen 15 [99]

Figure **3-4** shows an example of when a magnetic field parallel to NV axis is applied to the system $\mathbf{B}_{\|}$, producing several minimums around a center frequency when there is resonance, the number of minimum around a particular frequency is due to hyperfine interaction with N^{14} and N^{15} as shown in figure **3-4**, where hyperfine sublevels are also shown. For an NV ensemble, the resonance lineshape – often modeled as a sum of multiple Lorentzians or Gaussians – is parametrized by the center frequency, linewidths, and fluorescence contrast. The center frequencies of every NV resonance feature are fit to the appropriate Hamiltonian to extract the desired magnetic field, and also strain, temperature, and electric field for other sensing modalities. In a magnetometry experiment, this analysis yields $\mathbf{B}_0 + \mathbf{B}_s$, from which the unknown magnetic field of the sample

($\mathbf{B}_s$) can be determined when a bias field ($\mathbf{B}_0$) is applied.

The CW-ODMR implies the application of an alternant magnetic field over the NV center with specified frequency f, the time-dependent term is $\hat{H}_{ac}/h = \sqrt{2}\Omega\cos(2\pi ft)\,\hat{S}_x$, where Ω is known as the on-resonance Rabi frequency in MHz, the sum of 3-1, 3-3 with nuclear Zeeman term and the time dependent term allows to simulate the expected resonance which is presented in figure **3-5**

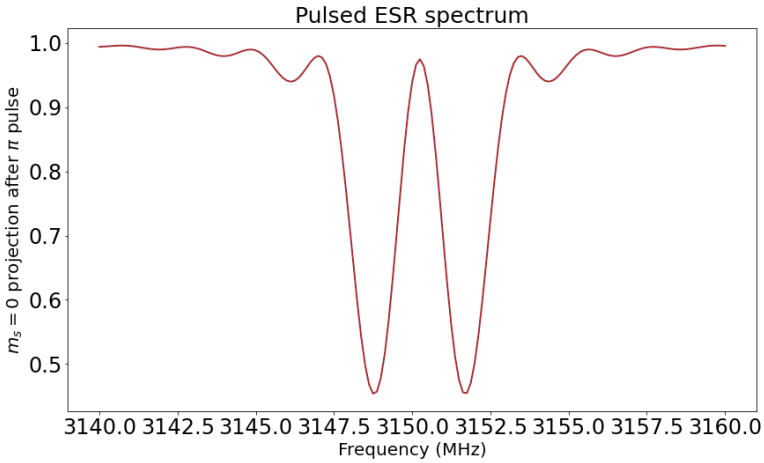

Figure 3-5: Upper resonance spectrum of fluorescence as a function of frequency.

The simplest way to apply a MW field to the NVs is with a piece of wire connected to a coaxial cable. The QDM MW field is ideally uniform across the NV layer field of view, and there are a variety of alternative engineered MW antennas that aim to optimize the MW field homogeneity, efficiency, or bandwidth [94–100]. By the transition selection rules, the transitions between $^3A_2$ sublevels require left-circularly or right-circularly polarized microwaves [101]. One QDM MW antenna option is a pair MW loop as shown in Figure. The striplines are excited in-phase (or 90 degrees out-of-phase) to produce a linearly (or circularly) polarized MW field as needed for a given sensing protocol.

3.2.5 Sensing parameters

Typically NV centers in diamond are used for magnetometry purposes, when an external magnetic field is applied over the system, the hamiltonian have to include an additional term related to zeeman splitting due to the magnetic field B_{NV} in the form of

$$\hat{H}_{mag}/h = \frac{\mu_B}{h}\mathbf{B}_{NV}\cdot\mathbf{g}\cdot\hat{S} = \frac{\mu_B g_e}{h}\left(B_{NVx}\hat{S}_x + B_{NVy}\hat{S}_y + B_{NVz}\hat{S}_z\right) \tag{3-3}$$

Here $\gamma_e = g_e\mu_B/h \approx 28.7$ GHz/T is the NV gyromagnetic ratio, the quantities μ_B and $\mathbf{g}$ are the Bohr magneton and the electronic g-factor tensor, respectively. The Zeeman interaction lifts the

degeracy between the $m_S = \pm 1$ sublevels, and when $|\mathbf{B}_{NV}|$ is along the N-V axis, the sublevel energies split linearly with $|\mathbf{B}_{NV}|$ while m_s sublevel is unaffected. The nuclear Zeeman term is $\gamma_n \mathbf{B}_{NV} \cdot \hat{I}$, with γ_n equals to 3.08 MHz/T and -4.32 MHz/T for nitrogen-14 and nitrogen-15, respectively. This term can be disregarded for magnetic fields below 0.05 T. On this equation $\mathbf{B}_{NV} = \mathbf{B}_0 + \mathbf{B}_s$ where $\mathbf{B}_0$ is the known bias field applied by a permanent magnet or helmholtz coil and $\mathbf{B}_s$ is the unknown samples field to be determined.

In figure **3-6** are shown simulations of the energy levels diagram depending when the magnetic field orientation is in on-axis with NV principal axis (A) or when it is $109.47°$ respect respect NVs principal axis. In this figure can be observed that around 0.1 T there is a groun state level anti crossing in between states with $m_s = 0$ and $m_s = -1$ for the figure **3-6**A and this effect is gone in **3-6**B. Detailed discussion about level anticrossing will be provided in the next sections.

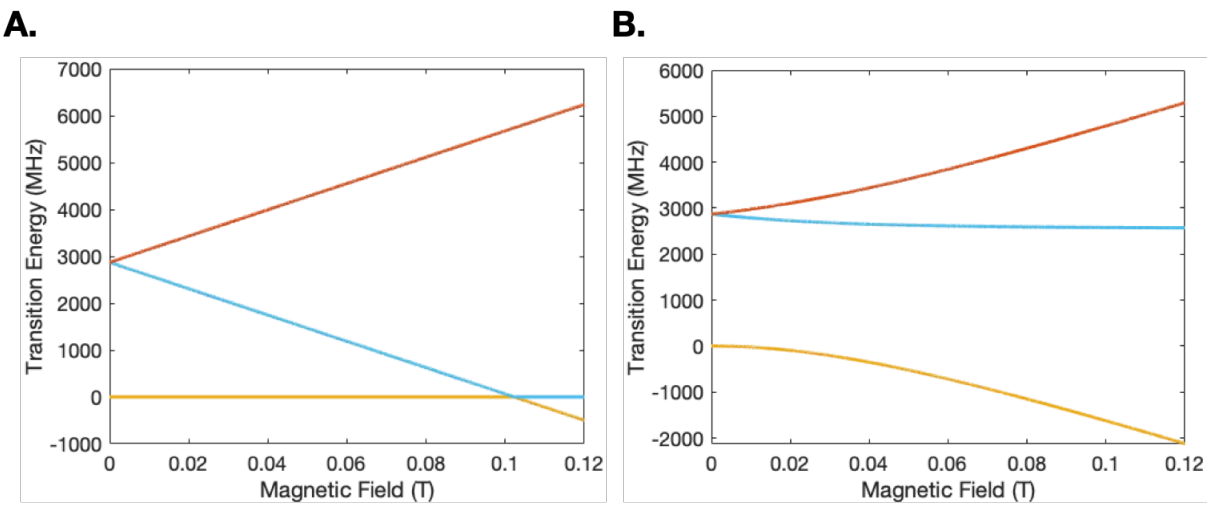

Figure 3-6: Transition energy level for NV center in diamond when fine and hyperfine term are considered, A. corresponds to the case when the field is applied On-axis and B. when the field is applied 109.47° respect NV principal axis.

The unknown orientation and magnitude of the sample magnetic field can be determined by taking advantage of the ODMR resonances from the NV ensemble related to each NV axis possible orientation as shown in figure **3-8**A, where each of the four possible orientation of an NV center in a diamond lattice is shown, in the following **3-8**B, **3-8**C and **3-8**E are shown special cases of the resonances when the magnetic field is zero, showing just the zero-field splitting for a N^{15}; the resonances when a magnetic field is parallel to just one NV axis and forming an angle of 109.47 with the other three axes; and when the magnetic field have equal projections for each NV axis in the lattice. In figure **3-8**E is shown the contribution of each projection over each axis and with this information is possible to determine the magnitude and the orientation of the unknown field.

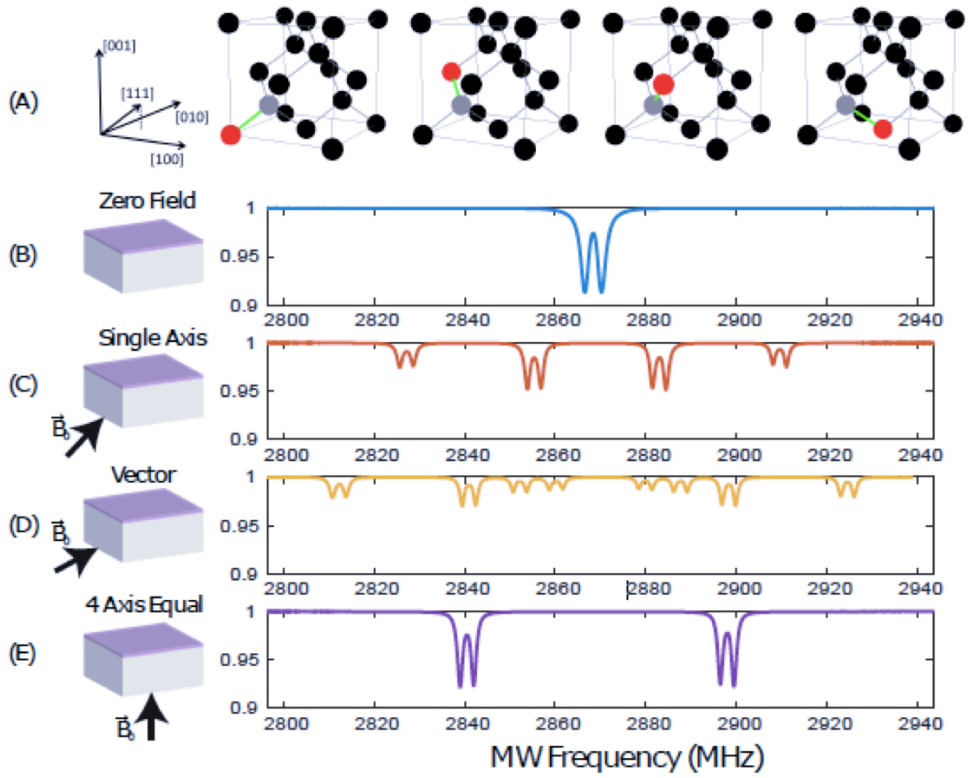

Figure 3-7: NV vector magnetometry using ODMR. (A) Shows NV four possible orientation in a diamond structure. (B) ODMR of an NV center when no magnetic field is applied, the split is due to nitrogen 15 hyperfine. (C) ODMR when the magnetic field goes along one NV axis. (D) ODMR when the magnetic field don't go in a particular orientation. (E) ODMR when the magnetic field is equally projected over the four axis. [103]

The NV centers in diamond also can be used to determine external electric field, temperature distribution, pressure, among others. The external sample electric field $\mathbf{E}_s = (E_{sx}, E_{sy}, E_{sz})$ adds to the local electric field, $\mathbf{E}_{loc} = (E_{loc,x}, E_{loc,y}, E_{loc,z})$, produced by high density of P1 (neutral nitrogen) centers, such that $\mathbf{E}_{tot} = \mathbf{E}_s + \mathbf{E}_{loc}$ contribute to the hamiltonian [110] in Eqn.,

$$\hat{H}_{el}/h = d_{\parallel} E_{tot,z} \hat{S}_z^2 - d_{\perp} E_{tot,x} (\hat{S}_x^2 - \hat{S}_y^2) + d_{\perp} E_{tot,y} (\hat{S}_x^2 + \hat{S}_y^2). \tag{3-4}$$

Here $d_{\parallel} = 3.5 \times 10^{-3}$ Hz/(V/m) and $d_{\perp} = 0.17$Hz/(V/m) are coupling constant related to the NV electric dipole [116, 117].

In addition stress and deformation over the crystal structure can be calculated in the system by considering the following hamiltonian,

$$\hat{H}_{stress}/h = M_z S_z^2 + M_x \left(S_x^2 - S_y^2\right) + M_y \left(S_x S_y + S_y S_x\right) + N_x \left(S_x S_z + S_z S_x\right) + N_x \left(S_y S_z + S_z S_y\right) \tag{3-5}$$

where M_x,M_y,M_z,N_x and N_y are spin-strain coupling parameters [110, 97].

Another case of interest is the distribution of temperature in a sample due that $D(T)$ changes in temperature will change the measurements using NV centers in diamond and it is distinguishable from magnetic or electric fields.

Let's simplify the Hamiltonian doing reasonable approximation of the quantities included in the full hamiltonian of the system that correspond to the sum of all the contribution from equations 3-2, 3-3, 3-4 and 3-5. The transverse magnetic coupling terms ($\propto B_x, B_y$) as well as the spin-strain coupling terms ($\propto N_x, N_y$) are suppressed by D and typically negligible. Furthermore, when an external bias magnetic field is applied with a nonzero projection along the NV axis, shifts in the ground state energy levels related to the transverse electric field components (E_x, E_y) and spin-strain parameters (Mx, M_y) are suppressed proportional to the projection B_z. The transitions between the $|0\rangle$ and $|\pm 1\rangle$ sublevels of this simplified Hamiltonian (additionally dropping the hyperfine and quadrupole structure) become,

$$f_\pm = E_{\pm 1} - E_0 = \left(D(T) + M_z + d_\parallel E_z\right) \pm \gamma B_z \tag{3-6}$$

The $|\pm 1\rangle$ sublevels are split in common ($\propto S_z^2$) from $|0\rangle$ by the zero-field-splitting as well as axial crystal stress and electric fields. Meanwhile, the Zeeman term shifts the $|\pm 1\rangle$ sublevels differentially (in opposite directions). As a consequence, axial stress and electric field induced shifts in the transitions can be deconvolved from magnetic-field-induced shifts by making separate measurements of the $|0\rangle \rightarrow |+1\rangle$ and $|0\rangle \rightarrow |-1\rangle$ transitions.

Finally, the NV ground state spin can be coherently manipulated using MW irradiation resonant with the $f_\pm$ transitions which are non-degenerate when $B_z \neq 0$. Application of resonant or near-resonant MW control fields in combination with the continuous wave or pulsed optical excitation forms the basis of NV-based multi-modal quantum sensing: shifts in the NV ground state spin resonances, $f_\pm$, will result in changes in the detected NV fluorescence. For small changes (relative to the dynamic range of the measurement), the shift in $f_\pm$ with respect to the frequency of the applied MW control field can be linearly mapped to changes in magnetic field, electric field, crystal stress, or temperature. In the following, we will consider transition neglecting the effect of electric field assuming that the sample's electric field, NV ensemble local electric field, and strain variation are negligible.

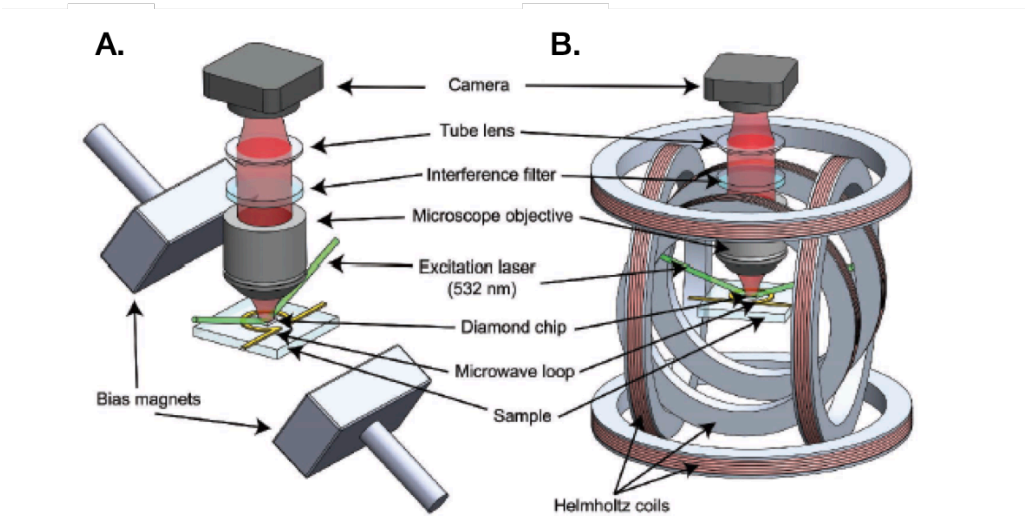

Figure 3-8: Typical quantun magnetic imaging with NV centers in diamond setup. The distinction comes from the use of different sources of bias field, permanent magnets (in A) and Helmholtz coils (in B). [99]

3.2.6 Quantum diamond microscopy setup

The figure shows the basic components used for magnetic imaging using NV centers in diamond, similar setup is used for quantum diamond microscopy, a technique used for mapping a more broad variety of parameters such as electric field, temperature, deformation, among others. From now on QMI and QM will be used to refer to the same setup. The main difference in each configuration is the bias magnetic field source, in Figure A there are permanent magnets, and in Figure B the Helmholtz coil. The components are the aforementioned bias magnets, the optical sensor (in the image camera), the microwave delivery coil, the laser, the optical system, and the doped synthetic diamond. In the following, we will describe some requirements for each component to make a fully functional QDM, however we are not looking to make a exhaustive description of the properties needed for QMI.

The diamond has to be fabricated with control of properties such as NV layer thickness, NV concentration, isotope and impurity concentration, and diamond cut, all of them can be controlled during the fabrication process, the typical methods to produce diamonds are high-pressure and high-temperature (HPHT) growth which is able to produce diamond with nitrogen density of 100 ppm, and the second technique is chemical vapor deposition, which grow the diamond substrate layer by layer [118, 119, 120]. In the other hand, NV layer thickness is optical when the it has size comparable to the magnetic source sedation from the sample, usual thickness corresponds to dimensions of 10 nm to 100 nm. The NV density should be tuned to achieve the desired magnetic field sensitivity, although high NV density yields more fluorescence intensity

and good photon shot noise, a high senility may contribute to inhomogeneity due to impurities and isotopes, which broadening ODMR resonance and spoils magnetic field sensitivity, so NV density should be chosen to get the better trade-off [91, 121, 122, 123]. Finally, the diamond cuts typically used correspond to [100] or [110] planes

The diamond should be illuminated typically by of 532 nm solid-state laser, increasing the illumination intensity improves the NV fluorescence intensity, the photon shot noise, and sometime the ODMR line shape. The red light emitted by the diamond and the green light that hit the diamond should be collected and directed, respectively, with optics, usually the configuration depends on the needs of the setup, but typically the optical photon collection efficiency requires to be optimized by reaching the largest achievable numerical aperture (NA) from an objective and several optical lenses are required to make telescope system to increase the magnification and the illuminated area, a correct disposition of objectives and optical lenses are required to optimize the mentioned parameters[96].

The emitted light should be collected and directed to an optical sensor, i.e. a camera or photodiode, camera selection for a targeted application requires consideration of the expected photon collection rate from the NV layer, camera read-noise and dark-current noise, well depth, global/rolling shutter capability, software and external triggering, frame rate, data transfer rate, pixel size, and quantum efficiency [94]. For experiments with a high photon count rate, the camera must handle enough photoelectrons per second without saturating. Here, the pixel well depth, number of pixels, quantum efficiency, and frame rate are the important quantities to consider, because they determine the maximum photon count rate for fluorescence detection. The camera frame rate can limit the experimentally-realizable temporal resolution. Increasing the camera frame rate is possible by using only a fraction of the sensor. However, the trade-off between frame rate and number of pixels is generally not favorable with regards to maximizing total photoelectrons/s. Alternatively, if the photon count rate is low, parameters like the read noise and dark-current noise should be minimized while the quantum efficiency is maximized.

The QDM bias magnetic field $\mathbf{B}_0$ can be provided by electromagnets (Helmholtz coil sets, solenoids, and C-frame/H-frame electromagnets) or permanent magnets. Electromagnets allow us to select arbitrary $|\mathbf{B}_0|$ up to a few teslas. However, they require a stable current supply, may need water cooling for the magnet, and can add to the sample and system heating. Permanent magnets allow higher $|\mathbf{B}_0|$ in a more compact instrument, though the applied $\mathbf{B}_0$ can drift with temperature. The direction of B0 also factors into the specific QDM application. Alignment of $\mathbf{B}_0$ along the N-V axis ([111] crystallographic direction) allows for interrogating the NVs along this crystallographic direction. This approach allows optimization of the other measurement parameters, e.g., the optical polarization, which maximizes the fluorescence and contrast from the selected NV orientation.

3.2.7 QDM performance

Magnetic field sensitivity

The minimum detectable field difference is defined as the change in magnetic field magnitude, **B** for which the resulting change in a given measurement of the field equals the standard deviation of a series of identical measurements. However, for meaningful determination of sensor performance characterizations of the minimum detectable field must consider the total measurement duration, as well as the total number of NVs that contributed to the measurement. The magnetic field sensitivity scales as the square root of the number of detected photons. The number of photons collected over a unit time from a unit volume of NVs increases proportionally with time and volume. To account for measurement time, sensitivity is represented as $\eta = \delta B\sqrt{(t_{meas})}$ with units of T $\text{Hz}^{-1/2}$, where t_{meas} is the total measurement time. To account for the number of NV spins required to reach a given sensitivity, a sensor volume-normalized sensitivity is defined as $\eta_{vol} = \eta\sqrt{V}$ with units Tμ $\text{m}^{3/2}\text{Hz}^{-1/2}$, where V is volume for a fixed density of NVs [34].

Temporal Resolution and Frequency Bandwidth

For broadband QMI measurements, temporal resolution is defined as the time between subsequent measurements of the sample field. The physical limitation determining the fastest temporal resolution is set by the time it takes for the NVs to react to a change in the sample field. The temporal resolution can never be faster than the inverse of 5 MHz (the maximum optical pumping rate), which is limited by the ^{1}E metastable state lifetime. The same is true for pulsed measurements, since NVs are optically reinitialized to the $m_s = 0$ state. before each measurement. For a measurement with continuous laser illumination and MW field, the QDM temporal resolution is set by the optical pumping rate and the MW Rabi frequency. There is also a practical limit to the temporal resolution, set by signal-to-noise ratio (SNR) tolerance: faster temporal resolution gives worse SNR per measurement. QDM frequency bandwidth is the range of sample frequencies that can be interrogated with the same experimental protocol. A broadband magnetometry experiment has a frequency resolution spanning from static DC fields to $\sim$ 100s of kHz.

Spatial Resolution and Field of View

QDM imaging seeks to resolve magnetic fields with sufficiently high spatial variation and wide-field of view to probe the sample properties of interest; and to successfully invert the magnetic field measurements to generate a map of closely-separated magnetic sources. Both goals have fundamental and sensor-specific limitations. It is ideal to operate at the limit of magnetic field inversion and not to be limited by the sensor properties such as resolution and field of view.

1. NV-sample standoff distance. As the standoff distance Δz increases, the 2D magnetic map is convolved with a Lorentzian of width Δz, reducing the ability to resolve closely

separated magnetic sources. Reducing the standoff distance improves the field strength and often the spatial resolution.

2. NV layer thickness. A sample with an NV layer much larger than the sample standoff distance will degrade the spatial resolution. An infinitesimally thin NV layer will ensure the imaging resolution is not limited by the diamond properties. However, thicker NV layers can increase sensitivity through increasing the amount of photons produced for a given optical excitation intensity. Therefore, the optimal NV layer needs to be tuned to balance needed imaging resolution with measurement sensitivity.

3. Optical diffraction limit. Set by the numerical aperture (NA) of the microscope objective ($\lambda/(2NA)$) for a typical fluorescence wavelength of $\lambda \approx 700$ nm. This assumes that the camera pixel size is small compared to the diffraction-limited spot size in the image plane. The spherical aberration from the diamond chip or other optics can also degrade the resolution so the optical diffraction limit would need to be modified.

In general, QDM magnetic field imaging is best used for applications that need both high spatial resolution and wide-field of view, and can also afford small NV-sample separation. The intuitive rule-of-thumb is to have NV layer thickness, standoff distance, and sample thickness of comparable sizes.

3.3 Experimental Methods

Sample preparation

Diamond cut is [100] created using CVD, implemented with nitrogen with NVs at a depth of 20 nm in average and density in the range of $10^{12} - 10^{13}$ cm^{-2}. The diamond have fabricated markers on the surface of the NVs side via litography and electron beam evaporation to facilitate flake identification.

In figure **3-9**A is shown the unit cell of Fe_5GeTe_2 (FGT) and co-doped Fe_5GeTe_2 (CFGT) single crystals were grown using iodine as a mineralizer/transport agent together with elemental Fe (granules), Ge pieces, and Te shot in sealed, evacuated silica ampoules. Single crystals of the reported phase were obtained from growths with nominal compositions of $Fe_{4.7}GeTe_2$ Polycrystalline $Fe_{5-x}GeTe_2$ was obtained by reacting the elements in a sealed silica ampoule at 973-1023 K followed by quenched from the growth temperature and washed with ethanol and acetone. For these samples, Fe powder, Ge powder, and Te shot were ground together in a helium glove box and the quartz ampoule was sealed after purging with argon. Samples that were allowed to cool to 10 K or less in a magnetometer in the furnace were characterized by X-ray diffraction patterns. The Fe content has not been controlled during these growths, which are done in the presence of iodine, and the average composition is expected to be near $Fe_{4.7}GeTe_2$. The

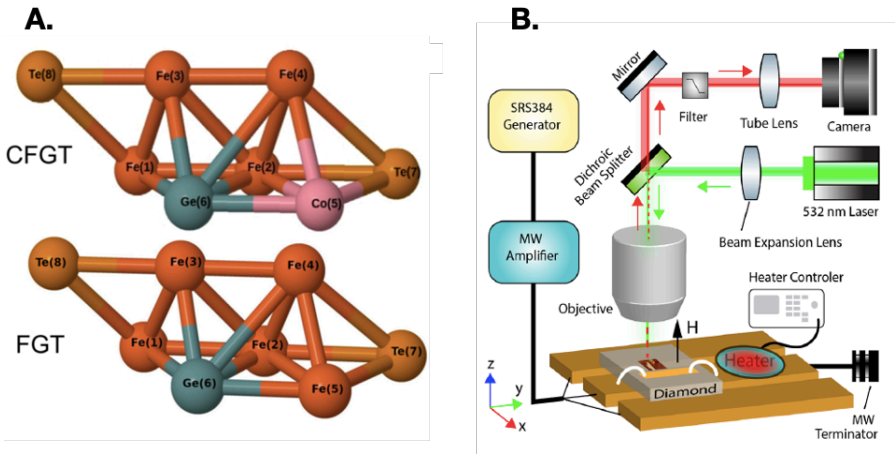

Figure 3-9: A. Crystallographic structure of Fe_5GeTe_2 (FGT) and Co-substited Fe_5GeTe_2 (CFGT). B. NV-QMI setup implemented. Adapted from [124]

Fe_5GeTe_2 crystals are initially stored in a vacuum desiccator to avoid sample degradation. We exfoliate flakes on the diamond surface with NVs. Exfoliation was performed with a standard medium-tack Blue Plastic Film tape (Semiconductor Equipment Corporation P/N 18074). Exfoliation was done quickly in the air, and then the sample was immediately transferred into an electron-beam evaporation chamber for deposition of a 5 nm Pt layer as a protection layer to prevent degradation. In this work, we have investigated both flakes protected with the Pt layer and flakes without a protective layer. In previous literature is based this procedure [125, 126].

Cobalt-containing crystals were grown using the same iodine-assisted approach as utilized as previously described, using initial compositions of $Fe_{5-y}Co_yGeTe_2$. The raw elements were sealed in evacuated silica ampoules and heated to 750 $°C$ at 120$°C$/h, followed by an isothermal step for 1– 2 weeks at 750 $°C$. The ampoules were quenched into ice water and iodine was washed from the surfaces of crystals with solvents (ethanol and/or isopropanol with an acetone rinse). The exfoliation process was carried out as described previously.

The initial cooling and then heating procedure in FGT samples exhibit a first-order magnetostructural transition near 100K that increases the bulk Curie temperature from ≈ 270 to 310K. In addition, the magnetic phase of Co-dope FGT samples exhibit different type of magnetic phases depending on the percentage of cobalt in the lattice, and the introduction of it enhance the curie temperature up to 330 K when the percentage of cobalt is up to 30%, beyond it behaves as an antiferromagnet[127, 126]. In this work, the doping is 28%, for the bulk crystal characterization shows a curie temperature of about 328 K for and an easy-plane anisotropy, with an effective anisotropic field of $H_a = -5.1$ kOe.

Experimental procedure

The schematic of QMI is described in **3-9**B. We use a 532 nm laser (Coherent Verdi 2 G) in the QMI system. A Kohler-illumination system, consisting of a beam expansion lens and an objective (Olympus ULWD MSPlan80 0.75 NA), expands the laser beam to illuminate an area of about 40 $\times$ 40 μm^2 on the sample. NV photoluminescence (PL) is collected with the same objective. The collected light passes through a 552 nm edge dichroic (Semrock LM01-552-25), after which it is separated from the excitation, passes through another 570 nm long-pass filter to further reduce light not in the PL wavelength range, and is imaged via a tube lens (focal length f = 200 mm) onto a camera (Basler acA1920- 155μm). Each pixel corresponds to 133 nm on the sample (265 nm if an additional 2 $\times$ 2 binning is applied). The estimated number of NVs that contribute to the signal of a pixel is $\leq$10. A SRS384 signal generator supplies microwave (MW) to an amplifier to produce MW with power of 45 dBm. The MW is delivered into the signal line of a co-planner waveguide on a printed circuit board (PCB), which produces an in-plane MW magnetic field for driving NV spin transition. In our experiment, the diamond surface with exfoliated Fe_5GeTe_2 flakes and NVs may be either facing up or down.

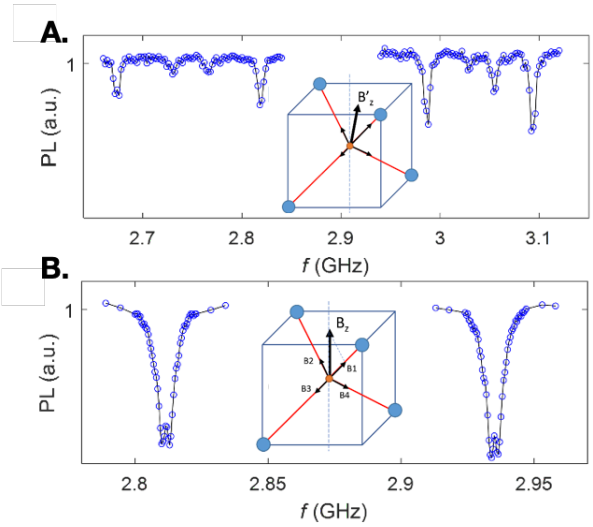

Figure 3-10: ODMR spectrum for different bias field direction. A. B_{NV} corresponds to split all eight ODMR resonances. B. B_z corresponds to getting only two ODMR resonances by projecting the field equally to each crystallographic orientation. Adapted from [124, 128]

A permanent magnet, movable via motorized stages, supplies a bias field for splitting the ODMR resonances. In principle, there can be up to four pairs of ODMR resonances, each corresponding to $m_s = 0 \leftrightarrow \pm 1$ transitions of NVs aligned with one of the four-diamond crystalline axes; the direction of the nitrogen-vacancy bond provides the quantization axis for the corresponding NV, and it may point along one of the four possible crystallographic directions. We employ two

configurations of bias field B_0.

First, a bias field can be applied in a direction to split all four ODMR resonances. In this configuration, we sense B_{NV}, the projection of the magnetic field along an NV quantization axis of our choice; B_{NV} has a contribution from both the out-of-plane and in-plane fields. The projection of the total magnetic field (the sum of the sample stray field and an applied bias field) on each axis, B_{NV}, contributes to the shift of ODMR resonance. Off-axis field also contributes to the shift of ODMR resonance; however, the leading order off-axis contribution is common-mode motion between the upper and the lower transitions, and in our analysis procedure, we only look at the differential shift, hence we are not sensitive to off-axis field. When the bias field is fixed, the shifts in ODMR resonance reveal the amplitude of the sample field projected along the crystallographic direction. In general, an ODMR spectrum includes four pairs of transitions due to the Zeeman splitting as shown in figure **3-10**A.

In a second configuration, we align B_0 along the z direction (normal to the diamond surface), which allows us to sense B_z, the projection of the field along the z direction. All measurements are performed in the atmosphere. Only one pair of transitions is observed as shown in figure **3-10**B because the field projection on each crystallographic direction is equal. As a matter of fact, applying B_0 in the z direction results in an enhanced contrast in the ODMR spectrum since it is the sum of the contribution from all four NV axis, as long as the bias is not large ($B \leq 100$ G) and hence the effect of the off-axis field on photoluminescence contrast is not strong. The enhanced contrast in this configuration is confirmed by the comparison of resonance contrast between figure **3-10**A, and B where 4 transitions on each side are overlapped. However, it might also broaden the linewidth due to the frequency shift of resonances induced by even a slight misalignment between B_0 and z direction. The broadened linewidth as a result reduces the sensing sensitivity. Therefore, good alignment is crucial in B_z configuration.

The frequency splitting between lower and upper resonance transitions can be written by $\Delta f = 2\gamma_{NV}(B_{0,NV} + B_{NV})$ where $\gamma_{NV} = 28.03$ GHz/T is the NV gyromagnetic ratio, $B_{0,NV}$, and B_{NV} are the bias field and sample stray field projected on the corresponding NV axis. Thus, the stray field is calculated by $B_{NV} = (\Delta f/2\gamma_{NV}) - B_{0,NV}$. While in B_z configuration, the stray field B_z is calculated by the formula $B_z = \sqrt{3}(\Delta f/2\gamma_{NV}) - B_0$ according to the geometric relationship between the bias field and NV axis.

Measurements and analysis protocol

By sweeping the MW frequency, the camera records an ODMR spectrum for each pixel. Thus, mapping of the sample field is realized by extracting resonances from each pixel, acquiring an image $I(x, y, f)$. We scan the microwave frequency between $2.65 \sim 2.70$ GHz and $3.07 \sim 3.11$

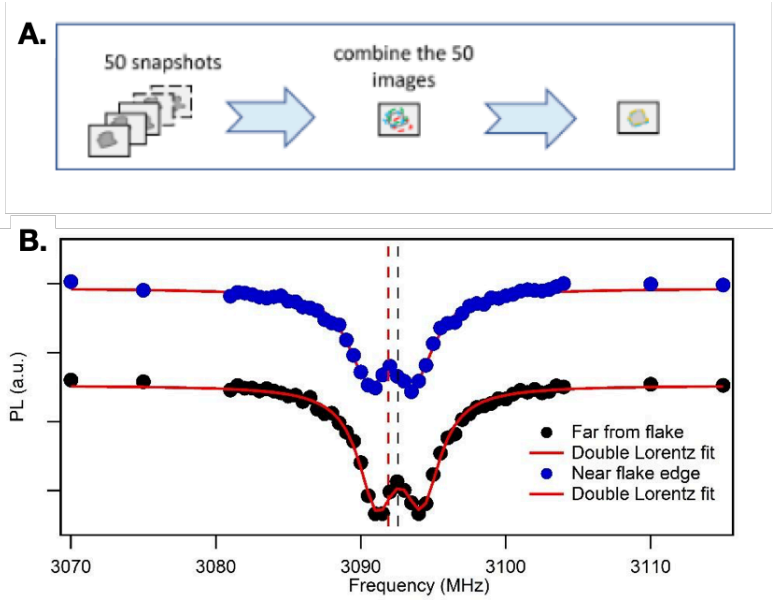

Figure 3-11: A. Step by step process for imaging sum up using flakes edges in each image. B. ODMR far and near flake.

GHz to obtain the branch of the two transitions with the largest frequency span. We repeat PL imaging of the sample N times ($N > 50$) and the recorded images, $I_i(x, y, f)$, are added up to reduce the noise in measured ODMR spectrums. However, misalignment might occur among recorded images due to the drift of sample position in the x-y plane. As described in figure **3-11**A, the displaced images could be corrected by aligning the contours of the imaged flakes. This is a necessary step before we sum up the images. The summed image will be followed with pixel binning to further improve the signal-to-noise ratio (SNR) in the image. We analyze each pixel in the binned image by fitting the ODMR spectrum with a double-Lorentz function. The lineshape is a result of hyperfine splitting due to ^{15}N nuclear spins. The fitted values of resonance frequency are used to calculate the stray field at the corresponding pixel, which allows us to map the entire imaged region depending on the configuration of the bias field employed. It is noted that in the final mapping result, we discard the contribution from the external magnetic field B0 by subtracting the average of the image region without flakes.

In **3-11**B, we show the two ODMR spectrums which are measured from a pixel near to the flake edge and one pixel far away from the flake. Here, we only show the resonance of the upper transition ($m_s = 0 \leftrightarrow +1$). The resonant peaks are fitted using a double-Lorentz formula and the center of the peak is used to determine Δf. It is observed that the ODMR peak position shifts to a lower frequency in the presence of a magnetic material, which indicates the generated negative stray field from a flake.

3.4 Results and discussion

The figure **3-12**a,**3-12**b,**3-12**c, and d shows the QMI method applied to detect the magnetic field in Z generated by flakes of different thickness of Fe_5GeTe_2 at ambient conditions, i.e. at room temperature and in the atmosphere. The thickness of each flake was determined using an atomic force microscope and the optical image as well as the measurement value are shown in figures **3-12**g, **3-12**h, and **3-12**f. Now first we will show that the origin of the stray field comes from the ferromagnetism nature of the flakes.

To probe the ferromagnetic behavior of the flakes we follow the next procedure, we magnetize the flakes before imaging them, to do so, we use one side (pole 1) of a cylindrical permanent magnet with a magnetic field of about 0.6 T. The way we determine the bias magnetic field in z consists of using the ODMR spectrum of the regions where the flakes are not located, in these regions the ODMR is due just to the bias field only. In this configuration, the magnet provides a bias field $B_0 = 40$ G in the z-direction, and it is useful to split the lower and upper transitions in the ODMR spectrum and hence identify the sign of the stray field. The analyzed δB_z fields of a 100 nm thick flake magnetized by pole 1 are plotted in Fig. a. Subsequently, we magnetize the flakes again but with the opposite pole (pole 2) of the permanent magnet. We then perform measurement in a similar bias field $B_0 = 30$ G. The field mapping result is shown in Fig. 2b. We note that measurements occurred at two different bias fields because the diamond position slightly changes with respect to the permanent magnet underneath the PCB board when each time the diamond is mounted after the magnetizing procedure. The contribution from the bias field to the map has been removed in the figure.

Now, before we move forward, let's consider the numerically simulated field in the z-direction generated from a small square magnet with a single domain in the figure **3-13**. In **3-13**A shows the B_z map with the centrosymmetric pattern when the magnetization is out of the plane, the major contrast is observed at the edges of the square and in the inner has a weak intensity but still significant. When the magnetization goes along x direction, the simulation shows that the largest intensity of the field is at the two edges with the opposite sign, and in the inner part is almost zero as shown in figure **3-13**B. Line cuts of the field generated by each configuration at $y = 0$ are shown in figures **3-13**C and **3-13**D, where can be highlighted the change of sign in Bz field generated when the magnetization is out-of-plane in **3-13**C. In general, flakes could have domains or magnetic textures, which will produce more complex patterns, hence the experimentally imaged magnetic field will not necessarily have all the features exhibited by a single domain, however, in general one could anticipate that the δB_z field will be along the boundary and more generally across the flakes, if magnetization is present.

Indeed, in figures **3-12**(a) to **3-12**(e), a stray field across the flakes is observed with similar features to the mentioned above for the magnetized square, however, the question then is whether

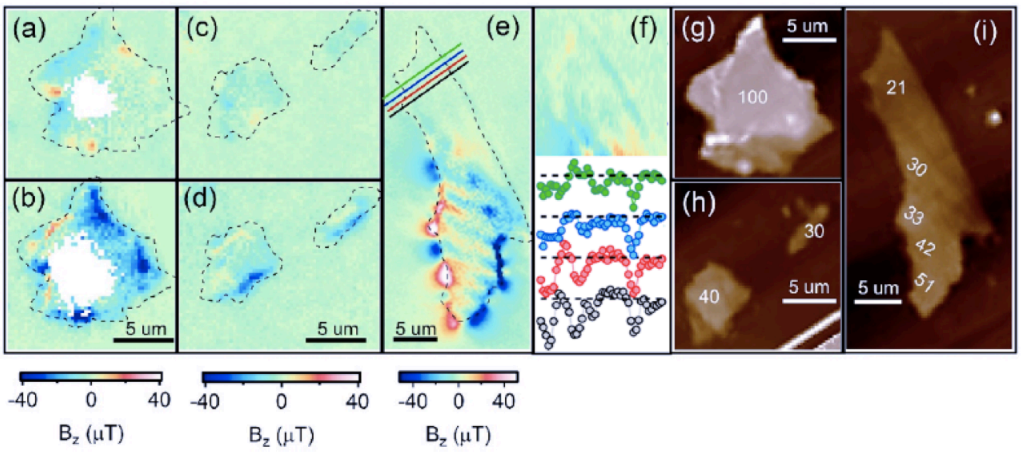

Figure 3-12: Ferromagnetism in exfoliated thin flakes of Fe_5GeTe_2. Measurements have been performed when a magnetic bias field in z, B_z, is present and δB_z is mapped in the figures. The flakes are magnetized by the two poles of a permanent magnet. Pole 1 is used for figure (a) and (c) , and pole 2 is used for figure (b) and (d), figures (a) and (b) shows the thickest flakes (around 10 nm). In figure (e) displays the Bz field mapping of the thinnest flake of 21 nm. (f) Top: zoomed-in view of the upper part of the flake in Figure (e). Bottom: Stray field variation along the four linecuts marked in (e). Each curve has a vertical offset for clarity of display. Horizontal black dashed lines indicate zero ΔBz value for each of the curves. Curves are correlated to the line cuts in (e) by different colors. In each curve, the left peak and right dip clearly indicate the boundary of the thinnest part. In particular, a sharp dip manifests along the right boundary, which is marked with vertical orange dashed line. (g)-(i) AFM images of the 4 measured flakes where the thicknesses of flakes are labeled by the numbers in the unit of nanometers. The outlines of the flakes in panels (a) to (e) have been depicted with black dash lines.

the field from the flakes comes from a ferromagnetic or paramagnetic phase. If the flakes are paramagnetic, then the local magnetic moment that compounds the total magnetization of the flake will orient in the same direction as the applied magnetic field and its intensity will be proportional to the applied field, so, it is expected that in a paramagnetic sample when pole 1 (bias field of 40 G) faces the sample the field generated by the flakes should be more intense and with an opposite sign than the field generated by the flakes when the pole 2 (bias field of 30 G) is applied. Instead, we observe the opposite, when pole 2 is facing the flakes, the intensity of the field is way higher than the field produced by the sample when pole 1 faces the sample, so clearly, the measured stray fields show a significant difference in strength when we magnetize the flake in opposite directions. This result is consistent with the presence of ferromagnetically ordered magnetization: when the magnetization is polarized along the opposite directions, one polarization will show a stronger magnetization (and hence a stray field) in the same or even

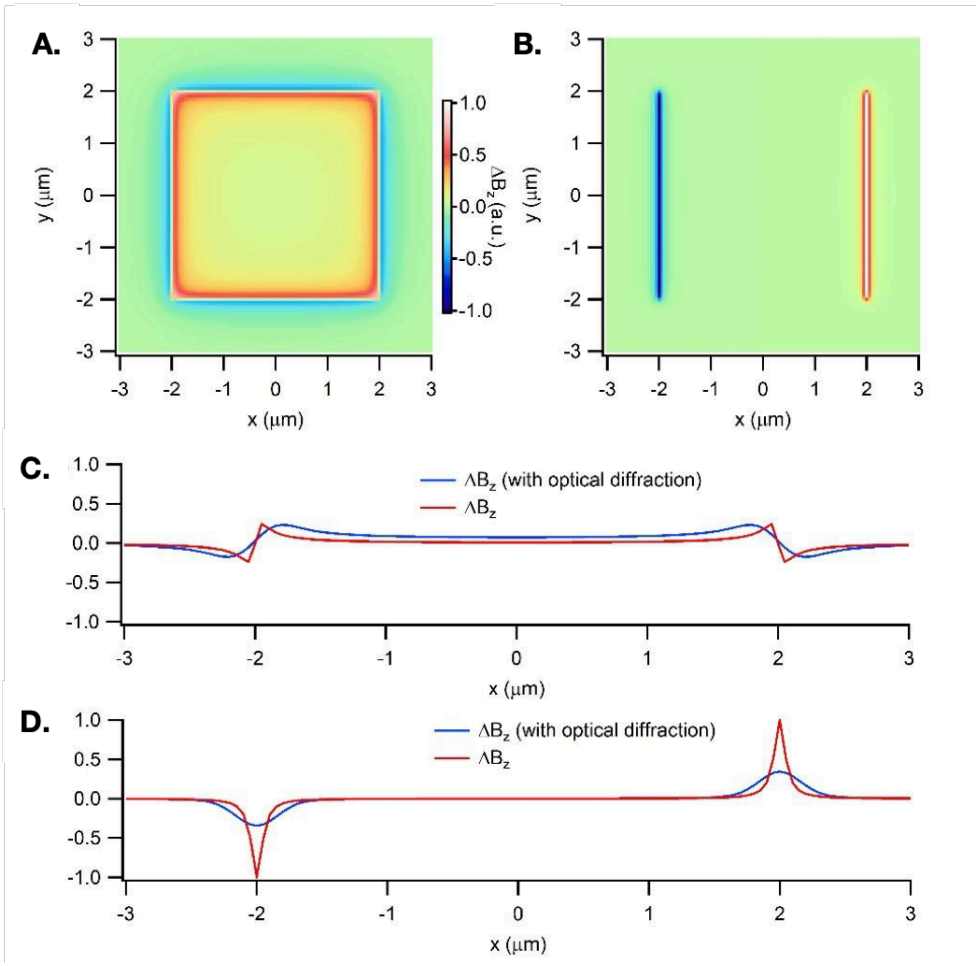

Figure 3-13: A. Magnetic field generated by a out-of-plane magnetization in a square sample. B. Magnetic field generated by a in-plane magnetization in a square sample. C. Linecut at y=0 for the figure A. D. Linecut at y=0 for the figure D.

a smaller bias field. This analysis does not require the flake to have a single magnetic domain, as we have access to local stray fields. Similar observations are found in the other two smaller flakes with thicknesses of 40 nm and 30 nm as shown in figure **3-12**(c) and (d). Therefore, we conclude the stray field observed is generated by ferromagnetism in the flakes.

Using the map of the ΔB_z on the surface of the sample provides insights into the magnetic anisotropy of the flake. As is shown in figure b, we observe the field has mostly the same sign along the edge as well as in the inner part of the flake. The pixel data with low signal-noise-to-ratio, e.g., when the error of $\delta(\Delta Bz)$ larger than 300μT, has been removed, this is because the thick flakes attenuate light and reduce the number of collected photons. Additional features in the map are likely due to domain or magnetic textures. The observed topology looks similar to the expected distribution induced by a perpendicular magnetization, additionally is worth high-

lighting that the feature doesn't correspond to the ones generated by an in-plane field, this is a pattern with field localized to the boundary and vanishingly small in the inner part of the flake.

Figures **3-12**(c) and **3-12**(d) are thinner flakes, hence the SNR is higher in the flakes center in both, so the field is generally visualized in the entire flakes. Lastly, we note the contrast between Figures **3-12**(a) and **3-12**(b), as well as **3-12**(c) and **3-12**(d), indicates the change in magnetization induced by a perpendicular magnetizing field persists after the magnetizing field has been removed. Aspects of these results point to easy-axis anisotropy near T_C, though further investigation is required to draw certain conclusions. For instance, the stray field appears to remain across a crystal, though the existence of domains could lead to apparent sign inversions within a given flake that may also give the appearance of in-plane anisotropy. Future measurements at higher and variable bias fields would provide even more insight into the magnetism in these and similar materials in this thin flake form, and in particular allow more definitive conclusions about anisotropy.

Lastly, we explore what is the thinnest flake we have observed that exhibits room-temperature ferromagnetism. To do so, we show the stray field map of a 21 nm thick flake in figure **3-12**(e) and in figure **3-12**(f) there is a zoom-in view of the upper part where the thinner part of the flake is shown. We trace four linecuts to study the field through the flake, which clearly displays a stray field near the boundary, this demonstrates the ability of our wide-field NV magnetometer to characterize the stray field induced by very thin flakes. Hence, we demonstrate Fe_5GeTe_2, when protected with a thin Pt layer, exhibits ferromagnetism in flakes as thin as 21 nm, corresponding to 7 unit cells. The thicknesses of all those flakes are measured by atomic force microscopy (AFM) as shown in figure **3-12**(g) to (i). We note that in figure **3-12**(i) multiple terraces are present in the bottom half of the flake, as revealed by AFM, and may be responsible for the complex stray field pattern in the bottom half of figure **3-12**(i).

At last, we demonstrate the utility of our QMI technique for rapid screening of magnetism in exfoliated flakes. Multiple Fe_5GeTe_2 flakes without Pt protection layer are imaged at room temperature and the stray field map is shown in figure **3-14**(a). We note that in this measurement, B_{NV} was imaged, hence the stray field pattern looks different from those in figure **??**. As mentioned above near the center of the flakes, the SNR of stray field measurement is low so here the stray field values are not displayed for these pixel points. The AFM image of the corresponding flakes are shown in figure **3-14**(b). We have properly labeled the flakes or flake clusters in both panels. It is seen that some small flakes are visible in AFM picture (for example, flakes circled by red box A and B) but do not generate stray field. This may be attributed to the fact that those flakes are too small or too thin and hence have completely degraded in the absence of protective layer. However, even some larger flakes (for example, the flakes around the cluster number 2) also do not generate stray fields, which may also indicate complete degradation. Among the flakes that generate stray fields, we find the thinnest flake is 40 nm thick (< 20 unit

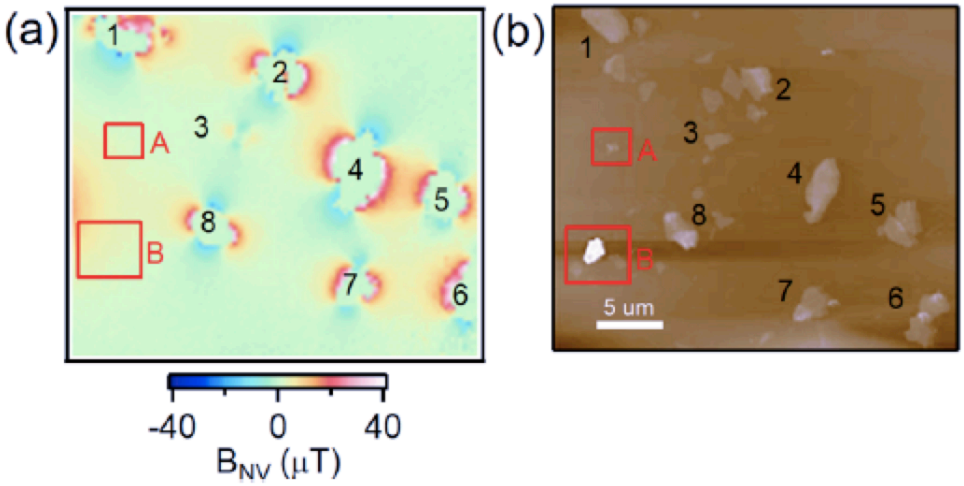

Figure 3-14: The B_{NV} stray field map of Fe_5GeTe_2 flakes without Pt protection layer. Stray field in areas where SNR is low is not shown. (b) The AFM image of the flakes in (a). The flake or the flakes cluster are labeled by numbers and the measured flakes thicknesses are 1(45 80 nm), 2(35 100 nm), 3(40 65 nm), 4(110 nm), 5(75 150 nm), 6(85 nm), 7(60 nm), 8(100 nm).

cells). This result shows our image tool can measure the magnetism of unprotected Fe_5GeTe_2 flake also down to very thin layers. It also provides an option to investigate the degradation of the magnetic flakes in an ambient condition by imaging the sample field changing with time. Lastly, this work demonstrates the utility of QMI for rapid, parallel characterization of the thin flakes of other potential 2D magnets near room temperature, providing an enabling tool that will aid the effort in discovering additional 2D magnets that are useful for applications.

To help inform what kind of pattern of stray-field distribution one anticipates to observe, we show simulated $B_z(x, y)$ generated by a square magnetic structure with a uniform out-of-plane (**3-15**2(a)) and in-plane 2D magnetization (**3-15** (b)). The former generates a $B_z(x, y)$ that switches sign at the boundary, where the latter generates a dipole-like pattern that is antisymmetric along the magnetization direction. In figures **3-15**(c) to **3-15**(h), we show images of experimentally measured stray field distribution of several flakes. The thickness of flakes was measured with an atomic force microscope (AFM) and is 15.7(3) nm (16 layers) for figures **3-15**(c), **3-15**(f), 28.6(3) (29 layers) for figures **3-15**(d), **3-15**(g), and 25.6(2) nm (26 layers) for figures **3-15**(e), **3-15**(h), and. Thickness is 56.5(6) nm (58 layers) for figure **3-15**(i). In Figures **3-15**(c) to **3-15**(e), we show $B_z(x, y)$ with an out-of-plane bias field $B_0 \sim 30$ mT. In each case, we observed $B_z(x, y)$ maps that have a similar topology to the one shown in Figure **3-15**(a), indicating that magnetization is directed out-of-plane. We then lowered the bias field to $B_0 \sim 3$ mT. The corresponding $B_z(x, y)$ maps, shown in figures **3-15**(f) to **3-15**(h), undergo a dramatic change in topology and reveal a texture of the change in the distribution of the stray field and hence the underlying magnetic domains. The stray field texture contains multiple dipole-like features, consistent with the ex-

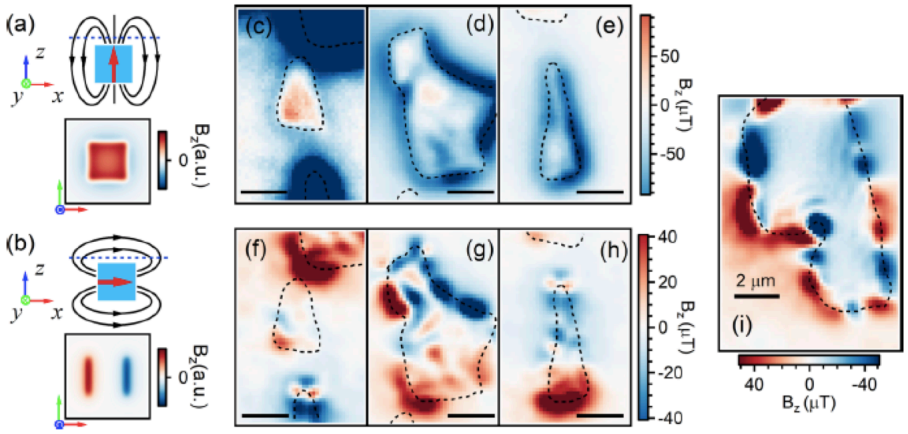

Figure 3-15: Quantum magnetic imaging of CFGT flakes. a) and b): Simulated distribution of vertical stray field B_z for uniform a) out-of-plane (pointing along z) and b) in-plane (pointing along x) magnetization. Here, one assumes a 2D 1 μm $\times$ 1 μm square of magnetization, and stray field is simulated at a stand-off distance d=100 nm. Images are convolved with a point spread function corresponding to 600 nm optical resolution of the experimental setup. c)-e) Experimental stray field of CFGT flakes at room temperature with an applied vertical bias field (along z-direction) $\sim$30 mT. These images have a similar topology to a), demonstrating that magnetization is aligned along the vertical direction. f)-h): Measurement of the same flakes corresponding to c-e respectively, but with a smaller vertical bias field $\sim$3 mT. Here, we see stray field texture develops that reveals underlying domains. Magnetizations that get oriented along the bias field at high field and forms domains at low field demonstrate that these flakes have ferromagnetic order. The thickness of flakes are 15.7(3) nm (16 layers) for c, f, 25.6(2) nm (26 layers) for d, g, and 28.6(3) nm (29 layers) for e, h. i) Measurement of a 56.5(6) nm thick (58 layers) flake under the same condition as f-h. All experimental images are shown to the same scale; a 2 μm scale bar is shown in (i)

pectation of in-plane magnetized domains inferred from bulk magnetization measurement that shows zero remanence and easy-plane anisotropy. The change in stray field topology as the external field was lowered and the revelation of domains confirmed the ferromagnetic ordering of flakes; if the flakes were paramagnetic, the stray field would merely change in amplitude but not topology. In figure **3-15**(i), we show the stray field of another flake at a bias field $\sim$3 mT, which also displays stray field texture, demonstrating that room-temperature ferromagnetism is ubiquitous among CFGT flakes.

3.5 Summary

- We have developed a NV-QMI modality with reliable capabilities to explore thin and ultrathin flakes of Van der Waals Material.
- We have probed ferromagnetism in flakes of FGT and Co-doped FGT at room temperature. In particular have shown magnetism in flakes with thickness as little as 7 unit cells.
- Our method allows us to screen several flakes at once and explore the thickness effects in the intensity of the magnetic field generated by each flake. In addition our method allows us to study in-plane magnetization as well as out-plane magnetization over the samples studied.
- Finally, our numerical simulation to predict ODMR behavior and to simulate the magnetic field generated by samples was in good agreement with our experimental finding.

4 All-Optical and micro-wave free Low Field Magnetometer based on NV center in diamond

4.1 Introduction

As shown in previous chapter the NV center in diamond magnetometry is a modality that depends directly on the use of microwave fields to detect external sensing parameters. However, this technique could be problematic for studying systems where both external magnetic field and microwave might disturb the target system. Some examples correspond to the detection of MWs generated by eddy currents in conductive materials in the context of magnetic induction tomography[129, 130], high-Tc superconductors (Tc stands for the superconducting transition temperature) [131] and also has remained an outstanding challenge to extend the vector capability to cryogenic temperatures (less than 4 K) due to difficulties of thermal management. The heat from the applied microwaves is unavoidable and causes temperature variations, restricting the sensors for numerous innovative applications, such as mapping the magnetization of individual atomic layers of van der Waals materials.

There have been several demonstrations of MW-free, and all-optical, diamond-based magnetic sensors, initially implemented with single NV centers attached to scanning atomic force microscopes, and more recently with ensembles of NV centers[132, 102, 133, 134]. These MW-free magnetometric protocols have been realized by exploiting either the properties of the NV centers photoluminescence (PL), shown in figure **4-1** [135], or their decoherence properties under the influence of external MWs, some experimental realizations have demonstrated competitive sensitivities around the few nT/$\sqrt{Hz}$, taking advantage of features such as GSLAC [102, 132, 136]. Spin cross-relaxation (CR) at low field due to NV-NV interaction has also been observed and could be deployed for higher sensitivity microwave-free magnetometry. The CR contrast was indeed shown to be much larger in this zero-field limit but all the relaxation mechanisms have not been identified there.

Understanding the impact of CR in all-optical microwave-free modality is essential to improve sensitivity, to do so a simulation model is required to get insights about the parameters that

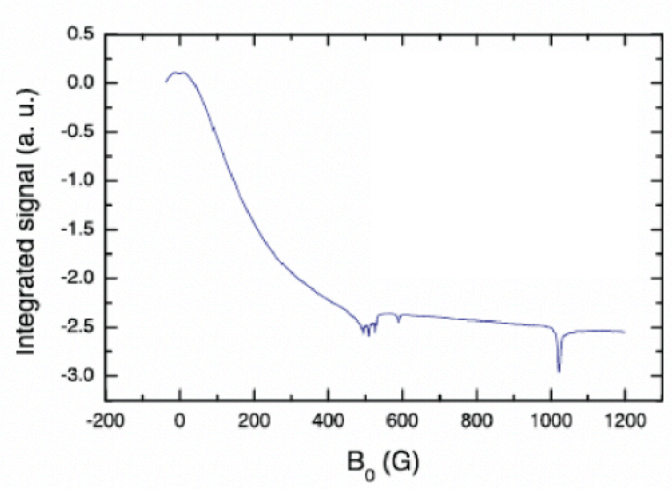

Figure 4-1: PL spectrum as a function of an on-axis magnetic field for a nitrogen vacancy center

could affect the CR features in the photoluminescence behavior in NV centers in diamond [137, 138, 133]. A semi-classical model that considers the main 7-level states from the NV center system, i.e. ground state, excited state, and intersystem crossing, has been developed for such purposes, however, the existing model offers light on the behavior around GSLAC mainly and doesn't explore the effects of CR at low field, in addition, the method cannot be extensible to systems that include nuclear spin, or other defect centers, due a lack of mathematical basis to introduce the additional degree of freedom in a phenomenological manner[139]. In addition, several models that are based on the Lindblad equation are computational expensive and have not been extended for cases when interaction in between defect centers should be considered [140, 141].

On the other hand, further experimental research for an all-optical low-field magnetometer based on NV is still required. Recent reports explore such modality, however, the absence of a full theoretical model that accounts for their findings is still missing for properly grounding their insights. In our work, we develop a theoretical model based on previous literature to understand the cross-relaxation nature and build our own all-optical magnetometer based on the nitrogen-vacancy center, to verify our findings from the simulation model and get further understanding of experimental parameters that play a role in the study of this modality. This chapter, initially will introduce important Hamiltonian considerations about the system. After the theoretical model proposed is shown, as well as relevant numerical simulations. Then experimental results contrasted with simulations are discussed. Finally, a summary of our findings are presented.

4.2 Theoretical Methods

4.2.1 Hamiltonian considerations

In the previous chapter, the ground state Hamiltonian for NV centers in diamonds was broadly discussed considering several fields and effects over the system. In the following, we will consider features such as fine, quadrupolar, and hyperfine terms as well as the Zeeman term, when the magnetic field is applied, as follows,

$$\frac{\hat{H}_{gs}}{\hbar} = \hat{S} \cdot \mathbf{D} \cdot \hat{S} + \hat{S} \cdot \mathbf{A} \cdot \hat{I} + \hat{I} \cdot \mathbf{Q} \cdot \hat{I} + \hat{I} \cdot \mathbf{Q} \cdot \hat{I} + \frac{\mu_B}{h} \mathbf{B} \cdot \mathbf{g} \cdot \hat{S} \tag{4-1}$$

In figure **3-6** shows the energy level diagram for an NV center in a diamond, however, when focus is given to the ground state level anticrossing (GSLAC) around 0.1 T and to low magnetic field features, either when the nitrogen isotope is ^{15}N or ^{14}N, features such as the one in figure **4-2** are observed. The anticrossing features are vital in the NV center physics because using these features it is possible to transfer information from the nuclear spin state to the electronic spin state and are useful also for all-optical sensing purposes.

For high-density ensembles, the paramagnetic interaction between NV centers and NVs with other defect centers plays a role in the system's hamiltonian. The interaction term read as follows,

$$H_{Int} = D_{dd} \left[3(\hat{S}_1 \cdot \mathbf{n}_{12})(\hat{S}_1 \cdot \mathbf{n}_{12}) - (\hat{S}_1 \cdot \hat{S}_2) \right]. \tag{4-2}$$

In the Hamiltonian, the interaction term is defined as a function of the unitary vector $\mathbf{n}_{12}$ of the relative position between the NV and the second defect center, so the angles respect the denied coordinate system will play a role as shown in the figure **4-3**A, where $\mathbf{n}_{12}$ appears in the figure as $\hat{r}_{12}$. In addition D_{dd} is the interaction strength that depends of the relative position in between defect centers in units of MHz.

The equation 4-2 can be expressed in terms of the polar (θ) and azimuthal (ϕ) angle as shown in the figure **4-3**A, to do so, let's consider that $S_x = 1/2\,(S_+ + S_-)$ and $S_y = i/2\,(S_- - S_+)$. Then the equation can be expressed as,

$$H_{Int} = D_{dd}(A + B + C + D + E + F), \tag{4-3}$$

where,

$$A = S_z^1 S_z^2 \left(1 - 3\cos^2\theta\right), \tag{4-4}$$

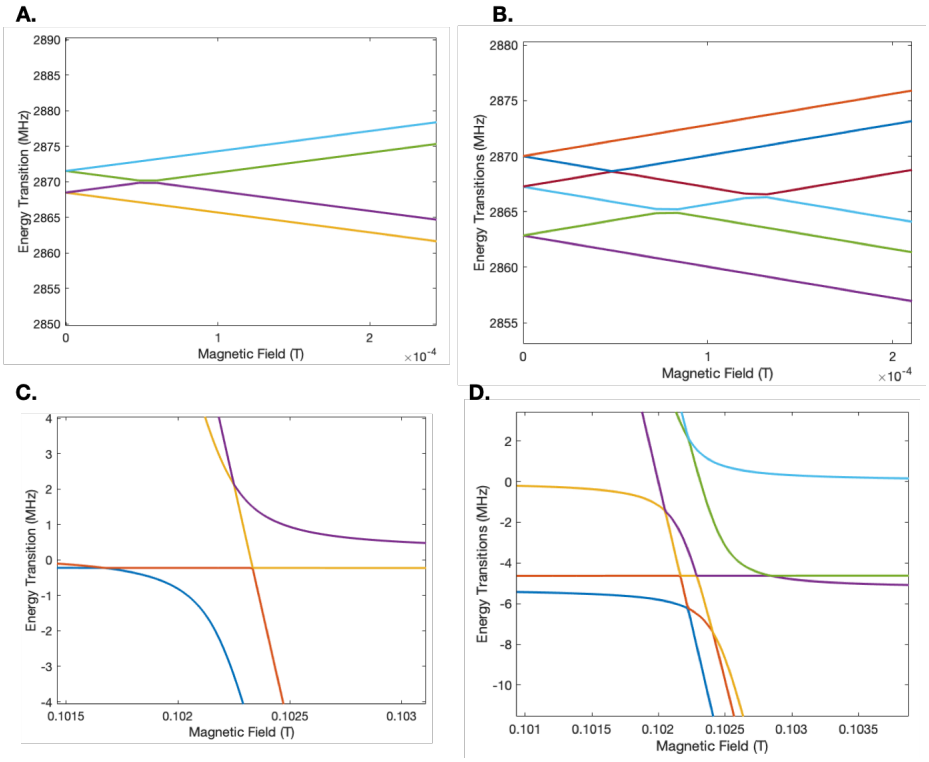

Figure 4-2: Anticrossing level states at low field and ground state for ^{15}N (A and C) and ^{14}N (B and D). For A. and C., color labels correspond to: $m_s = 1$ and $m_i = 1/2$ (light blue),$m_s = 1$ and $m_i = -1/2$ (light green), $m_s = -1$ and $m_i = +1/2$ (purple), $m_s = -1$ and $m_i = +1/2$ (yellow), $m_s = 0$ and $m_i = +1/2$ (red), and $m_s = 0$ and $m_i = -1/2$ (red); for B. And D. $m_s = 1$ and $m_i = 0$ (orange), $m_s = 1$ and $m_i = -1$ (dark blue), $m_s = 1$ and $m_i = 1$ (dark red), $m_s = -1$ and $m_i = 0$ (light blue), $m_s = -1$ and $m_i = 1$ (light green), $m_s = -1$ and $m_i = -1$ (purple), $m_s = 0$ and $m_i = 0$ (yellow), $m_s = 0$ and $m_i = -1$ (red), and $m_s = 0$ and $m_i = 1$ (blue).

$$B = \frac{1}{2}\left(1 - \frac{3}{2}\sin^2\theta\right)\left(S_+^1 S_-^2 + S_-^1 S_+^2\right), \tag{4-5}$$

$$C = -\frac{3}{2}\sin\theta\cos\theta e^{-i\phi}\left(S_z^1 S_+^2 + S_+^1 S_z^2\right), \tag{4-6}$$

$$D = -\frac{3}{2}\sin\theta\cos\theta e^{i\phi}\left(S_z^1 S_-^2 + S_-^1 S_z^2\right), \tag{4-7}$$

$$E = -\frac{3}{4}\sin^2\theta\cos\theta e^{-2i\phi} S_+^1 S_+^2, \tag{4-8}$$

$$F = -\frac{3}{4}\sin^2\theta\cos\theta e^{2i\phi} S_-^1 S_-^2. \tag{4-9}$$

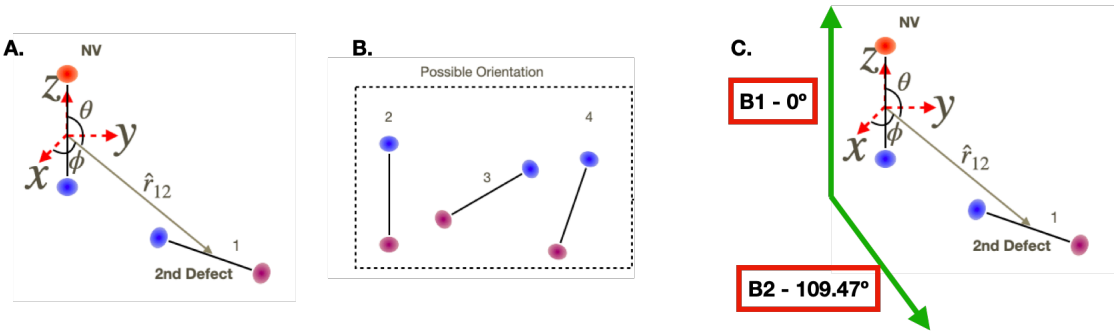

Figure 4-3: A. Representation of coordinate system respect first defect center (NV) and relative position vector respect to second defect center. B. Representation of second defect center possible orientation. C. Application of magnetic field respect the coordinate system.

The term A acts as a local static field, while B leads to flip-flop interactions. Both these terms commute with the hamiltonian, since $\Delta m_z = 0$. For this reason, they are known as the secular part of the dipole-dipole interaction. For all other terms, $\Delta m_z \neq 0$, and thus they lead transitions. They are collectively knows as the non-secular part of the Hamiltonian.

As discussed in the previous chapter, NV center can be oriented in four possible orientations, in general, the second defect center can be oriented in any of the four possible orientations as represented in figure **4-3**B. For the tensors, **A**, **Q** and the magnetic field **B** when second defect center principal axis is not parallel to the first deferec principal axis, when this is done, Tensor transforms as $\hat{R}^T(\theta,\phi,\alpha)\,\mathbf{A}\hat{R}(\theta,\phi,\alpha)$ and the vector of the magnetic field $\hat{R}(\theta,\phi,\alpha)\,\mathbf{B}$, where $\hat{R}$ is the rotation matrix.

4.2.2 Density Matrix and Von Neumann Equation

In short the density matrix describes the quantum states of a physical system. The matrix entries correspond to the quantum state's probability to occur if it is measured. On a given basis, the representation of a density matrix is given by:

$$\rho \equiv \sum_{i=1,\ldots,N} p_i |\psi_i\rangle\langle\psi_i| = \begin{bmatrix} \rho_{11} & \cdots & \rho_{1N} \\ \cdots & \rho_{ij} & \cdots \\ \rho_{N1} & \cdots & \rho_{NN} \end{bmatrix}. \tag{4-10}$$

The equation that gives the density matrix dynamics for a closed quantum system read as follows,

$$\dot{\rho} = -i\,[H,\rho]\,, \tag{4-11}$$

this is the so-called Von-Neumann Equation.

4.2.3 NV Photoluminiscence Model

The model is based on the described in [135], due to the easy implementation and the grasp of the major physical features of the quantum system. The method use the Von Neumann Equation to describe the photoluminiscence (PL) spectrum of a system of two interacting paramagnetic centers, each with a nuclear and electronic spin, in particular, paramagnetic centers such as NV and P1 (substitutional nitrogen) centers are considered. This method is introduced to describe the low-field regime, i.e. below $\sim$ 0.1T. To simplify the system, realistic assumptions, such as the following, are made as follows,

- Photo-Excitation, fluorescence, and inter-system crossing processes are faster than spin dynamics at the ground state.
- There is no energy exchange with the system surroundings; then, spin distribution is a coherent process.
- The ground state mainly gives the system's dynamics because it remains excited for a short period compared to its time at the ground level.

The first and third assumptions imply that the system transition from excited to ground state defines the initial condition for the density matrix, and this means what the electronic spin state initial polarization of the ground state is. The second condition means that the system will conserve its quantum state overall time, which means that the system will evolve with the Von Neumann Equation. The third condition allows us to ONLY use the ground state Hamiltonian to describe the system's dynamics that's why the figure **4-4** make focus on the ground state energy levels, in this case of a ^{14}N.

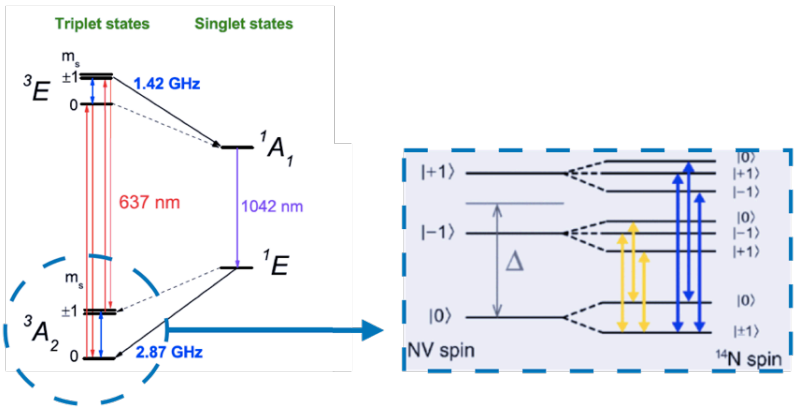

Figure 4-4: NV electronic levels with the blue dashed circled ground state energy levels describing hyperfine energy levels in the dashed blue box to emphasis the assumption of the model

The isolated NV hamiltonian correspond to equation 4-1 and when dipole-dipole interaction is considered then the term of the equation 4-2 should be included. In each case described by previous hamiltonians, we can simulate the magnetic field aligning in the NV axis direction, or 109.47 degrees with respect to the NV axis as shows in figure **4-3**.
The density matrix for the system initially is:

$$\rho_0 = \rho_{s1} \otimes \rho_{s2} \otimes \rho_{I1} \otimes ... \tag{4-12}$$

where each term in the Kronecker product corresponds to electronic spin and nuclear spin, and the indexes 1 and 2 correspond to the first defect center, NV, and 2 for the second defect center, P1 or another NV. In addition, the electronic spin polarization of the NV is given by

$$\rho_{s1} = \alpha \begin{bmatrix} 0 & 0 & 0 \\ 0 & 1 & 0 \\ 0 & 0 & 0 \end{bmatrix} + \frac{1}{3}(1-\alpha) \begin{bmatrix} 1 & 0 & 0 \\ 0 & 1 & 0 \\ 0 & 0 & 1 \end{bmatrix} \tag{4-13}$$

where the parameter α tunes the intensity of the optical polarization and it affects directly the initial condition for the electronic spin state polarization for the NV. When the NV and the magnetic field are oriented in the same direction, the parameter is 1 and when it is in the other orientation is 0.7.

After the previous definition and consideration have been made, we will now mathematically develop the method that will be used to model the fluorescence of the system. To start with, as it is observed the initial density matrix and the Hamiltonian are not on the same basis, so this means that in the frame of reference of the Hamiltonian, the density matrix evolves in time. The von Neumann equation is easily solved if the frame of reference corresponds to one where the Hamiltonian is diagonal. To do that, we make a transformation using the eigenvectors of the Hamiltonian as a matrix called $\hat{V}$, as follows:

$$\rho_0^{eb} = \hat{V}^{-1} \rho_0 \hat{V}. \tag{4-14}$$

After the transformation, it is easy to write the right side of the von Neumann equation as:

$$[H^{eb}, \rho^{eb}] = 2\pi (E_i - E_j) \rho_{ij}^{eb}, \tag{4-15}$$

Then, we can solve the von Neumann equation in this frame of reference as,

$$i\frac{d\rho_{ij}^{eb}}{dt} = 2\pi (E_i - E_j) \rho_{ij}^{eb} \rightarrow \rho_{ij}^{eb}(t) = \rho_{ij}^{eb}(0) \exp\left(-2\pi i (E_i - E_j) t\right). \tag{4-16}$$

After this, we get back to the initial frame of reference in the following way,

$$\rho(t) = \hat{V} \rho^{eb}(t) \hat{V}^{-1}, \tag{4-17}$$

and we assume that the projection of the density matrix on the $m_s = 0$, i.e. P_0 state corresponds to the evolution of the PL with time, as

$$\rho_{00}(t) = \text{Tr}\left(P_0\rho(t)\right). \tag{4-18}$$

We are interested in finding the PL as a function of the magnetic field, to do so we will calculate the average in time of the PL for each value of the magnetic field. In the average calculation, we have to take into account that the photo-excitation process interrupts the PL time evolution with time rate τ and re-initializes the system, this is taken into account in the following way in the average calculation

$$\langle\rho_{00}\rangle = \text{Tr}\left(P_0\frac{1}{\tau}\int_0^\infty \rho(t)\exp\left(-t/\tau\right)dt\right). \tag{4-19}$$

Replacing $\rho(t)$ we can see that previous equation can be written in the following way

$$\frac{1}{\tau}\int_0^\infty \rho(t)\exp\left(-t/\tau\right)dt = \frac{1}{\tau}\int_0^\infty \hat{V}^{-1}\rho^{eb}(t)\exp\left(-t/\tau\right)\hat{V}dt. \tag{4-20}$$

Solving the integral we find that,

$$\rho_{ij}^{st} = \int_0^\infty \rho^{eb}(t)\exp\left(-t/\tau\right)dt = \frac{\rho_{0,ij}^{eb}}{\left(1+2\pi i\left(E_i-E_k\right)\tau\right)}, \tag{4-21}$$

and then we can find a simplified expression in terms of the last result to find the PL through the population of ground $m_s = 0$ state

$$\langle\rho_{00}\rangle = \text{Tr}\left(P_0\hat{V}\rho^{st}\hat{V}^{-1}\right). \tag{4-22}$$

4.3 Experimental Procedure

The setup in figure **4-5** is meant to make detections of changes in fluorescence emitted by a bulk NV ensemble due to the changing magnetic field coming from the Helmholtz coil. For the light collection, we used a balanced photodiode Throlabs PDB210A that records data from fluorescence and green light. The diamond has been fabricated using CVD with a [111] cut, has an NV^- concentration of about 3.8 ± 0.25 ppm which according to the literature should exhibit features due to NV-NV interaction. The diamond is glued to a sapphire substrate that is mounted over a rotational stage Thorlabs ELL14K that allows us rotations around an axis that is perpendicular and passes through the center of the diamond face. The Helmholtz coil used is BH300-3-A 300mm from ASC scientific and gives up to 20 G for each axis when 4 A are applied. The power supply is a Rohde and Schwarz HMP2030 and it has three DC supplies that the computer can control. To record the data, a DAQ from National Instruments NI-USB6281 is used and it goes directly connected to the computer and it gathers information from the photodiode. There is

a microwave source used to calibrate the Helmholtz coil field as well as the orientation of the ensemble planes with respect to the Helmholtz coil field. Regarding the optics, we use as objective Olympus Plan N with NA 0.4 and up to 20x magnification and a dichroic Semrock FF625; lenses and mirror were disposed in such a way that the beam spot from fluorescence and green light has a size lower than the diameter of the photodiode sensor, i.e. below 5 mm.

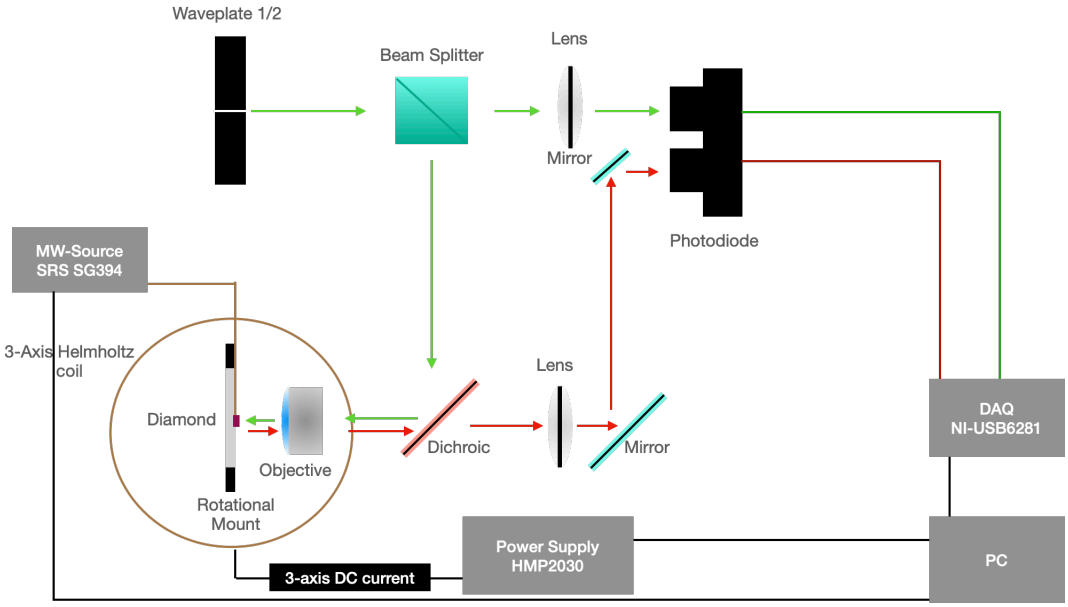

Figure 4-5: Setup for all-optical microwave free quantum magnetometer based on nitrogen-vacancy center in diamond, MW loop and signal generator are not needed, however are used for benchmarking process.

We use the experimental setup to record fluorescence change when a magnetic field generated by one axis of the Helmholtz coil is applied over the diamond. Initially, the magnetic field is applied perpendicular to the face of the diamond, which we will call B_z, by a Helmholtz axis that we will call z, and regular changes in the field are applied and the corresponding fluorescence is recorded at least ten thousand times per each magnetic field step. Secondly, when the magnetic field is applied in-plane by another Helmholtz coil axis that we will call x, the rotational mount is used to orient the crystal planes of the ensemble in such a way that when ODMR is done over the diamond the resonances look as figure **3-8**E, in this case, the ODMR is used to test the position of the crystal planes; when a field in-plane is applied perpendicular to the field generated by the x-axis, a similar resonance is observed and we will called y. Similar fluorescence measurements are done for the in-plane directions x and y. Lastly, a magnetic field is applied parallel to the NV principal axis, and information on the behavior of the fluorescence is registered.

Finally, we will realize two-dimensional maps of the fluorescence when the magnetic field is applied simultaneously in z and y, as described in the previous paragraph. Also, a 2D map will

be measured for magnetic field applied by x and y axis. After, for both configurations of two-dimensional maps, measurements are done when the planes are rotated around the z-axis. In the end, a two-dimensional plot is generated when an on-axis magnetic field, i.e. parallel to the NV axis and an off-axis (i.e. perpendicular to the NV principal axis) are applied over the diamond, simultaneously.

4.4 Results and Discussion

4.4.1 Theoretical results

Fluorescence model for isolated and interacting NV

We calculate the fluorescence as a function of the magnetic field when it is applied parallel to the NV principal axis and when it is applied 109.47 ° respect the NV principal axis as shown in **4-3**C. In figure **4-6** calculations of the fluorescence for isolated NV (A), NV interacting with a P1 (B), and NV interacting with another NV (D) are shown. In the plots for interacting NVs, we did the average of the fluorescence for those cases considering the PL when the second defect center is oriented in any of the four possible orientation and the first defect center (The NV) points out in the z direction as shown in figure **4-3**C.

In figure **4-6**A, the calculation is done for an isolated NV center. In the literature, the seven-level model is the well-established method to explore the fluorescence of NV centers, and although it considers the excited states, the method fails when an additional degree of freedom such as the nuclear spin of the nitrogen is included. In the approach we are proposing we are able to easily include an additional degree of freedom while the main physical features are considered. From the calculation, it is easy to observe that when the magnetic field is parallel to the NV axis there is a pronounced dip in the fluorescence around 0.1 T. The feature is related to the GSLAC that is presented in figure **4-2**, when this level anticrossing happens, there is a strong mixing of the quantum states from a nuclear state to another due to the hyperfine coupling. This type of feature has been used for all-optical magnetometers based on NV centers in diamond as well as for quantum information advantages.

On the other hand, the behavior of the PL when there is an off-axis component of the field shown in figure **4-6**A, it is due also to spin mixing effects, in this particular case in between electronic spin states. To picture the mixing, we can imagine that the system initially is emitting photons that proceed from a population of NV that is in a spin-up state at the beginning, however, when an off-axis magnetic field component is applied and increased, part of the population that was used to emit photons from spin up stars to transfer for another spin state that it is the mix in between the spin up and spin down state, this effect reduce the potential population that can be used for photon emission which drops then the fluorescence when the field is increasing.

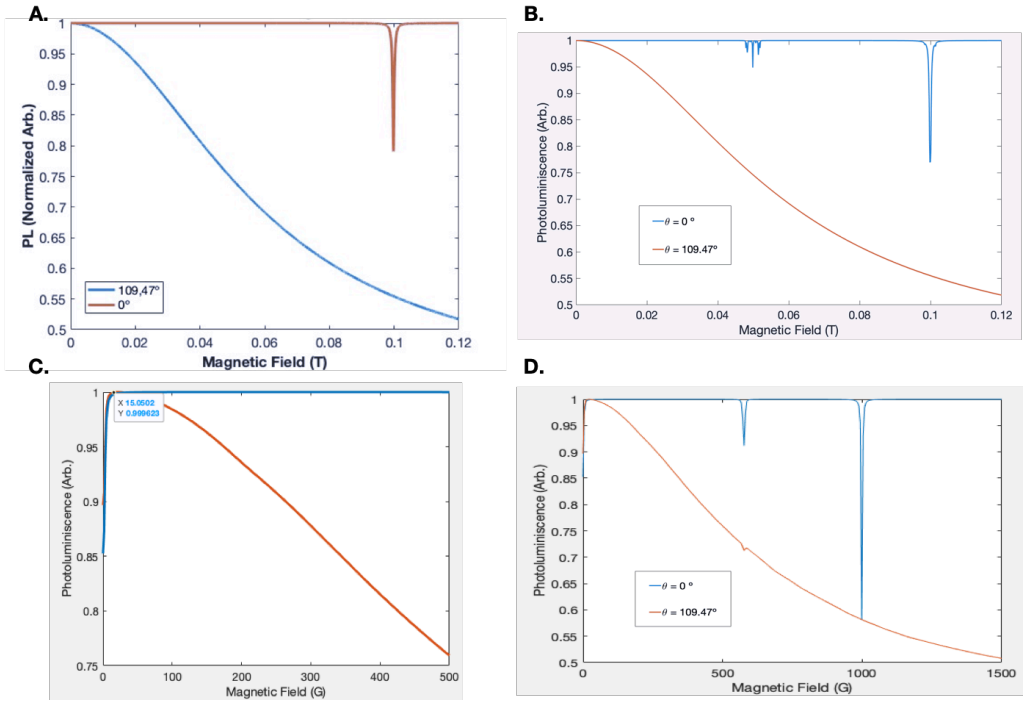

Figure 4-6: PL spectrum for different defect system. A. Isolated NV with hyperfine interaction. B. NV interacting with P1 centers. C and D. Correspond to NV interacting with another NV.

This fluorescence quenching is at the heart of all-optical and microwave-free methods using a nitrogen-vacancy center in diamond. This feature is a common behavior that is observed also for a system of interacting defect centers, such as the one presented in figures **4-6**B and **4-6**D.

Additional sharp dips in the fluorescence spectrum of NV centers in diamonds have their nature resting in the interactions among the several defect centers that are in an NV ensemble. In figure **4-6**B the dip with several wiggles appears when the field is aligned with the NV axis and it happens for values of a magnetic field around 500 G, which of course is due to the NV-P1 interaction. For figure **4-6**C and D, the features happened for low field, i.e. below 20 G, and for the field of around 600 G, the initial increase has been accounted to dynamical nuclear polarization process in between NVs from different crystal planes or equivalent NVs, called classes, as well as accounted for flip-flop process and double flip process. In general, the understanding of the mechanism that truly explains the existence of this dip is still a topic of research. In our work, we seek to develop an all-optical magnetometer based on NV center in a diamond that takes advantage of the initial increase in the fluorescence due to NV-NV interaction, that is why in our work is essential to have a clear understanding through the model on how this feature can be considered to further development of the magnetometer.

Finally, it is worth remembering that our model accounts for the average of an interacting NV center with a second defect center in their respective four possible orientation. The model is simplified, in the sense that doesn't consider the fact that the real system is an NV ensemble. However, our model is accurate in the predictions about the appearances of the sharp dips in the NV spectrum with respect to a magnetic field when applied. In the end, the measured spectrum reported in the literature, as presented in **4-1**, is the sum of the spectrum found for each particular case with an appropriate weight to account for the contribution of each system configuration into the real fluorescence spectrum.

The role of τ and n_{12}

In our model, there are parameters related to the transition rate from the ground state to the excited state that influence the average of the population. The effect is shown in figure **4-7** for the case of an interacting NV-P1, either for GSLAC or the dip around 500 G, shows that when time is increased above 1 μs the fluorescence doesn't change anymore, that suggests that the transition time is of the scale of a few microseconds, as it is well known in the literature that is the case for NV centers in diamond. In the GSLAC case call our attention that in the base of the dip additional features that for times of 0.1 μs are not observed, so it is not a matter of amplification of the depth of the deep but that also helps to resolve additional features in the spectrum.

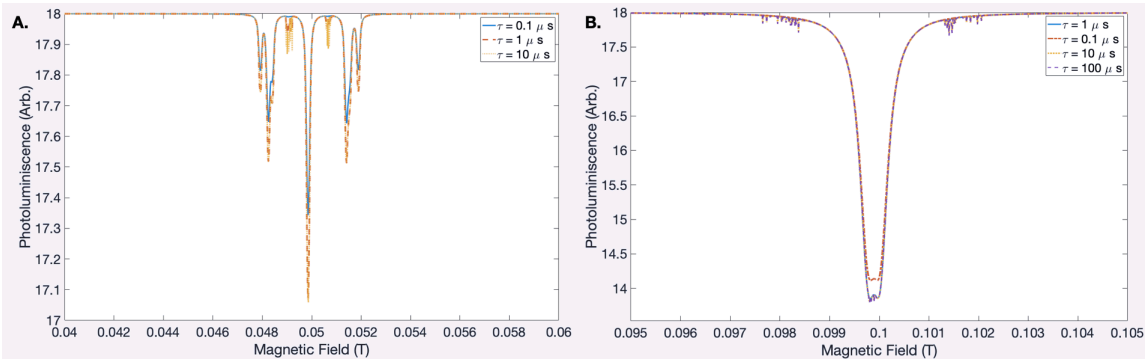

Figure 4-7: PL spectrum for different transition rate time for NV-P1. A. PL zoomed in 500 G. B. PL zoomed in GSLAC. The fluorescence have not been normalized to 1 in this figures.

In Figure **4-8**A, can be observed the photoluminescence spectrum as a function of the magnetic field for an NV interacting with a P1, for different polar angles of the relative position of the defect centers around the dip in 500 G. As can be observed the polar angle plays a role in the amplitude of the dips of the photoluminescence, which is easy to see that applies for all the deeps that are part of the spectrum in **4-8**C. Lastly, in figure **4-8**B is shown that changes on the azimuthal angle don't affect the spectrum of the fluorescence. From now on, the calculations will be done assuming the polar angle is 90°, the azimuthal angle is 0° and the optical transition time or decay rate is about 1 μs.

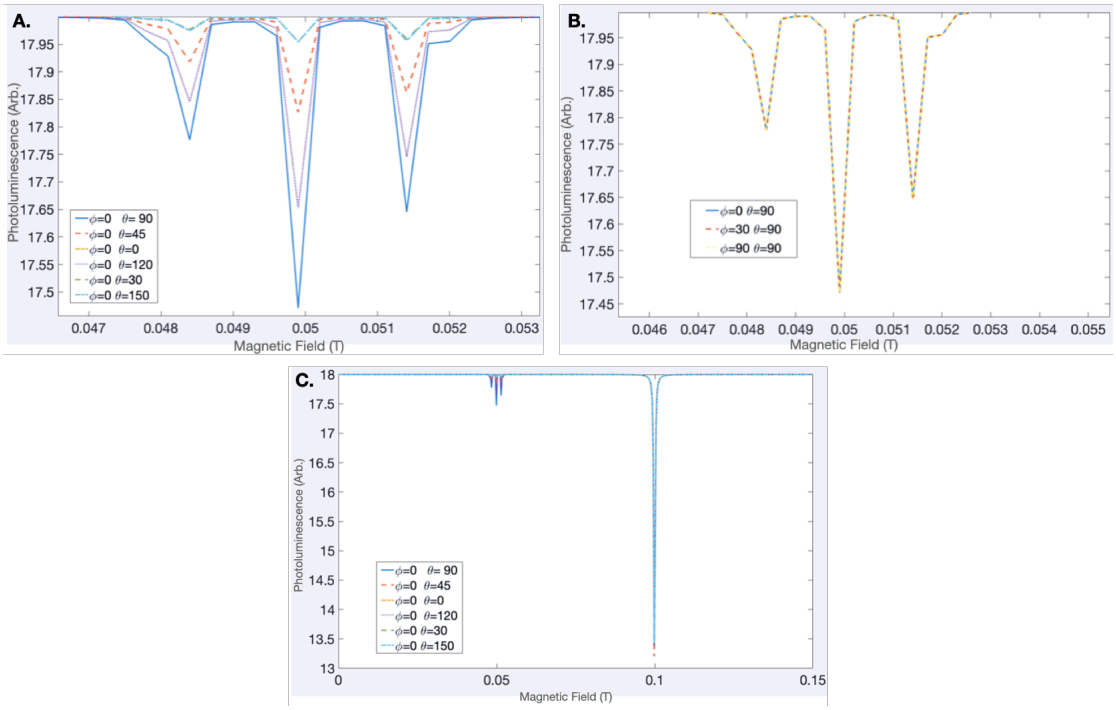

Figure 4-8: A. and B. PL spectrum for different azimuthal and polar angles for NV-P1. A. PL zoomed in 500 G for different polar angles. B. PL zoomed in 500 G for different azimuthal angles. C. PL spectrum up to 0.15 T for different polar angles.

4.4.2 Experimental results

One-dimensional NV centers ensemble PL at low field

The figure **4-9**A shows the fluorescence of NV centers when the magnetic field is applied by the Helmholtz coil Z and X axis as discussed before, clearly, the magnetic field direction over the sample plays a valuable role in the slop of the initial increase of the fluorescence, where for the case when the field is in Z presented a more high slop. This finding is valuable in order to determine what is the specific setting of the magnetometer that gives us the highest sensitivity if it is understood as the slop of the PL spectrum. However, further research should be done to establish a reliable way to define sensitivity for this type of magnetometer.

For the simulation shown in figure **4-9**B, we are going to now consider the first NV could be in any of the other three possible orientations of the diamond crystal structure and the system is just interacting with another NV center, with this in mind we will have 16 possible configurations of our interacting NV-NV system in the average calculation of the PL. In the plot, the results are consequent with the observation in the sense that the initial fluorescence increase for the case of the magnetic field in x has a fluorescence that is above of the case when the magnetic field is applied in z. In our model, as mentioned before, additional improvements should be considered

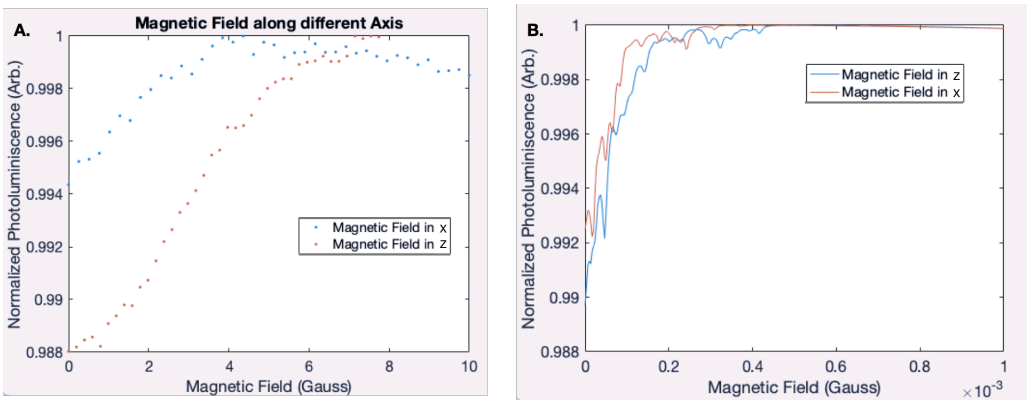

Figure 4-9: Experimental (A) and theoretical (B) simulations of fluorescence at low field for different axis orientation.

in order to better match the experimental results, but even in this case, the model still gives us insight into the order of magnitude of difference between the fluorescence from each case ($\sim$ 0.001) which correspond to the experimental observations.

Linear polarization effects in the fluorescence increase

In previous literature [135], it has been reported that linear polarization plays a role in the initial PL increase when the magnetic field is applied on-axis. Due to that our interest rest in looking for parameters that play a role in the improvement of the slope of the initial increase, we explore the effect of the light polarization by using a linear and circular polarizer before the green light hit the diamond but that is not in the path of the collected red light, each at a time.

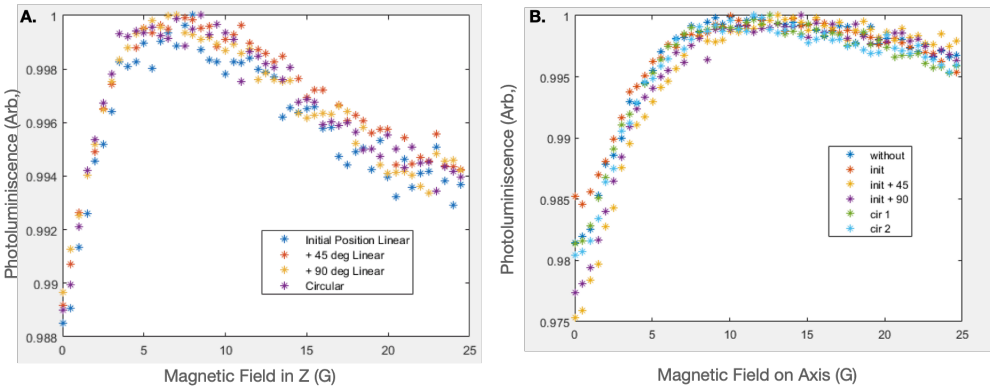

Figure 4-10: Fluorscence affected by linear or circular polarization for field oriented in z (A) and on-axis (B)

The reported results of our studies are shown in figure **4-10**, in A the magnetic field is applied in Z, and in B the magnetic field is applied parallel to the NV principal axis, i.e. on-axis, as it is

observed the initial fluorescence is affected by the linear polarization when the magnetic field is applied On-axis, in addition, when the field is applied in z, the slope is still better than when the field is applied on-axis. Secondly, the effect on the polarization changes the initial PL in almost 0.005 units, we point out that the error bars of the fluorescence of our data point is 0.0005 units, this suggests that our linear polarization changes directly the initial PL, and the initial change is not an artifact. Finally, the circular polarizer doesn't change the initial fluorescence increase, for either case.

These results are related to the fact that when light linear polarization is changed, some NV classes are stimulated to emit more fluorescence than others, several additional techniques using microwaves have allowed us to observe this phenomenon before, however, this corresponds to one of the first times this results is reported to the community, for the best of our knowledge.

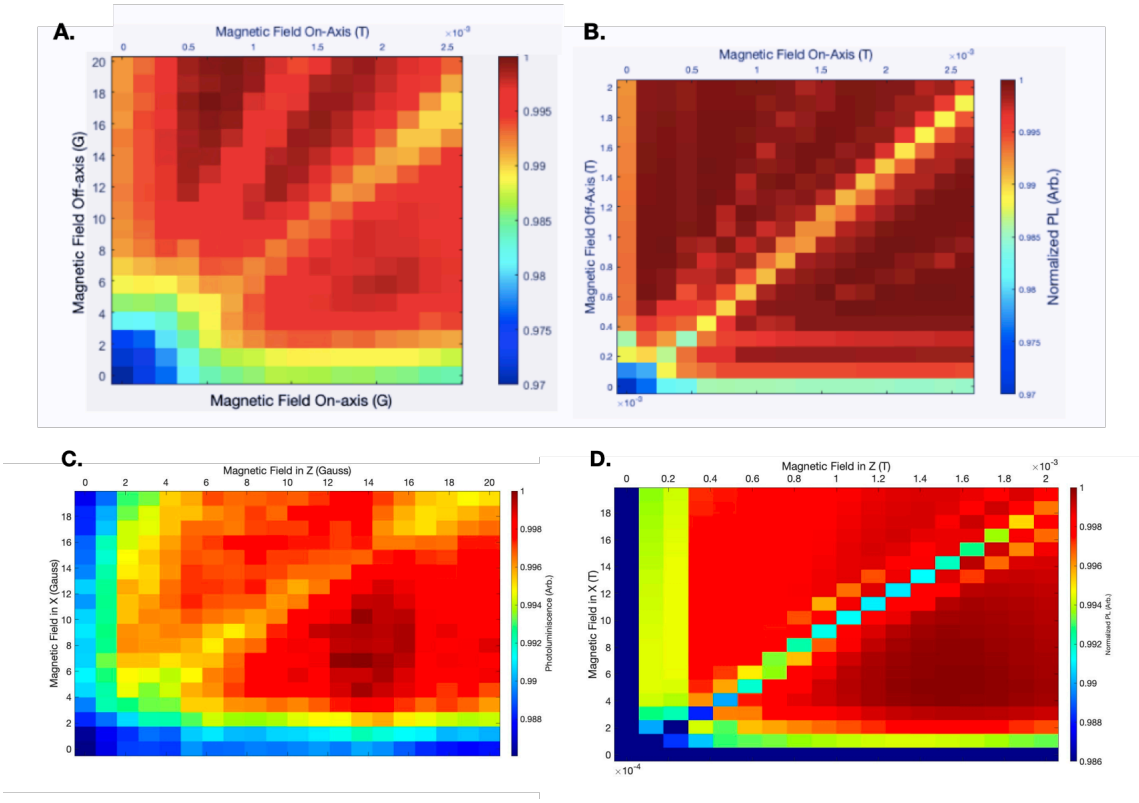

Figure 4-11: Theoretical (B and D) and experimental (A and C) results of two dimensional fluorscece from a magnetic field coming from two different directions. A. and B. correspond to on-axis and off-axis magnetic fields.. C. and D. correspond to z and x axis magnetic fields

Two-dimensional fluorescence maps

The two dimensional map are valuable tool in our study because this reveal information about region where the changes in the fluorescence are abrupts, this region offers a playground for all-optical measurement with high sensitivity. Plots A and B in figure **4-11**, correspond to the experimental results and theoretical simulations for the case when the magnetic field is applied in an on-axis and off-axis setting, the magnetic field range and the colormap have the same scales for simulations and measurement; Plots C and D are the same type of plot, but when the magnetic field is applied in z and x. The nature of the sharp changes in the fluorescence map, that looks like thick lines in the colormap, are due to the presence of NV-NV interaction. Comparing plots A and C, the lines that appears depends on the orientation of the applied magnetic field, because the number of lines that appears and the intensity of the map change due to orientation change of the field, additional discussion about it will be done in later section. Finally the experimental results and the simulation results shows agreement in the features that the fluorescence two dimensional map exhibit when the magnetic field is changed simulatoneasly in two perpendicular directions, this can be noticed either by comparing the contrast of the intensity of fluorescence for theoretical predictions and experimental results, or by looking at the locations of the the features lines that appears in simulated and experimental plot.

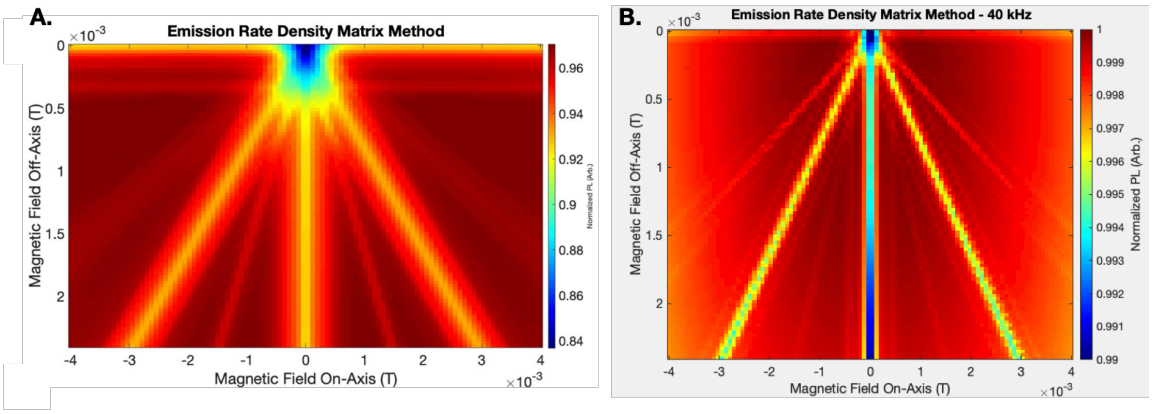

Figure 4-12: Fluorscence spectrum due on-axis and off-axis magnetic field for two different interaction strength, 1 MHz (A) and 0.04 MHz (B)

In figure **4-12**A and **4-12**B, the interaction strength in the former is about 1 MHz and in the later around 40 kHz. Using this simulation can explore how when the interaction strength get weaker the features lines, where sharp changes in fluorescence happens, start to vanish and reduce their sharpness changes in intensity. This result is a clear evidence about the role that play the density of NV centers in diamond in the existence of this features. In our simulations in figure **4-11** we are using a few hundred of MHz strength. As discussed previously the existance of this initial increase of fluorescence is related to NV-NV cross-relaxation, this means that initially when there is not field, NVs from different crystallographic planes have same energy levels

this allows the transfer of population from one NV from a particular orientation to another in other crystal orientation because of the coupling due to their interaction , in the case when the interaction is negligible this transfer is not possible hence all the population is emitted as light, but in former case all the population is not available for light emission then a lower value of fluorescence is observed at low magnetic fields[142]. In the following, we will establish how the different NV classes in each crystallographic plane, play a role in the appearances of the lines in the PL two-dimensional map.

Two-dimensional fluorescence maps for different crystal planes orientation

In these experimental results, we consider that 45° corresponds to the case when resonance from each NV overlapped all together due to the in-plane field by either x or y axis from the Helmholtz coil. Then the procedure is that with the rotational mount, we rotate the diamond around the z axis of the Helmholtz coil about 15°. To check the alignment we did ODMR measurements for different magnetic field when B_x is applied and identified if there was just two resonance peak.

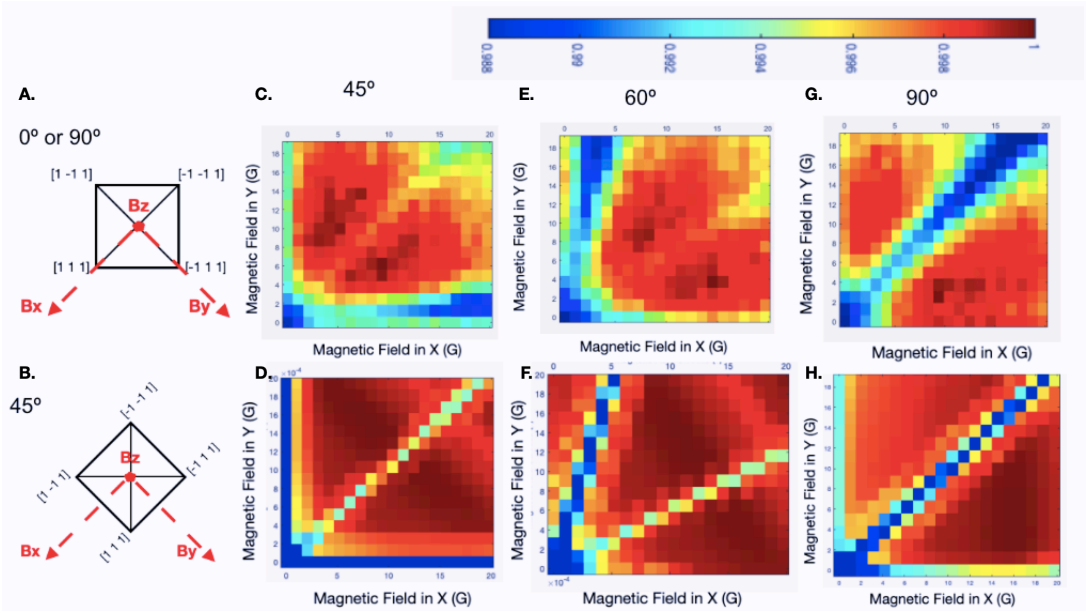

Figure 4-13: Theoretical (D,F, and H) and experimental (C,E, and G) results for different diamond orientations when the magnetic field is applied in by B_x and B_y. A. and B. are different orientation of an ensemble of NV center from a top view. The colorbar for all the two dimensional map is the same.

In figure **4-13** and **4-14**, sketches A and B, are how the crystal planes look with respect to the applied magnetic field for different angles in a top view of a unit cell. Experimental results are shown in figure **4-13**C, E, and D for different angles, as well as simulations are shown in figures **4-13**D, F, and H, all the figures share the same color bar. In measurements from figure **4-13** the

angles don't correspond exactly to the mentioned value, it can be observed when simulations and measurements are compared, however, the angle is close to the claimed one.

The first insight from the experimental results from figures **4-13** is that each line comes from NV-NV cross relaxation when the magnetic field is equally projected into the crystallographic planes of the interacting NVs. To draw this point, let us consider figure **4-13**D or C, when the B_y is off, and B_x is applied, the fluorescence have a value defined by the dark blue color intensity in the map, that represents the lowest fluorescence from the system. This also happens because when only B_y is applied. In the previous described setting, the projection of the field is equal over the NVs that are in the plane parallel to B_x or B_y. To notice also the previous point consider the case when in figure **4-13**D or C the field applied all the time is $B_x = B_y$, in such a case also a line related to cross relaxation feature is presented due to the equal project of the field into all the NVs crystal planes, but in this time there is more emission of fluorescence than in the case when the field is just applied in B_x or By. To finish, notice that when the field do not hold any of previous condition the fluorescence don't exhibit any particular feature, suggesting then the need of an equal projection over at least two NVs in the same crystal plane to exhibit some cross relaxation lines feature in the 2D PL map.

The second point is that it is easy to notice that the physical rotation of the NV ensemble is reflected in an equal rotation of the feature lines in the fluorescence map. To showcase this, let's compare plots **4-13**D and H, the horizontal or vertical dark blue line at the edge of figure D corresponds to the line with 45 ° angle respect the B_x axis in figure H, this is because now, in the configuration of 90 ° it is needed to apply the same amount of B_x and B_y at the same time to talk to the four NV classes, which in the setting of 45 ° degrees corresponds to the application of only B_x or B_y when the other was off. Similarly observing plot **4-13**F and E, a rotation of 15 ° can be estimated for the light blue line feature that in the case of figure D was diagonal to the plot. It is worth mentioning that some feature lines in the experimental result are a bit vanished due to noise from measurement, however, the general pattern can be appreciated.

According to these results, the appearance of these feature lines is due to cross-relaxation between different NV classes, which is in agreement with the current understanding on the phenomena in 1D PL plots in the literature[142]. In our work we are able to visualize and predict this behavior by using our field all optical magnetometer and our theoretical model, as well as observe that the cross relaxation features in the 2D PL maps are represented as sharp intensity contrast lines which are influenced by the equal projection of the field into the different NV classes, however further first principle explanation about the mechanism that explains this features is required. From now on, the mentioned features will mentioned as cross-relaxation lines.

In figure **4-14**C and D, we have an equivalent case to the one discussed in previous results, where when each field is applied individually when the other is off, then all the NV classes are

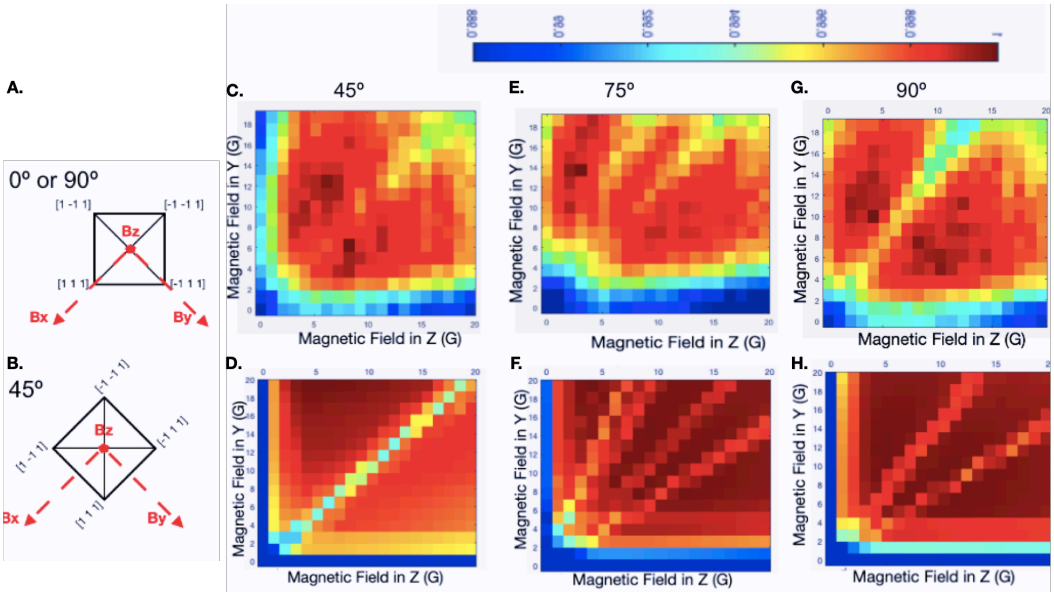

Figure 4-14: Theoretical (D,F, and H) and experimental (C,E, and G) results for different diamond orientations when the magnetic field is applied in by B_z and B_y. A. and B. are different orientation of an ensemble of NV center from a top view. The colorbar for all the two dimensional map is the same.

influenced equally by the field, enhancing the cross-relaxation. Figure **4-14**E and F look more complicated because when B_y and B_z are applied in such a way that their resulting vector points out in a specific orientation, it influences the cross-relaxation lines of cases when the projection is over 2,3 or 4 NV classes, each cross-relaxation line corresponds to the specific angles for that to happend. However, further research should be done to improve the experimental result to properly visualize all the cross-relaxation lines. Lastly, Figure **4-14**G and H, shows when there is one NV class that is parallel to the magnetic field and there are three that are equally projected to that field, the cross relaxation lines observed correspond to this particular situation.

Finally, it is worth mentioning that further research should be done in order to improve the resolution of the experimental results presented due to noise effects. A way to overcome this is the use of a lock-in amplifier that allows us to modulate the magnetic field in a way that the noise can be cancelled, This procedure offers the derivative of the PL measurements. In addition, further investigation should be done to explain the mechanism about how the magnetic field projection influences in the contrast observed in the cross-relaxation lines. The all-optical magnetometer methods presented in this work, show the best sensitivity when the sensing field is applied in a perpendicular direction to the cross-relaxation lines, due that in those locations the change in fluorescence is sharp which means that are regions for high sensitivity, however, further improvement of the experimental setup should be introduced to make an appropriate estimation of the sensitivity of our experimental setup. Our work paved the way to a better

understanding of the cross-relaxation effect of a high-density ensemble in the sensitivity of an all-optical magnetometer based on NV centers in diamond which could have applications for biotechnology, condensed matter physics, and study of geological samples at low field [143, 138].

4.5 Summary

- In this chapter we engineer and build a functional all-optical microwave magnetometer based on NV centers in diamond, upon this we developed a numerical simulation that correctly predicts and explains several features observed experimentally.
- On the experimental side, when a one-dimensional PL spectrum is measured, we found that when the magnetic field is changed perpendicularly to the face of the diamond the initial increase shows a better slope than when the field is applied on x or on-axis.
- Our numerical simulations calculate the one-dimensional PL spectrum when an on-axis magnetic field is applied in two possible NV orientations. Our results agree on the location of the features observed in the literature which are due to NV-NV interaction around 600 G, NV-P1 interaction around 500 G, and GSLAC around 1000 G. In addition, our method shows that fine-tuning of parameters such as the transition rate time, the n_{12} and the interaction strength open the door to better modeling.
- Our exploration of the effects of linear and circular light polarization gives us insights into the role that play in the PL spectrum at low-field. Circular polarization does not affect the PL spectrum at low field, but interestingly, the linear polarization only affects when the magnetic field is applied over an on-axis NV center, the effect to the linear polarization are not observed when the field is in z direction.
- The CR effect related to the crystal planes directly affected by the magnetic field is exhibited by CR lines in the two-dimensional plot, which are connected to the crystallographic structure of the NV classes due to the direct correlation in between the physical rotation of the diamond and the rotation of CR lines in the two-dimensional plot for fluorescence. Our simulation accounts for our experimental findings and our insights offer further exploration of the nature of the CR process that happens at low field.
- Our methods clearly suggest that the most sensible region for sending purposes corresponds to those near CR lines, in particular in the perpendicular direction to them where the highest sensitivity is observed.

5 Conclusion and Outlook

Initially we claim as the main purpose of this work: the development and/or application of novel theoretical and experimental methods to explore relevant and exotic condensed matter systems. To show that our goal have been accomplished, we will walk through a general overview of the key achievements from each chapter. In the second chapter of this thesis, we have developed a new generalized Green function method for Dirac materials based on the microscopic properties of our systems that allows us to determine closed-form and analytical results for measurable quantum transport properties in graphene-like materials that have infinite, semi-infinite and finite sizes and have different type of boundary conditions, in particular this method allows us to study semiconducting, insulating, metallic and topological phases in materials such as germanene and TMDs. After, in our third chapter we fully introduce and describe a novel quantum sensing technique that is starting to be a well-established method in the community, quantum magnetic imaging using NV centers in diamond to study Van der Waals magnets, by using this method we were able to reveal room temperature ferromagnetism in FGT and CFGT in samples with thickness as little as 7 unit cells and with this magnetic imaging technique we were able to screen several flakes simultaneously. In our last chapter, we have engineered and developed a new all-optical and microwave-free magnetometer based on NV center in diamond for low magnetic field regime, as well as develop a numerical simulation that predicts the behavior of the fluorescence due to the magnetic field which allows us to understand the cross-relaxation effects which when tuned appropriately are key to the enhancement of the sensitivity of the sensor, our results show that implementation of the magnetometer close to cross-relaxation lines in the two-dimensional maps improves sensitivity; our finding paves the way to the implementation of such magnetometer for application in the study of relevant condensed matter systems such as Van der Waals materials or high-temperatures superconductor at low temperatures. So far, we believe that the independent parts of our work expose the same philosophy and are highly correlated, all of them propose a new technique or use a recently developed novel technique to explore equivalent measurable physical quantities with the end goal of exploring condensed matter systems, in our manuscript particularly we study the family of the two-dimensional material, however, all the techniques are applicable beyond that.

Some possible future directions of research based on the integration of the developed techniques and studied materials are the following. The use of the generalized Green function method allows the engineering of junctions based on two-dimensional graphene-like materials or Dirac materials, for instance studying the junction of different TMDs will allow us to

get insights into the electronic and optoelectronic properties of atomically p-n heterojunctions based on this type of semiconductors by applying our developed method [144]. In addition, our method can be extended to the engineering of heterostructure based on superconductors and graphene-like materials with the purpose of studying the scattering process at the interfaces [55]. Finally, recently realized Dirac magnon quasiparticles correspond to quantum excitations in a honeycomb structure that has been reported in CrI_3 with a Hamiltonian that after some manipulation can be transformed into a dirac hamltonian, which could be properly studied by the natural extension of the generalized Green function method to include peculiarities of this system, which will allow the inclusion of new type of Dirac excitation into the method [145, 146].

In general, the green function technique allows the engineering and simulation of several interesting devices with topological phases [147], in addition to this, the properties of such devices could be explored by using a probe nitrogen-vacancy center in diamond either as a magnetometer or for sensing an electric field [116, 97], either way, will allow the study of quantum transport properties, to understand this point we have to aware of the fact that magnetic field generated by two-dimensional material can be imaged by this quantum sensor but in addition to this, the map of the electric or spin current in the surface of this material can be done by using the magnetic field map, revealing in this way transport properties of the materials as recently was done for the Dirac viscous flow in graphene [32], techniques like this using NV-QMI can be extended to all the family of graphene-like materials, the key to do this, is that the inverse problem of finding the distribution current given a magnetic field is mathematically solvable in two dimensions. In addition to this, findings from our thesis such as the topological insulating properties from materials such as silicene and germanene could be probed by using NV-QMI, the reason relies in the fact that at the edge of these graphene-like materials, there are topologically protected current states with different helicity [44, 58], this makes the current at the edge move in opposite direction respect each other, these currents should have associated to a magnetic field which can be measured by NV-QMI, currently two-dimensional current flow in the edge of 2D material due to topological phase have not been experimentally observed yet.

Another possible direction of the use NV-QMI technique corresponds to the use of the technique as a way to study temperature-dependent VdW materials with magnetic properties or with interesting electric properties for valleytronics or spintronics [148, 69, 149, 150], due to multi-modal characterization capabilities of NV-QMI because the fine term is a temperature-dependent and can be calculated by knowing the sum of the resonance frequencies over the system and the magnetic field by the difference of the resonance frequencies [97], this then opens the doors to simultaneous screening and characterization of multiple physical parameters of this type of system, then magnetic hysteresis curve and additional ways to prove magnetism or other electronic properties can be tested by using this method without being electrically invasive into the sample of interest.

Finally, due that very recent evidence of sensitivity as low as 6 nT/$\sqrt{Hz}$ for all-optical magnetometry with NV centers in diamond at low field [143, 138], it is possible to use this method as a reliable sensing technique for imaging modality as QMI but microwave-free. Remember that the fields of the flakes were of the order a few tens of μT, which suggests that possible sensitivity for the modality is good enough to study this system at room temperature, however, due to the flexibility that this type of method have to explore cryogenic temperature, further studies of VdW material as CFGT and FGT, and beyond those, can be done at such regime with a competitive sensitivity. It is worth mentioning that QMI modality without a microwave has not been reported, so this is a promising path in the further development of the technique. In addition to this, the use of the technique using optical Fourier processing method citeBacklund2017Nov allows to the stimulation with green light directly of a specific NV class in the crystal structure could allow us to enhance our current insight into the role of different NV classes explored through our measurements and theoretical methods .

The novel developed methods as well as the exotic physical system studied offer a rich landscape of possibility for the application of the techniques as well as the further use of the materials for technological and fundamental physics purposes.

6 Appendix

6.1 Generalized Green function method for Dirac Materials

6.1.1 Semi-infinite system

Equation 2-22 is one key step in our calculations that is fundamental to the development of the method. The way we find this results is shows as follows,

$$\check{W}^{>}(x) = U_a \check{g}^{>}(x, x_a)\,\check{\tau}_a \sum_{p=0}^{\infty} \left(U_a \check{g}^{>}(x_a, x_a)\,\check{\tau}_a\right)^p . \tag{6-1}$$

Using the completeness relation, 2-16, we find

$$\begin{aligned}\check{g}^{>}(x_a, x_a)\,\check{\tau}_a =& \frac{-i}{2\hbar v_F} \sum_n \psi_n^{+} (\bar{\psi}_n^{+})^T \check{\tau}_a \sum_{m,\varepsilon} \psi_m^{\varepsilon} (\tilde{\psi}_m^{\varepsilon})^{\dagger} \\ =& \frac{-i}{2\hbar v_F} \sum_{n,m,\varepsilon} \tau_{a,nm}^{+\varepsilon} \check{P}_{nm}^{+\varepsilon},\end{aligned} \tag{6-2}$$

where we have defined the projector operators

$$\check{P}_{nm}^{\varepsilon\varepsilon'} = \psi_n^{\varepsilon} (\tilde{\psi}_m^{\varepsilon'})^{\dagger}, \tag{6-3}$$

and the matrix representation of $\check{\tau}_a$ as

$$\tau_{a,nm}^{\varepsilon\varepsilon'} = (\bar{\psi}_n^{\varepsilon})^T \check{\tau}_a \psi_m^{\varepsilon'}. \tag{6-4}$$

As a result, 2-22 becomes

$$\check{W}^{>}(x) = \sum_{n,m,\varepsilon} f_n^{+}(x - x_a)\,(\hat{r}_a^{+\varepsilon})_{nm} \check{P}_{nm}^{+\varepsilon}, \tag{6-5}$$

Analogously,

$$\check{W}^{<}(x) = \sum_{n,m,\varepsilon} f_n^{-}(x - x_a)\,(\hat{r}_a^{-\varepsilon})_{nm} \check{P}_{nm}^{-\varepsilon}, \tag{6-6}$$

with $\hat{r}_a^{-\varepsilon} = \hat{D}_a^{-} \hat{\tau}_a^{-\varepsilon}$.

6.1.2 Iterative method

In this section, we obtain $\check{W}^{>}(x)$ given in 6-1 following an iterative method. First, we start using 2-22 with $x < x'$ in the definition of the GF,

$$\check{G}_a^{<}(x,x') = \check{g}^{<}(x,x') + \check{g}^{>}(x,x_0)\, U_a \check{\tau}_a \check{G}_{RR}^{<}(x_0,x')\,. \tag{6-7}$$

Here, $\check{G}_{RR}^{<}(x_0,x')$ is given by Dyson's equation, 2-21, as

$$\check{G}_{RR}^{<}(x_0,x') = \left[1 + \check{W}^{>}(x_0)\right] \check{g}^{<}(x_0,x')\,. \tag{6-8}$$

Substituting into 6-7 we get

$$\begin{aligned}\check{G}_{RR}^{<}(x,x') =& \check{g}^{<}(x,x') + \check{g}^{>}(x,x_0) \\ &\times U_a \check{\tau}_a \left(1 + \check{W}^{>}(x_0)\right) \check{g}^{<}(x_0,x')\,.\end{aligned} \tag{6-9}$$

Comparing 6-9 with 2-21, namely,

$$\check{G}_a^{RR,<}(x,x') = \check{g}^{<}(x,x') + \check{W}^{>}(x)\, \check{g}^{<}(x_0,x')\,,$$

we obtain the following equation for $\check{W}^{>}(x)$,

$$\check{W}^{>}(x) = \check{g}^{>}(x,x_0)\, U_a \check{\tau}_a + \check{g}^{>}(x,x_0)\, U_a \check{\tau}_a \check{W}^{>}(x_0) \tag{6-10}$$

We then solve 6-10 recursively to find

$$\check{W}^{>}(x) = U_a \check{g}^{>}(x,x_0)\, \check{\tau}_a \sum_{p=0} U_a^p \left(\check{g}^{>}(0)\, \check{\tau}_a\right)^p. \tag{6-11}$$

6.1.3 Scattering matrix

We now derive the expression and general properties of the scattering matrix in 2-28. To define the scattering problem, we consider a potential barrier at $x = x_a$. Incoming states from the left (right) of the barrier are $\psi_m^{+}(x)$ with amplitudes a_m^{+} ($\psi_m^{-}(x)$ with a_m^{-}), which are solutions of 2-12. In the absence of a potential barrier, a general unperturbed scattering state reads

$$\psi_0(x) = \sum_{m,\varepsilon} a_m^{\varepsilon} \psi_m^{\varepsilon}(x)\,. \tag{6-12}$$

In the presence of the barrier potential, the perturbed state to the left or right of the barrier is obtained using Dyson's equation as

$$\psi_{L(R)}(x) = \psi_0(x) + \check{W}^{<(>)}(x)\, \psi_0(x_a)\,, \tag{6-13}$$

with $\psi_m^{\varepsilon}(x) = \psi_m^{\varepsilon} f_m^{\varepsilon}(x)$ and $f_m^{\varepsilon}(x) = e^{i\varepsilon k_m x}$.

Owing to the translational invariance along the x-direction, we proceed taking $x_a = 0$ without loss of generality. For simplicity, we also define $\psi_R(0) = \psi_R$ and $\psi_0(0) = \psi_0$ and obtain

$$\begin{aligned}\psi_R = & \left[1 + \check{W}^{>}(0)\right]\psi_0 \\ & = (1 + \sum_{n,m,\varepsilon} \left(\hat{r}_a^{+\varepsilon}\right)_{nm} \hat{P}_{nm}^{+\varepsilon}) \sum_{m',\varepsilon'} a_{m'}^{\varepsilon'} \psi_{m'}^{\varepsilon'} \\ & = \sum_{m,\varepsilon} a_m^{\varepsilon}\psi_m^{\varepsilon} + \sum_{n,m,\varepsilon} \left(\hat{r}_a^{+\varepsilon}\right)_{nm} a_m^{\varepsilon}\psi_m^{+}, \end{aligned} \tag{6-14}$$

where we have used that $\hat{P}_{nm}^{+\varepsilon}\psi_{m'}^{\varepsilon'} = \delta_{\varepsilon,\varepsilon'}\delta_{m,m'}\psi_{m'}^{\varepsilon'}$. Summing over ε we get

$$\psi_R = \sum_m a_m^- \psi_m^- + \sum_n b_n^+ \psi_n^+, \tag{6-15}$$

with b_n^+ being the outgoing scattering amplitudes,

$$b_n^+ = \sum_m \left(\hat{r}_a^{+-}\right)_{nm} a_m^- + \sum_m \left(\hat{t}_a^{++}\right)_{nm} a_m^+. \tag{6-16}$$

Here, we have defined the transmission amplitudes as the elements of the following matrix

$$\hat{t}_a^{++} = \hat{1} + \hat{r}_a^{++}, \tag{6-17}$$

which allows us to rewrite eq:appb1 as

$$\mathbf{b}^+ = \hat{r}_a^{+-}\mathbf{a}^- + \hat{t}_a^{++}\mathbf{a}^+, \tag{6-18}$$

with

$$\mathbf{b}^{+T} = (b_1, b_2, ..., b_N)^T, \tag{6-19}$$

$$\mathbf{a}^{+T} = (a_1, a_2, ..., a_N)^T. \tag{6-20}$$

The perturbed scattering state to the left of the barrier is obtained analogously as

$$\psi_L(0) = \sum_m a_m^+ \psi_m^+ + \sum_n b_n^- \psi_n^-, \tag{6-21}$$

with

$$\mathbf{b}^- = \hat{r}_a^{-+}\mathbf{a}^+ + \hat{t}_a^{--}\mathbf{a}^-, \tag{6-22}$$

and

$$\hat{t}_a^{--} = \hat{1} + \hat{r}_a^{--}. \tag{6-23}$$

Combining the previous results, we define the scattering matrix $\hat{S}$ as

$$\mathbf{b} = \check{S}\mathbf{a}, \tag{6-24}$$

with

$$\mathbf{b} = \begin{pmatrix} \mathbf{b}^{+} \\ \mathbf{b}^{-} \end{pmatrix}, \quad \mathbf{a} = \begin{pmatrix} \mathbf{a}^{+} \\ \mathbf{a}^{-} \end{pmatrix}. \tag{6-25}$$

Note that in the usual definition of the scattering matrix the reflection amplitudes are in the diagonal, which results from taking $\mathbf{b}^{T} = (\mathbf{b}^{-T}, \mathbf{b}^{+T})$. In what follows, however, we use

$$\begin{aligned} \check{S}_a &= \begin{pmatrix} \hat{t}_a^{++} & \hat{r}_a^{+-} \\ \hat{r}_a^{-+} & \hat{t}_a^{--} \end{pmatrix} \\ &= \begin{pmatrix} \hat{1} + \hat{r}_a^{++} & \hat{r}_a^{+-} \\ \hat{r}_a^{-+} & \hat{1} + \hat{r}_a^{--} \end{pmatrix} \\ &= \check{1} + \check{r}_a. \end{aligned} \tag{6-26}$$

We can now set the potential barrier at an arbitrary position $x_a \neq 0$ changing the scattering matrix as

$$\check{S}\left(x_a\right) = \check{f}\left(-x_a\right) \check{S} \check{f}\left(x_a\right), \tag{6-27}$$

with

$$\check{f}\left(x_a\right) = \begin{pmatrix} \check{f}^{++}\left(x_a\right) & 0 \\ 0 & \check{f}^{--}\left(x_a\right) \end{pmatrix} \tag{6-28}$$

and

$$\left(\hat{f}^{\varepsilon\varepsilon}\right)_{nm}(x) = \delta_{nm} \hat{f}_m^{\varepsilon}(x). \tag{6-29}$$

Here, $\hat{S}\left(x_a\right)$ and $\hat{S}$ are related by an unitary transformation since $\hat{f}\left(-x_0\right)\hat{f}\left(x_0\right) = \hat{1}$.
As it is usually interpreted, **b** represents the outgoing flux and **a** the incoming one. Consequently, the probability flux to the right and left of the barrier reads

$$\begin{aligned} J_R &= v_F \sum_n \left(a_n^{-*} \psi_n^{-\dagger} + b_n^{+*} \psi_n^{+\dagger}\right) \hat{\alpha}_x \sum_n \left(a_n^{-} \psi_n^{-} + b_n^{+} \psi_n^{+}\right) \\ &= v_F \sum_n \left(\left|b_n^{+}\right|^2 - \left|a_n^{-}\right|^2\right), \end{aligned} \tag{6-30}$$

$$\begin{aligned} J_L &= v_F \sum_n \left(a_n^{+*} \psi_n^{+\dagger} + a_n^{-*} \psi_n^{-\dagger}\right) \hat{\alpha}_x \sum_n \left(a_n^{+} \psi_n^{+} + a_n^{-} \psi_n^{-}\right) \\ &= v_F \sum_n \left(\left|a_n^{+}\right|^2 - \left|b_n^{-}\right|^2\right). \end{aligned} \tag{6-31}$$

Conservation of the probability flux requires that $J_L = J_R$; therefore,

$$\sum_n \left(\left|a_n^{+}\right|^2 - \left|b_n^{-}\right|^2\right) = \sum_n \left(\left|b_n^{+}\right|^2 - \left|a_n^{-}\right|^2\right), \tag{6-32}$$

$$\sum_n \left(\left|a_n^{+}\right|^2 + \left|a_n^{-}\right|^2\right) = \sum_n \left(\left|b_n^{+}\right|^2 + \left|b_n^{-}\right|^2\right), \tag{6-33}$$

which we can recast in vector form as $|\mathbf{b}|^2 = |\mathbf{a}|^2$. As a result, we find that

$$\mathbf{a}^\dagger \check{S}^\dagger \check{S} \mathbf{a} = |\mathbf{a}|^2, \tag{6-34}$$

and thus,

$$\mathbf{a}^\dagger \left(\check{S}^\dagger \check{S} - 1 \right) \mathbf{a} = 0. \tag{6-35}$$

eq:appb2 proves that the scattering matrix is unitary, that is,

$$\check{S}^\dagger \check{S} = \check{S} \check{S}^\dagger = \check{1}, \tag{6-36}$$

which we can recast using the reflection matrix $\check{r}$ as

$$\left(1 + \check{r}_a\right) \left(1 + \check{r}_a^\dagger\right) = \left(1 + \check{r}_a^\dagger\right) \left(1 + \check{r}_a\right) = \check{1}. \tag{6-37}$$

6.1.4 Nanoribbon Green's function and bound states

The solution to 2-31 reads as

$$\check{G}_{ab}\left(x, x'\right) = \check{G}_a\left(x, x'\right) + \check{W}^<\left(x\right) \check{G}_a^>\left(x_b, x'\right), \tag{6-38}$$

with

$$\check{W}^<\left(x\right) = \sum_{n,m,\varepsilon,\varepsilon'} f_n^\varepsilon\left(x - x_b\right) \left(\hat{r}_b^{\varepsilon\varepsilon'}\right)_{nm} \check{P}_{nm}^{\varepsilon\varepsilon'}, \tag{6-39}$$

and

$$\check{r}_b = -i \frac{U_b \check{\tau}_b}{2\hbar v_F} \left(\check{1} + i \frac{U_b \check{\tau}_b}{2\hbar v_F} \right)^{-1}. \tag{6-40}$$

Using the explicit expression for the semi-infinite GF, 2-24, we write the GF with $x > x'$ for the central region as

$$\check{G}_{ab}^<\left(x, x'\right) = \frac{-i}{2\hbar v_F} \tag{6-41}$$
$$\times \sum_{n,m,\varepsilon,\varepsilon'} f_n^\varepsilon(x - x_b) (\check{w}^>)_{nm}^{\varepsilon\varepsilon'} f_m^{\varepsilon'}(x_b - x') \psi_n^\varepsilon (\bar{\psi}_m^{\varepsilon'})^T,$$

where we have defined the matrices

$$\check{w}^> = \begin{pmatrix} \hat{1} + \hat{w}_b^{++} & \left(\hat{1} + \hat{w}_b^{++}\right) \hat{r}_a^{+-}\left(L\right) \\ \hat{w}_b^{-+} & \hat{w}_b^{-+} \hat{r}_a^{+-}\left(L\right) \end{pmatrix}, \tag{6-42}$$

with $L = x_b - x_a > 0$ the length of the finite region. Here, $\hat{w}_b^{\varepsilon\varepsilon'}$ are the submatrix elements of

$$\check{w}_b = -i \frac{U_b}{2\hbar v_F} \check{\tau} \left(\check{1} + i \frac{U_b}{2\hbar v_F} \check{\tau} \right)^{-1}, \tag{6-43}$$

with

$$\check{\tau} = \begin{pmatrix} \hat{r}_a^{+-}(L)\,\hat{\tau}_b^{-+} & \hat{r}_a^{+-}(L)\,\hat{\tau}_b^{--} \\ \hat{\tau}_b^{-+} & \hat{\tau}_b^{--} \end{pmatrix}, \tag{6-44}$$

and $\hat{r}_a^{+-}(W)$ is defined from the reflection matrix at the left interface, $\hat{r}_a^{+-}$, as $\hat{r}_a^{+-}(W) = \hat{f}^{++}(-W)\hat{r}_a^{+-}\hat{f}^{--}(W)$, with the diagonal matrices $(\hat{f}^{\varepsilon\varepsilon})_{nm}(x) = \delta_{nm} f_m^{\varepsilon}(x)$. Analogously, we can also define

$$\check{w}^{<} = \begin{pmatrix} \hat{w}_b^{++} & \left(\hat{1} + \hat{w}_b^{++}\right)\hat{r}_a^{+-}(L) \\ \hat{w}_b^{-+} & \hat{1} + \hat{w}_b^{-+}\hat{r}_a^{+-}(L) \end{pmatrix}, \tag{6-45}$$

where we have used the projector operators, 6-3. This result is equivalent to the reflection matrix for a single barrier at $x = x_b$, $\hat{r}^{++}$, changing $\check{w}_b$ by $\hat{\tau}^{++}$.

In this section we provide more details on the derivation of the nanoribbon GF, 2-32, and the associated bound states. For the case of two potential barriers placed at $x = x_a$ and $x = x_b > x_a$, the perturbed GF for the region between the barriers is

$$\check{G}_{ab}(x, x') = \check{G}_a(x, x') + \check{W}^{<}(x)\,\check{G}_{ab}^{>}(x_b, x'), \tag{6-46}$$

for $x > x'$, where

$$\check{G}_{ab}^{>}(x, x') = \frac{-i}{2\hbar v_F} \tag{6-47}$$
$$\times \sum_{n,m,\varepsilon,\varepsilon'} f_n^{\varepsilon}(x - x_b)(\check{w}^{>})_{nm}^{\varepsilon\varepsilon'} f_m^{\varepsilon'}(x_b - x')\psi_n^{\varepsilon}(\bar{\psi}_m^{\varepsilon'})^T,$$

with $\check{w}^{>}$ given by 6-45.

The equation 6-46 can be solved after obtaining $\check{G}_{ab}^{>}$. However, to do so, one can not take the limit $U_b \to \infty$ and invert $\check{w}$, because the matrix $\check{\tau}$ has no inverse ($\det[\check{\tau}] = 0$). To circumvent this problem, we define the matrix

$$\check{N} = \hat{1} - AU_b\check{\tau}, \tag{6-48}$$

with $A = -i/(2\hbar v_F)$, and

$$\check{N} = \begin{pmatrix} \hat{N}_1 & \hat{N}_2 \\ \hat{N}_3 & \hat{N}_4 \end{pmatrix}, \tag{6-49}$$

where

$$\hat{N}_1 = \hat{1} - AU_b\hat{r}_a^{+-}(L)\,\hat{\tau}_b^{-+}, \qquad \hat{N}_2 = -AU_b\hat{r}_a^{+-}(L)\,\hat{\tau}_b^{--},$$
$$\hat{N}_3 = -AU_b\hat{\tau}_b^{-+}, \qquad \hat{N}_4 = AU_b\hat{\tau}_b^{-+}\left(\hat{r}_b^{-+}\right)^{-1}.$$

We can now compute the inverse of $\hat{N}$ and then take the limit $U_b \to \infty$. To do so, we use Schur complement, which, for example, is defined for submatrix $\hat{N}_4$ as

$$\hat{C} = \hat{N}_1 - \hat{N}_2 \hat{N}_4{}^{-1} \hat{N}_3.$$

Therefore, defining

$$\hat{r}_b^{-+} = A U_b \left(1 - A U_b^{--} \hat{\tau}_b\right)^{-1} \hat{\tau}_b^{-+},$$

we get

$$\hat{C} = \hat{1} - \hat{r}_a^{+-}(L)\, \hat{r}_b^{-+}, \tag{6-50}$$

with $L = x_b - x_a$.

The inverse matrix of $\hat{N}$ is thus

$$\check{N}^{-1} = \begin{pmatrix} \hat{1} & 0 \\ -\hat{N}_4^{-1}\hat{N}_3 & \hat{1} \end{pmatrix} \begin{pmatrix} \hat{C}^{-1} & 0 \\ 0 & \hat{N}_4^{-1} \end{pmatrix} \begin{pmatrix} \hat{1} & -\hat{N}_2\hat{N}_4^{-1} \\ 0 & \hat{1} \end{pmatrix}, \tag{6-51}$$

which simplifies to

$$\check{N}^{-1} = \begin{pmatrix} \hat{C}^{-1} & \hat{C}^{-1}\hat{r}_a^{+-}(L)\, \hat{\tau}_b^{--} \hat{r}_b^{-+} \left(\hat{\tau}_b^{-+}\right)^{-1} \\ \hat{r}_b^{-+}\hat{C}^{-1} & U_b^{-1}\hat{r}_b^{-+}\hat{C}^{-1}\left(\hat{1} - U_b \hat{r}_a^{+-}(L)\, \hat{\tau}_b^{-+}\right)\left(\hat{\tau}_b^{-+}\right)^{-1} \end{pmatrix}. \tag{6-52}$$

We can now take the limit $U_b \to \infty$, resulting in

$$\check{w}^{<} = \begin{pmatrix} \hat{C}^{-1}\hat{r}_a^{+-}(L)\, \hat{r}_b^{-+} & -\hat{C}^{-1}\hat{r}_a^{+-}(L) \\ \hat{r}_b^{-+}\hat{C}^{-1} & -\hat{r}_b^{-+}\hat{C}^{-1}\left(\hat{r}_b^{-+}\right)^{-1} \end{pmatrix}. \tag{6-53}$$

Analogously, we get

$$\check{w}^{>} = \begin{pmatrix} \hat{D}^{++} & \hat{D}^{++}\hat{r}_a^{+-}(x_a) \\ \hat{r}_b^{-+}(x_b)\, \hat{D}^{++} & \hat{r}_b^{-+}(x_b)\, \hat{D}^{++}\hat{r}_a^{+-}(x_a) \end{pmatrix}, \tag{6-54}$$

with

$$\hat{D}^{++} = \left[\hat{1} - \hat{r}_a^{+-}(x_a)\, \hat{r}_b^{-+}(x_b)\right]^{-1}, \tag{6-55}$$

$$\hat{D}^{--} = \left[\hat{1} - \hat{r}_b^{-+}(x_b)\, \hat{r}_a^{+-}(x_a)\right]^{-1}. \tag{6-56}$$

The nanoribbon's bound states are obtained from the denominator of the GF, that is, setting the inverse of $\hat{D}^{++}$ or, equivalently, $\hat{D}^{--}$, to zero. From 6-55, this condition reduces to

$$\hat{r}_a^{+-}(x_a)\, \hat{r}_b^{-+}(x_b) = \hat{1}. \tag{6-57}$$

We can interpret this condition as follows: inside the nanoribbon, the scattering state is a superposition of left and right movers, namely,

$$\psi = \sum_n \left(c_n^+ \psi_n^+ + c_n^- \psi_n^-\right). \tag{6-58}$$

At each potential barrier, $x = x_{a,b}$, the amplitudes for left and right movers, c_n^- and c_n^+, respectively, are related by

$$c_n^- = \sum_m \hat{r}_{nm}^{-+}(x_b)\, c_m^+, \tag{6-59}$$

$$c_n^+ = \sum_m \hat{r}_{nm}^{+-}(x_a)\, c_m^-. \tag{6-60}$$

In matrix form we have

$$\mathbf{c}^- = \hat{r}^{-+}(x_b)\, \mathbf{c}^+, \tag{6-61}$$

$$\mathbf{c}^+ = \hat{r}^{+-}(x_a)\, \mathbf{c}^-, \tag{6-62}$$

which form the closed cycle

$$\mathbf{c}^+ = \hat{r}^{+-}(x_a)\, \hat{r}^{-+}(x_b)\, \mathbf{c}^+. \tag{6-63}$$

It is thus straightforward to get

$$\mathbf{c}^+ \left(\hat{1} - \hat{r}^{+-}(x_a)\, \hat{r}^{-+}(x_b)\right) = \mathbf{0}, \tag{6-64}$$

which corresponds to the zeroes of the GF, as shown in 6-57. This result shows that the nanoribbon's bound states are determined by the reflection matrices at each edge of the finite region, and can thus be obtained by the zeroes of the inverse of 6-55.

6.1.5 Applications

General definition for zig-zag case: The normalized eigenstates:

$$\psi_1^+ = \frac{1}{\sqrt{2\cos\alpha}} \begin{pmatrix} N^{-1}e^{-i\frac{\alpha}{2}} \\ Ne^{i\frac{\alpha}{2}} \end{pmatrix} \tag{6-65}$$

$$\psi_1^- = \frac{1}{\sqrt{2\cos\alpha}} \begin{pmatrix} N^{-1}e^{i\frac{\alpha}{2}} \\ -Ne^{-i\frac{\alpha}{2}} \end{pmatrix} \tag{6-66}$$

$$\tilde{\psi}_1^+ = \frac{1}{\sqrt{2\cos\alpha}} \begin{pmatrix} Ne^{i\frac{\alpha}{2}} \\ N^{-1}e^{-i\frac{\alpha}{2}} \end{pmatrix} \tag{6-67}$$

$$\tilde{\psi}_1^- = \frac{1}{\sqrt{2\cos\alpha}} \begin{pmatrix} Ne^{i\frac{-\alpha}{2}} \\ -N^{-1}e^{i\frac{\alpha}{2}} \end{pmatrix} \tag{6-68}$$

Then we can define the transposed states which are

$$\bar{\psi}_1^+ = \frac{1}{\sqrt{2\cos\alpha}} \begin{pmatrix} N^{-1}e^{i\frac{\alpha}{2}} \\ Ne^{-i\frac{\alpha}{2}} \end{pmatrix} \tag{6-69}$$

$$\bar{\psi}_1^- = \frac{1}{\sqrt{2\cos\alpha}} \begin{pmatrix} N^{-1}e^{-i\frac{\alpha}{2}} \\ -Ne^{i\frac{\alpha}{2}} \end{pmatrix} \tag{6-70}$$

Finally with this we can calculate the bulk gf:

$$g^{<}(x,x') = \frac{e^{ik(x'-x)}}{2\cos\alpha}\begin{pmatrix} N^{-2} & -e^{i\alpha} \\ -e^{-i\alpha} & N^{2} \end{pmatrix} \tag{6-71}$$

$$g^{>}(x,x') = \frac{e^{ik(x-x')}}{2\cos\alpha}\begin{pmatrix} N^{-2} & e^{-i\alpha} \\ e^{i\alpha} & N^{2} \end{pmatrix} \tag{6-72}$$

Semi-infinite layer with zig-zag edge: The projections of $\hat{\tau}$ into the system eigenstates for border A is done as follows:

$$\hat{S}_{11}^{++} = \hat{S}_{11}^{--} = \frac{1}{2N^2\cos\alpha} \tag{6-73a}$$

$$\hat{S}_{11}^{+-} = \frac{e^{i\alpha}}{2N^2\cos\alpha} \tag{6-73b}$$

$$\hat{S}_{11}^{-+} = \frac{e^{-i\alpha}}{2N^2\cos\alpha} \tag{6-73c}$$

similarly is done for border B.

Regarding the outcome of the previous procedure it is easy to calculate the respective coefficients for the gf, which has the following form:

$$\hat{G}_{RR}(x,x') = \hat{g}(x,x') - e^{i\alpha}e^{ik(x+x'-2x_0)}\hat{M}_{11}^{+-} \tag{6-74}$$

Where,

$$\hat{M}_{nm}^{\epsilon\epsilon'} = \psi_n^{\epsilon}(\bar{\psi}_n^{\epsilon'})^T \tag{6-75}$$

$$\hat{G}_{RR}^{>}(x,x') = \frac{Ae^{ik(x-x')}}{2\cos\alpha}\begin{pmatrix} N^{-2} & e^{-i\alpha} \\ e^{i\alpha} & N^{2} \end{pmatrix} - \frac{Ae^{i\alpha}e^{ik(x+x'-2x_a)}}{2\cos\alpha}\begin{pmatrix} N^{-2}e^{-i\alpha} & -1 \\ 1 & -N^{2}e^{i\alpha} \end{pmatrix} \tag{6-76}$$

Then in the edge we can find

$$\hat{G}_{RR}^{>}(x_a,x_a) = -\frac{i}{\hbar v_F}\begin{pmatrix} 0 & 1 \\ 0 & N^{2}e^{i\alpha} \end{pmatrix} \tag{6-77}$$

Where easily can be observed the result of LDOS for the semi-infinite layer with zig-zag edges.
Nanoribbon layer with zig-zag edge:

A contracted form for the Green function in this case is,

$$\hat{G}^{>}_{ab}(x,x') = AD^{++}\left(e^{ikx}\psi^{+} + r^{-+}e^{-ik(x-2x_b)}\psi^{-}\right)\times \left(e^{-ikx'}\psi^{+\dagger} + r^{+-}e^{ik(x'-2x_a)}\psi^{-\dagger}\right) \tag{6-78}$$

Where D^{++}

$$D^{++} = \left[1 - r^{+-}r^{-+}e^{2ik(x_b-x_a)}\right]^{-1}$$

Finally we are able to operate to find the gf matrix:

$$\hat{G}^{>}_{ab}(x_a,x_a) \;=\; -i\begin{pmatrix} 0 & \frac{1+e^{2i\alpha}e^{i2kW}}{\hbar v_F\left[1+e^{+2i\alpha}e^{2ikW}\right]} \\ 0 & \frac{N^2e^{i\alpha}\left(1-e^{i2kW}\right)}{\hbar v_F\left[1+e^{+2i\alpha}e^{2ikW}\right]} \end{pmatrix}$$

General Definitions for Armchair case: Particularly for this case we find that the normalized eigenfunctions projected into each valley space are:

$$\varphi^{+}_{1} = \frac{1}{\sqrt{2\cos\alpha}}\begin{pmatrix} N^{-1}e^{-i\frac{\alpha}{2}} \\ Ne^{i\frac{\alpha}{2}} \end{pmatrix}, \tag{6-79}$$

$$\varphi^{-}_{1} = \frac{1}{\sqrt{2\cos\alpha}}\begin{pmatrix} N^{-1}e^{i\frac{\alpha}{2}} \\ -Ne^{-i\frac{\alpha}{2}} \end{pmatrix} \tag{6-80}$$

$$\varphi^{+}_{1'} = \frac{1}{\sqrt{2\cos\alpha'}}\begin{pmatrix} N'^{-1}e^{i\frac{\alpha'}{2}} \\ -N'e^{-i\frac{\alpha'}{2}} \end{pmatrix}, \tag{6-81}$$

$$\varphi^{-}_{1'} = \frac{1}{\sqrt{2\cos\alpha'}}\begin{pmatrix} N'^{-1}e^{-i\frac{\alpha'}{2}} \\ N'e^{i\frac{\alpha'}{2}} \end{pmatrix} \tag{6-82}$$

$$\tilde{\varphi}^{-}_{1'} = \frac{1}{\sqrt{2\cos\alpha'}}\begin{pmatrix} N'e^{i\frac{\alpha'}{2}} \\ N'^{-1}e^{-i\frac{\alpha'}{2}} \end{pmatrix} \tag{6-83}$$

and $\tilde{\varphi}^{\epsilon}_{n} = \hat{\sigma}_x\varphi^{\epsilon}_{n}$

Semi-infinite for armchair Previously was shown the matrix coefficients for the semi-infinite armchair layer, could be written compactly in the edge as:

$$\hat{G}^{<}_{RR}(x_0,x_0) = \left(\psi^{-}_{1} + r^{+-}_{11}\psi^{+}_{1} + r^{+-}_{1'1}\psi^{+}_{1'}\right)\psi^{-\dagger}_{1} + \left(\psi^{-}_{1'} + r^{+-}_{1'1'}\psi^{+}_{1'} + r^{+-}_{11'}\psi^{+}_{1}\right)\psi^{-\dagger}_{1'} \tag{6-84}$$

Coefficients such as $r^{+-}_{1'1'}$ could be defined in terms of auxiliary quantities, for instance in this specific case we have $r^{+-}_{1'1'} = \frac{h^{++}_{1'1}}{h^{-+}_{1'1}}$. Motivated by this several definitions for $h^{\epsilon\epsilon'}_{nm}$ are shown:

$$h^{++}_{11'} = \tilde{\varphi}^{+\dagger}_1 \varphi^+_{1'} \tag{6-85}$$
$$= \frac{e^{i\frac{(\alpha'-\alpha)}{2}}}{2\sqrt{\cos\alpha\cos\alpha'}}\left(\frac{N}{N'} - \frac{N'}{N}e^{-i(\alpha'-\alpha)}\right)$$

$$h^{-+}_{1'1} = h^{-+}_{11'} = \tag{6-86}$$
$$\frac{e^{i\frac{(\alpha'+\alpha)}{2}}}{2\sqrt{\cos\alpha'\cos\alpha}}\left(\frac{N}{N'} + \frac{N'}{N}e^{-i(\alpha'+\alpha)}\right)$$

$$h^{++}_{1'1} = \frac{e^{i\frac{(\alpha'-\alpha)}{2}}}{2\sqrt{\cos\alpha\cos\alpha'}}\left(\frac{N'}{N} - \frac{N}{N'}e^{-i(\alpha'-\alpha)}\right) \tag{6-87}$$

with this in mind we are able to find the reflection coefficients:

$$r^{+-}_{11} = e^{i\alpha}\frac{N^2e^{-i\alpha} - N'^2e^{-i\alpha'}}{N^2e^{i\alpha} + N'^2e^{-i\alpha'}} \tag{6-88}$$

$$r^{+-}_{1'1} = -2\frac{NN'\sqrt{\cos\alpha\cos\alpha'}}{N^2e^{i\alpha} + N'^2e^{-i\alpha'}}e^{i\frac{\alpha-\alpha'}{2}} \tag{6-89}$$

$$r^{+-}_{11'} = -2\frac{NN'\sqrt{\cos\alpha'\cos\alpha}}{N'^2e^{-i\alpha'} + N^2e^{i\alpha}}e^{i\frac{\alpha-\alpha'}{2}} \tag{6-90}$$

$$r^{+-}_{1'1'} = e^{i\alpha'}\frac{N'^2 - N^2e^{-i(\alpha'-\alpha)}}{N'^2 + N^2e^{i(\alpha'+\alpha)}} \tag{6-91}$$

Nanoribbon Armchair Layer As an illustration in this case we show the diagonal elements of the gf matrix

$$G^{>}_{KK'}(x,x') = \hat{f}^{+-}_{11'}(x,x')\,\hat{r}^{>,+-}_{11'}\hat{M}^{+-}_{11'} + \tag{6-92}$$
$$\hat{f}^{-+}_{11'}(x,x')\,\hat{r}^{>,-+}_{11'}\hat{M}^{-+}_{11'} + \hat{f}^{++}_{11'}(x,x')\,\hat{r}^{>,++}_{11'}\hat{M}^{++}_{11'}$$
$$+\hat{f}^{--}_{11'}(x,x')\,\hat{r}^{>,--}_{11'}\hat{M}^{--}_{11'}$$

$$G^{>}_{K'K'}(x,x') = \hat{f}^{++}_{1'1'}(x,x')\,\hat{r}^{>,++}_{1'1'}\hat{M}^{++}_{1'1'} + \hat{f}^{--}_{1'1'}(x,x')\,\hat{r}^{>,--}_{1'1'}\hat{M}^{--}_{1'1'} + \hat{f}^{+-}_{1'1'}(x,x')\,\hat{r}^{>,+-}_{1'1'}\hat{M}^{+-}_{1'1'} + \hat{f}^{-+}_{1'1'}(x,x')\,\hat{r}^{>,-+}_{1'1'}\hat{M}^{-+}_{1'1'} \tag{6-93}$$

Here $f^{\varepsilon\varepsilon'}_{nm}(x,x') = f^{\varepsilon}_{n}(x) f^{\epsilon'}_{m}(x')$, where $f^{\varepsilon}_{n}(x) = e^{i(K+\varepsilon k_n)x}$. Also, each coefficient is described by the reflection coefficient matrices which define $r^{>}_{\alpha\beta}$. Each entry of this matrix depends on the following matrixes:

$$\hat{r}^{+-}_{a}(x_a) = \begin{pmatrix} \frac{h_{11'}}{h_{\bar{1}1'}} e^{-2ikx_a} & -\frac{1}{h_{\bar{1}'1}} e^{-i(2K+k+k')x_a} \\ -\frac{1}{h_{\bar{1}1'}} e^{i(2K-k-k')x_a} & \frac{h_{1'1}}{h_{\bar{1}'1}} e^{-2ik'x_a} \end{pmatrix}$$

$$\hat{r}^{-+}_{b}(x_b) = \begin{pmatrix} \frac{h^{--}_{11'}}{h^{+-}_{11'}} e^{2ikx_b} & -\frac{1}{h^{+-}_{1'1}} e^{i(-2K+k+k')x_b} \\ -\frac{1}{h^{+-}_{11'}} e^{i(2K+k'+k)x_b} & \frac{h^{--}_{1'1}}{h^{+-}_{1'1}} e^{2ik'x_b} \end{pmatrix}$$

6.2 All-Optical and micro-wave free Low Field Magnetometer based on NV center in diamond

6.2.1 Rotation Matrix

$$R(\phi,\theta,\lambda) = \begin{pmatrix} \cos(\phi)\cos(\theta)\cos(\lambda) - \sin(\phi)\sin(\lambda) & \cos(\phi)\cos(\theta)\cos(\lambda) + \sin(\phi)\sin(\lambda) & -\cos(\phi)\sin(\theta) \\ -\sin(\phi)\cos(\theta)\cos(\lambda) - \cos(\phi)\sin(\lambda) & -\sin(\phi)\cos(\theta)\cos(\lambda) + \cos(\phi)\cos(\lambda) & \sin(\phi)\sin(\theta) \\ \sin(\theta)\cos(\lambda) & \sin(\theta)\sin(\lambda) & \cos(\theta) \end{pmatrix} \tag{6-94}$$

7 Bibliography

[1] Natalie Wolchover. Physicists aim to classify all possible phases of matter, Jan 2019.

[2] Bogdan Andrei Bernevig, Taylor L. Hughes, and Shou-Cheng Zhang. Quantum spin hall effect and topological phase transition in hgte quantum wells. *Science*, 314:1757 – 1761, 2006.

[3] Markus König, Steffen Wiedmann, Christoph Brüne, Andreas Roth, Hartmut Buhmann, Laurens W. Molenkamp, Xiao-Liang Qi, and Shou-Cheng Zhang. Quantum spin hall insulator state in hgte quantum wells. *Science*, 318:766 – 770, 2007.

[4] Xiaofeng Qian, Junwei Liu, Liang Fu, and Ju Li. Quantum spin hall effect and topological field effect transistor in two-dimensional transition metal dichalcogenides. *Science*, 2014.

[5] Sanfeng Wu, Valla Fatemi, Quinn D. Gibson, Kenji Watanabe, Takashi Taniguchi, Robert J. Cava, and Pablo Jarillo-Herrero. Observation of the quantum spin hall effect up to 100 kelvin in a monolayer crystal. *Science*, 359:76 – 79, 2017.

[6] Xiao-Liang Qi and Shou-Cheng Zhang. The quantum spin hall effect and topological insulators. *Physics Today*, 63:33–38, 2010.

[7] Yuqi Xia, Dong Qian, David Hsieh, L. Andrew Wray, Arijeet Pal, Hsin Lin, Arun Bansil, David C Grauer, Yew San Hor, Robert J. Cava, and M Zahid Hasan. Observation of a large-gap topological-insulator class with a single dirac cone on the surface. *Nature Physics*, 5:398–402, 2009.

[8] David Hsieh, Dong Qian, L. Andrew Wray, Y. Y. Xia, Yew San Hor, Robert J. Cava, and M Zahid Hasan. A topological dirac insulator in a quantum spin hall phase. *Nature*, 452:970–974, 2008.

[9] Y. L. Chen, James G. Analytis, J. H. Chu, Z. K. Liu, S. K. Mo, Xiao-Liang Qi, H. J. Zhang, Donghui Lu, Xi Dai, Zhong Fang, S. C. Zhang, Ian R. Fisher, Zahid Hussain, and Z. X. Shen. Experimental realization of a three-dimensional topological insulator, bi2te3. *Science*, 325:178 – 181, 2009.

[10] Alex R. Mellnik, J. S. Lee, Anthony Richardella, Jennifer L. Grab, Peter J. Mintun, Mark H. Fischer, Abolhassan Vaezi, Aurélien Manchon, E.-A. Kim, Nitin Samarth, and Daniel C.

Ralph. Spin-transfer torque generated by a topological insulator. *Nature*, 511:449–451, 2014.

[11] Yabin Fan, Pramey Upadhyaya, Xufeng Kou, Murong Lang, So Takei, Zhenxing Wang, Jianshi Tang, Liang He, Li-Te Chang, Mohammad Montazeri, Guoqiang Yu, Wanjun Jiang, Tianxiao Nie, Robert N. Schwartz, Yaroslav Tserkovnyak, and Kang L. Wang. Magnetization switching through giant spin-orbit torque in a magnetically doped topological insulator heterostructure. *Nature materials*, 13 7:699–704, 2014.

[12] Charles L. Kane and Eugene J. Mele. Quantum spin hall effect in graphene. *Physical review letters*, 95 22:226801, 2004.

[13] Motohiko Ezawa. Monolayer topological insulators: Silicene, germanene, and stanene. *Journal of the Physical Society of Japan*, 84:121003, 2015.

[14] Masatoshi Sato and Yoichi Ando. Topological superconductors: a review. *Reports on Progress in Physics*, 80, 2016.

[15] Liang Fu and Charles L. Kane. Superconducting proximity effect and majorana fermions at the surface of a topological insulator. *Physical review letters*, 100 9:096407, 2007.

[16] Qing Lin He, Lei Pan, Alex Stern, Edward C. Burks, Xiaoyu Che, Gen Yin, Jing Wang, Biao Lian, Quan Zhou, Eun Sang Choi, Koichi Murata, Xufeng Kou, Zhijie Chen, Tianxiao Nie, Qiming Shao, Yabin Fan, Shou-Cheng Zhang, Kai Liu, Jing Xia, and Kang L. Wang. Chiral majorana fermion modes in a quantum anomalous hall insulator–superconductor structure. *Science*, 357:294 – 299, 2016.

[17] A. Fornieri, A. M. Whiticar, F. Setiawan, Elías Portolés, A. C. C. Drachmann, Anna Keselman, Sergei Gronin, Candice Thomas, Tian Wang, Raymond L. Kallaher, Geoff C. Gardner, Erez Berg, Michael J. Manfra, Ady Stern, Charles M. Marcus, and Fabrizio Nichele. Evidence of topological superconductivity in planar josephson junctions. *Nature*, 569:89–92, 2018.

[18] P. Zhang, Koichiro Yaji, Takahiro Hashimoto, Yuichi Ota, Takeshi Kondo, Kozo Okazaki, Zhijun Wang, Jinsheng Wen, Genda Gu, Hong Ding, and Shik Shin. Observation of topological superconductivity on the surface of an iron-based superconductor. *Science*, 360:182 – 186, 2017.

[19] Elsa Prada, Pablo San-Jose, Michiel W. A. de Moor, Attila Geresdi, Eduardo J H Lee, Jelena Klinovaja, Daniel Loss, Jesper Nygård, Ramón Aguado, and Leo P Kouwenhoven. From andreev to majorana bound states in hybrid superconductor–semiconductor nanowires. *Nature Reviews Physics*, pages 1–20, 2019.

[20] Dmitry I. Pikulin, Bernard van Heck, Torsten Karzig, Esteban A. Martinez, Bas Nijholt, Tom Laeven, G. W. Winkler, John D. Watson, Sebastian Heedt, M. Temurhan, V. Svidenko, R. M. Lutchyn, Mason Thomas, Gijs de Lange, L. Casparis, and C. Nayak. Protocol to identify a topological superconducting phase in a three-terminal device. 2021.

[21] Cenke Xu and Leon Balents. Topological superconductivity in twisted multilayer graphene. *Physical review letters*, 121 8:087001, 2018.

[22] Yi-Ting Hsu, Abolhassan Vaezi, Mark H. Fischer, and Eun-Ah Kim. Topological superconductivity in monolayer transition metal dichalcogenides. *Nature Communications*, 8, 2016.

[23] Natalie Wolchover. Forging a qubit to rule them all, Apr 2019.

[24] Yoshinori Tokura and Naoya Kanazawa. Magnetic skyrmion materials. *Chemical reviews*, 2020.

[25] Lucas Thiel, Z. Wang, M. A. Tschudin, Dominik Rohner, Ignacio Gutiérrez-Lezama, Nicolas Ubrig, Marco Gibertini, Enrico Giannini, Alberto F. Morpurgo, and Patrick Maletinsky. Probing magnetism in 2d materials at the nanoscale with single-spin microscopy. *Science*, 364:973 – 976, 2019.

[26] Sebastian Mühlbauer, Benedikt Binz, Florian Jonietz, Christian Pfleiderer, Achim Rosch, Andreas Neubauer, Robert Georgii, and Peter Böni. Skyrmion lattice in a chiral magnet. *Science*, 323:915 – 919, 2009.

[27] E. C. Marino. Quantum field theory approach to condensed matter physics. 2017.

[28] Gerald Rickayzen. Green's functions and condensed matter. 1981.

[29] William J. Herrera, Pablo Burset, and Alfredo Levy Yeyati. A green function approach to graphene–superconductor junctions with well-defined edges. *Journal of Physics: Condensed Matter*, 22:275304, 2010.

[30] Oscar E. Casas, Shirley Gómez Páez, and William J. Herrera. A green's function approach to topological insulator junctions with magnetic and superconducting regions. *Journal of Physics: Condensed Matter*, 32, 2020.

[31] F. Fabre, Aurore Finco, Anike Purbawati, Abdellali Hadj-Azzem, Nicolas Rougemaille, Johann Coraux, I. Philip, and Vincent Jacques. Characterization of room-temperature in-plane magnetization in thin flakes of crte2 with a single-spin magnetometer. *arXiv: Materials Science*, 2020.

[32] Mark J. H. Ku, Tony X. Zhou, Qing Li, Young Jae Shin, Jingcheng Shi, Claire Burch, Laurel E. Anderson, Andrew T. Pierce, Yonglong Xie, A. Hamo, Uri Vool, Huiliang Zhang, Francesco Casola, Takashi Taniguchi, Kenji Watanabe, Michael M. Fogler, Philip Kim, Amir Yacoby,

and Ronald L. Walsworth. Imaging viscous flow of the dirac fluid in graphene. *Nature*, 583:537 – 541, 2019.

[33] Yuliya Dovzhenko, Francesco Casola, Sarah Schlotter, Tony X. Zhou, Felix Büttner, Ronald L. Walsworth, Geoffrey S. D. Beach, and Amir Yacoby. Magnetostatic twists in room-temperature skyrmions explored by nitrogen-vacancy center spin texture reconstruction. *Nature Communications*, 9, 2018.

[34] Edlyn V. Levine, Matthew J. Turner, Pauli Kehayias, Connor A Hart, Nicholas Langellier, Raisa Trubko, David R. Glenn, Roger R. Fu, and Ronald L. Walsworth. Principles and techniques of the quantum diamond microscope. *Nanophotonics*, 8:1945 – 1973, 2019.

[35] Tim Oliver Wehling, Annica M. Black□Schaffer, and Alexander V. Balatsky. Dirac materials. *Advances in Physics*, 63, May 2014.

[36] Jérôme Cayssol. Introduction to Dirac materials and topological insulators. *C. R. Phys.*, 14(9):760–778, November 2013.

[37] Mingsheng Xu, Tao Liang, Minmin Shi, and Hongzheng Chen. Graphene-Like Two-Dimensional Materials. *Chem. Rev.*, 113(5):3766–3798, May 2013.

[38] Jinying Wang, Shibin Deng, Zhongfan Liu, and Zhirong Liu. The rare two-dimensional materials with Dirac cones. *National Science Review*, 2(1):22–39, 01 2015.

[39] Chaoliang Tan, Xiehong Cao, Xue-Jun Wu, Qiyuan He, Jian Yang, Xiao Zhang, Junze Chen, Wei Zhao, Shikui Han, Gwang-Hyeon Nam, Melinda Sindoro, and Hua Zhang. Recent Advances in Ultrathin Two-Dimensional Nanomaterials. *Chem. Rev.*, 117(9):6225–6331, May 2017.

[40] Markus König, Steffen Wiedmann, Christoph Brüne, Andreas Roth, Hartmut Buhmann, Laurens W. Molenkamp, Xiao-Liang Qi, and Shou-Cheng Zhang. Quantum Spin Hall Insulator State in HgTe Quantum Wells. *Science*, 318(5851):766–770, 2007.

[41] Ivan Knez, Rui-Rui Du, and Gerard Sullivan. Evidence for Helical Edge Modes in Inverted InAs/GaSb Quantum Wells. *Phys. Rev. Lett.*, 107:136603, Sep 2011.

[42] M. Z. Hasan and C. L. Kane. Colloquium: Topological insulators. *Rev. Mod. Phys.*, 82:3045–3067, Nov 2010.

[43] Liangzhi Kou, Yandong Ma, Ziqi Sun, Thomas Heine, and Changfeng Chen. Two-Dimensional Topological Insulators: Progress and Prospects. *J. Phys. Chem. Lett.*, 8(8):1905–1919, April 2017.

[44] A Acun, L Zhang, P Bampoulis, M Farmanbar, A van Houselt, A N Rudenko, M Lingenfelder, G Brocks, B Poelsema, M I Katsnelson, and H J W Zandvliet. Germanene: the germanium analogue of graphene. *Journal of Physics: Condensed Matter*, 27(44):443002, oct 2015.

[45] C. Kamal and Motohiko Ezawa. Arsenene: Two-dimensional buckled and puckered honeycomb arsenic systems. *Phys. Rev. B*, 91:085423, Feb 2015.

[46] Suman Chowdhury and Debnarayan Jana. A theoretical review on electronic, magnetic and optical properties of silicene. *Reports on Progress in Physics*, 79(12):126501, oct 2016.

[47] Sajedeh Manzeli, Dmitry Ovchinnikov, Diego Pasquier, Oleg V. Yazyev, and Andras Kis. 2D transition metal dichalcogenides. *Nature Reviews Materials*, 2(8):17033, August 2017.

[48] Barry Bradlyn, L. Elcoro, Jennifer Cano, M. G. Vergniory, Zhijun Wang, C. Felser, M. I. Aroyo, and B. Andrei Bernevig. Topological quantum chemistry. *Nature*, 547:298–305, July 2017.

[49] L. Brey and H. A. Fertig. Electronic states of graphene nanoribbons studied with the dirac equation. *Phys. Rev. B*, 73:235411, Jun 2006.

[50] Jürgen Wurm, Klaus Richter, and İnan ç Adagideli. Edge effects in graphene nanostructures: From multiple reflection expansion to density of states. *Phys. Rev. B*, 84:075468, Aug 2011.

[51] Diego A. Manjarrés, William J. Herrera, and Shirley Gómez. Andreev levels in a graphene–superconductor surface. *Physica B: Condensed Matter*, 404(18):2799–2801, 2009.

[52] William J Herrera, P Burset, and A Levy Yeyati. A green function approach to graphene–superconductor junctions with well-defined edges. *Journal of Physics: Condensed Matter*, 22(27):275304, jun 2010.

[53] P. Burset, W. Herrera, and A. Levy Yeyati. Proximity-induced interface bound states in superconductor-graphene junctions. *Phys. Rev. B*, 80:041402, Jul 2009.

[54] Shirley Gómez Páez, Camilo Martínez, William J. Herrera, Alfredo Levy Yeyati, and Pablo Burset. Dirac point formation revealed by andreev tunneling in superlattice-graphene/superconductor junctions. *Phys. Rev. B*, 100:205429, Nov 2019.

[55] Oscar E Casas, Shirley Gómez Páez, and William J Herrera. A green's function approach to topological insulator junctions with magnetic and superconducting regions. *Journal of Physics: Condensed Matter*, 32(48):485302, sep 2020.

[56] C. L. Kane and E. J. Mele. Quantum spin hall effect in graphene. *Phys. Rev. Lett.*, 95:226801, Nov 2005.

[57] Motohiko Ezawa. A topological insulator and helical zero mode in silicene under an inhomogeneous electric field. *New Journal of Physics*, 14(3):033003, mar 2012.

[58] Cheng Cheng Liu, Wanxiang Feng, and Yugui Yao. Quantum spin hall effect in silicene and two-dimensional germanium. *Phys. Rev. Lett.*, 107:076802, Aug 2011.

[59] J. H. N. Loubser and J. A. van Wyk. Electron spin resonance in the study of diamond. *Rep. Prog. Phys.*, 41(8):1201, August 1978.

[60] Mingsheng Xu, Tao Liang, Minmin Shi, and Hongzheng Chen. Graphene-Like Two-Dimensional Materials. *Chem. Rev.*, 113(5):3766–3798, May 2013.

[61] Sajedeh Manzeli, Dmitry Ovchinnikov, Diego Pasquier, Oleg V. Yazyev, and Andras Kis. 2D transition metal dichalcogenides. *Nat. Rev. Mater.*, 2(17033):1–15, June 2017.

[62] Wonbong Choi, Nitin Choudhary, Gang Hee Han, Juhong Park, Deji Akinwande, and Young Hee Lee. Recent development of two-dimensional transition metal dichalcogenides and their applications. *Mater. Today*, 20(3):116–130, April 2017.

[63] Deep Jariwala, Vinod K. Sangwan, Lincoln J. Lauhon, Tobin J. Marks, and Mark C. Hersam. Emerging Device Applications for Semiconducting Two-Dimensional Transition Metal Dichalcogenides. *ACS Nano*, 8(2):1102–1120, February 2014.

[64] Motohiko Ezawa. Monolayer topological insulators: Silicene, germanene, and stanene. *Journal of the Physical Society of Japan*, 84(12):121003, 2015.

[65] A. Acun, L. Zhang, P. Bampoulis, M. Farmanbar, A. van Houselt, A. N. Rudenko, M. Lingenfelder, G. Brocks, B. Poelsema, M. I. Katsnelson, and H. J. W. Zandvliet. Germanene: the germanium analogue of graphene. *J. Phys.: Condens. Matter*, 27(44):443002, October 2015.

[66] M. E. Dávila, L. Xian, S. Cahangirov, A. Rubio, and G. Le Lay. Germanene: a novel two-dimensional germanium allotrope akin to graphene and silicene. *New J. Phys.*, 16(9):095002, September 2014.

[67] María Eugenia Dávila and Guy Le Lay. Few layer epitaxial germanene: a novel two-dimensional Dirac material. *Sci. Rep.*, 6(20714):1–9, February 2016.

[68] Patrick Vogt, Paola De Padova, Claudio Quaresima, Jose Avila, Emmanouil Frantzeskakis, Maria Carmen Asensio, Andrea Resta, Bénédicte Ealet, and Guy Le Lay. Silicene: Compelling Experimental Evidence for Graphenelike Two-Dimensional Silicon. *Phys. Rev. Lett.*, 108(15):155501, April 2012.

[69] Deep Jariwala, Vinod K. Sangwan, Lincoln J. Lauhon, Tobin J. Marks, and Mark C. Hersam. Emerging Device Applications for Semiconducting Two-Dimensional Transition Metal Dichalcogenides. *ACS Nano*, 8(2):1102–1120, February 2014.

[70] Andor Kormányos, Guido Burkard, Martin Gmitra, Jaroslav Fabian, Viktor Zólyomi, Neil D. Drummond, and Vladimir Fal'ko. k·p theory for two-dimensional transition metal dichalcogenide semiconductors. *2D Mater.*, 2(2):022001, April 2015.

[71] A. K. Geim and K. S. Novoselov. The rise of graphene. *Nat. Mater.*, 6(3):183–191, March 2007.

[72] A. K. Geim. Graphene: Status and Prospects. *Science*, 324(5934):1530–1534, June 2009.

[73] K. S. Novoselov, V. I. Fal'ko, L. Colombo, P. R. Gellert, M. G. Schwab, and K. Kim. A roadmap for graphene. *Nature*, 490(7419):192–200, October 2012.

[74] Jannik C. Meyer, A. K. Geim, M. I. Katsnelson, K. S. Novoselov, T. J. Booth, and S. Roth. The structure of suspended graphene sheets. *Nature*, 446(7131):60–63, March 2007.

[75] Ruitao Lv, Joshua A. Robinson, Raymond E. Schaak, Du Sun, Yifan Sun, Thomas E. Mallouk, and Mauricio Terrones. Transition Metal Dichalcogenides and Beyond: Synthesis, Properties, and Applications of Single- and Few-Layer Nanosheets. *Acc. Chem. Res.*, 48(1):56–64, January 2015.

[76] Cheng-Cheng Liu, Wanxiang Feng, and Yugui Yao. Quantum Spin Hall Effect in Silicene and Two-Dimensional Germanium. *Phys. Rev. Lett.*, 107(7):076802, August 2011.

[77] Li Tao, Eugenio Cinquanta, Daniele Chiappe, Carlo Grazianetti, Marco Fanciulli, Madan Dubey, Alessandro Molle, and Deji Akinwande. Silicene field-effect transistors operating at room temperature. *Nat. Nanotechnol.*, 10(3):227–231, March 2015.

[78] Jijun Zhao, Hongsheng Liu, Zhiming Yu, Ruge Quhe, Si Zhou, Yangyang Wang, Cheng Cheng Liu, Hongxia Zhong, Nannan Han, Jing Lu, Yugui Yao, and Kehui Wu. Rise of silicene: A competitive 2D material. *Prog. Mater. Sci.*, 83:24–151, October 2016.

[79] Di Xiao, Gui-Bin Liu, Wanxiang Feng, Xiaodong Xu, and Wang Yao. Coupled Spin and Valley Physics in Monolayers of MoS_2 and Other Group-VI Dichalcogenides. *Phys. Rev. Lett.*, 108(19):196802, May 2012.

[80] Motohiko Ezawa. Monolayer Topological Insulators: Silicene, Germanene, and Stanene. *J. Phys. Soc. Jpn.*, 84(12):121003, October 2015.

[81] Wei-Tao Lu and Qing-Feng Sun. Electrical control of crossed andreev reflection and spin-valley switch in antiferromagnet/superconductor junctions. *Phys. Rev. B*, 104:045418, Jul 2021.

[82] Jingang Wang, Fengcai Ma, and Mengtao Sun. Graphene, hexagonal boron nitride, and their heterostructures: properties and applications. *RSC Adv.*, 7(27):16801–16822, March 2017.

[83] Archana Raja, Andrey Chaves, Jaeeun Yu, Ghidewon Arefe, Heather M. Hill, Albert F. Rigosi, Timothy C. Berkelbach, Philipp Nagler, Christian Schüller, Tobias Korn, Colin Nuckolls, James Hone, Louis E. Brus, Tony F. Heinz, David R. Reichman, and Alexey Chernikov. Coulomb engineering of the bandgap and excitons in two-dimensional materials. *Nat. Commun.*, 8(15251):1–7, May 2017.

[84] A. Chaves, J. G. Azadani, Hussain Alsalman, D. R. da Costa, R. Frisenda, A. J. Chaves, Seung Hyun Song, Y. D. Kim, Daowei He, Jiadong Zhou, A. Castellanos-Gomez, F. M. Peeters, Zheng Liu, C. L. Hinkle, Sang-Hyun Oh, Peide D. Ye, Steven J. Koester, Young Hee Lee, Ph. Avouris, Xinran Wang, and Tony Low. Bandgap engineering of two-dimensional semiconductor materials. *npj 2D Mater. Appl.*, 4(29):1–21, August 2020.

[85] Andrew F. May, Dmitry Ovchinnikov, Qiang Zheng, Raphael P. Hermann, Stuart Calder, Bevin Huang, Zaiyao Fei, Yaohua Liu, Xiaodong Xu, and Michael A. McGuire. Ferromagnetism near room temperature in the cleavable van der waals crystal fe5gete2. *ACS nano*, 13 4:4436–4442, 2019.

[86] Zheng Li, Wei Xia, Hao Su, Zhenhai Yu, Yunpeng Fu, Leiming Chen, Xia Wang, Na Yu, Zhiqiang Zou, and Yanfeng Guo. Magnetic critical behavior of the van der waals fe5gete2 crystal with near room temperature ferromagnetism. *Scientific Reports*, 10, 2020.

[87] Tomoharu Ohta, Masashi Tokuda, Shuichi Iwakiri, Kosuke Sakai, Benjamin Driesen, Yoshinori Okada, Kensuke Kobayashi, and Yasuhiro Niimi. Butterfly-shaped magnetoresistance in van der waals ferromagnet fe5gete2. *AIP Advances*, 11:025014, 2021.

[88] Xiang Chen, Enrico Schierle, Yu He, Mayia Vranas, John W. Freeland, Jessica L. McChesney, Ramamoorthy Ramesh, Robert J. Birgeneau, and Alex Frano. Antiferromagnetic order in co-doped fe$_5$gete$_2$ probed by resonant magnetic x-ray scattering. 2022.

[89] Congkuan Tian, Feihao Pan, Sheng Xu, Kun Ai, Tianlong Xia, and Peng Cheng. Tunable magnetic properties in van der waals crystals (fe1–xcox)5gete2. *arXiv: Mesoscale and Nanoscale Physics*, 2020.

[90] Hongrui Zhang, Yu Tsun Shao, R. Chen, Xiang Chen, Sandhya Susarla, David Raftrey, Jonathan T. Reichanadter, Lucas Caretta, Xiaoxi Huang, Nicholas S. Settineri, Zhen Chen, Jingcheng Zhou, Edith Bourret-Courchesne, Peter Ercius, Jie Yao, Peter Fischer, Jeffrey B. Neaton, David A. Muller, Robert J. Birgeneau, and Ramamoorthy Ramesh. A room temperature polar magnetic metal. *Physical Review Materials*, 2022.

[91] Erik Bauch, Connor A. Hart, Jennifer M. Schloss, Matthew J. Turner, John F. Barry, Pauli Kehayias, Swati Singh, and Ronald L. Walsworth. Ultralong Dephasing Times in Solid-State Spin Ensembles via Quantum Control. *Phys. Rev. X*, 8(3):031025, July 2018.

[92] Lucio Robledo, Hannes Bernien, Toeno van der Sar, and Ronald Hanson. Spin dynamics in the optical cycle of single nitrogen-vacancy centres in diamond. *New J. Phys.*, 13(2):025013, February 2011.

[93] Andrew Horsley, Patrick Appel, Janik Wolters, Jocelyn Achard, Alexandre Tallaire, Patrick Maletinsky, and Philipp Treutlein. Microwave Device Characterization Using a Widefield Diamond Microscope. *Phys. Rev. Appl.*, 10(4):044039, October 2018.

[94] Adam M. Wojciechowski, Mürsel Karadas, Alexander Huck, Christian Osterkamp, Steffen Jankuhn, Jan Meijer, Fedor Jelezko, and Ulrik L. Andersen. Contributed Review: Camera-limits for wide-field magnetic resonance imaging with a nitrogen-vacancy spin sensor. *Rev. Sci. Instrum.*, 89(3):031501., March 2018.

[95] Eduardo A. Lima and Benjamin P. Weiss. Obtaining vector magnetic field maps from single-component measurements of geological samples. *J. Geophys. Res. Solid Earth*, 114(B6), June 2009.

[96] D. Le Sage, K. Arai, D. R. Glenn, S. J. DeVience, L. M. Pham, L. Rahn-Lee, M. D. Lukin, A. Yacoby, A. Komeili, and R. L. Walsworth. Optical magnetic imaging of living cells. *Nature*, 496(7446):486–489, April 2013.

[97] Edlyn V. Levine, Matthew J. Turner, Pauli Kehayias, Connor A. Hart, Nicholas Langellier, Raisa Trubko, David R. Glenn, Roger R. Fu, and Ronald L. Walsworth. Principles and techniques of the quantum diamond microscope. *Nanophotonics*, 8(11):1945–1973, November 2019.

[98] Connor Hart. *Experimental Realization of Improved Magnetic Sensing and Imaging in Ensembles of Nitrogen Vacancy Centers in Diamond*. PhD thesis, September 2020.

[99] Matthew James Turner. *Quantum Diamond Microscopes for Biological Systems and Integrated Circuits*. PhD thesis, September 2020.

[100] M. L. Goldman, M. W. Doherty, A. Sipahigil, N. Y. Yao, S. D. Bennett, N. B. Manson, A. Kubanek, and M. D. Lukin. State-selective intersystem crossing in nitrogen-vacancy centers. *Phys. Rev. B*, 91(16):165201, April 2015.

[101] A. Batalov, V. Jacques, F. Kaiser, P. Siyushev, P. Neumann, L. J. Rogers, R. L. McMurtrie, N. B. Manson, F. Jelezko, and J. Wrachtrup. Low Temperature Studies of the Excited-State Structure of Negatively Charged Nitrogen-Vacancy Color Centers in Diamond. *Phys. Rev. Lett.*, 102(19):195506, May 2009.

[102] J.-P. Tetienne, L. Rondin, P. Spinicelli, M. Chipaux, T. Debuisschert, J.-F. Roch, and V. Jacques. Magnetic-field-dependent photodynamics of single NV defects in diamond: an application to qualitative all-optical magnetic imaging. *New J. Phys.*, 14(10):103033, October 2012.

[103] Jennifer May. Schloss. *Optimizing nitrogen-vacancy diamond magnetic sensors and imagers for broadband sensitivity*. PhD thesis, Massachusetts Institute of Technology, 2019.

[104] L. J. Rogers, S. Armstrong, M. J. Sellars, and N. B. Manson. Infrared emission of the NV centre in diamond: Zeeman and uniaxial stress studies. *New J. Phys.*, 10(10):103024, October 2008.

[105] V. M. Acosta, A. Jarmola, E. Bauch, and D. Budker. Optical properties of the nitrogen-vacancy singlet levels in diamond. *Phys. Rev. B*, 82(20):201202, November 2010.

[106] L. J. Rogers, M. W. Doherty, M. S. J. Barson, S. Onoda, T. Ohshima, and N. B. Manson. Singlet levels of the NV- centre in diamond. *New J. Phys.*, 17(1):013048, January 2015.

[107] Tse-Luen Wee, Yan-Kai Tzeng, Chau-Chung Han, Huan-Cheng Chang, Wunshain Fann, Jui-Hung Hsu, Kuan-Ming Chen, and Yueh-Chung Yu. Two-photon Excited Fluorescence of Nitrogen-Vacancy Centers in Proton-Irradiated Type Ib Diamond. *J. Phys. Chem. A*, 111(38):9379–9386, September 2007.

[108] Robert Chapman and Taras Plakhotnik. Quantitative luminescence microscopy on Nitrogen-Vacancy Centres in diamond: Saturation effects under pulsed excitation. *Chem. Phys. Lett.*, 507(1):190–194, April 2011.

[109] A. Dréau, M. Lesik, L. Rondin, P. Spinicelli, O. Arcizet, J.-F. Roch, and V. Jacques. Avoiding power broadening in optically detected magnetic resonance of single NV defects for enhanced dc magnetic field sensitivity. *Phys. Rev. B*, 84(19):195204, November 2011.

[110] M. W. Doherty, F. Dolde, H. Fedder, F. Jelezko, J. Wrachtrup, N. B. Manson, and L. C. L. Hollenberg. Theory of the ground-state spin of the NV^- center in diamond. *Phys. Rev. B*, 85(20):205203, May 2012.

[111] Marcus W. Doherty, Neil B. Manson, Paul Delaney, Fedor Jelezko, Jörg Wrachtrup, and Lloyd C. L. Hollenberg. The nitrogen-vacancy colour centre in diamond. *Phys. Rep.*, 528(1):1–45, July 2013.

[112] Chang S. Shin, Mark C. Butler, Hai-Jing Wang, Claudia E. Avalos, Scott J. Seltzer, Ren-Bao Liu, Alexander Pines, and Vikram S. Bajaj. Optically detected nuclear quadrupolar interaction of ^{14}N in nitrogen-vacancy centers in diamond. *Phys. Rev. B*, 89(20):205202, May 2014.

[113] V. M. Acosta, E. Bauch, M. P. Ledbetter, A. Waxman, L.-S. Bouchard, and D. Budker. Temperature Dependence of the Nitrogen-Vacancy Magnetic Resonance in Diamond. *Phys. Rev. Lett.*, 104(7):070801, February 2010.

[114] S. Felton, A. M. Edmonds, M. E. Newton, P. M. Martineau, D. Fisher, D. J. Twitchen, and J. M. Baker. Hyperfine interaction in the ground state of the negatively charged nitrogen vacancy center in diamond. *Phys. Rev. B*, 79(7):075203, February 2009.

[115] M. W. Doherty, V. M. Acosta, A. Jarmola, M. S. J. Barson, N. B. Manson, D. Budker, and L. C. L. Hollenberg. Temperature shifts of the resonances of the NV^- center in diamond. *Phys. Rev. B*, 90(4):041201, July 2014.

[116] F. Dolde, H. Fedder, M. W. Doherty, T. Nöbauer, F. Rempp, G. Balasubramanian, T. Wolf, F. Reinhard, L. C. L. Hollenberg, F. Jelezko, and J. Wrachtrup. Electric-field sensing using single diamond spins. *Nat. Phys.*, 7(6):459–463, June 2011.

[117] Eric Van Oort and Max Glasbeek. Electric-field-induced modulation of spin echoes of N-V centers in diamond. *Chem. Phys. Lett.*, 168(6):529–532, May 1990.

[118] V. M. Acosta, E. Bauch, M. P. Ledbetter, C. Santori, K.-M. C. Fu, P. E. Barclay, R. G. Beausoleil, H. Linget, J. F. Roch, F. Treussart, S. Chemerisov, W. Gawlik, and D. Budker. Diamonds with a high density of nitrogen-vacancy centers for magnetometry applications. *Phys. Rev. B*, 80(11):115202, September 2009.

[119] Janis Smits, Joshua T. Damron, Pauli Kehayias, Andrew F. McDowell, Nazanin Mosavian, Ilja Fescenko, Nathaniel Ristoff, Abdelghani Laraoui, Andrey Jarmola, and Victor M. Acosta. Two-dimensional nuclear magnetic resonance spectroscopy with a microfluidic diamond quantum sensor. *Sci. Adv.*, 5(7):eaaw7895., July 2019.

[120] Ed E. Kleinsasser, Matthew M. Stanfield, Jannel K. Q. Banks, Zhouyang Zhu, Wen-Di Li, Victor M. Acosta, Hideyuki Watanabe, Kohei M. Itoh, and Kai-Mei C. Fu. High density NV sensing surface created via He^(+) ion implantation of (12)^C diamond. *arXiv*, February 2016.

[121] Gopalakrishnan Balasubramanian, Philipp Neumann, Daniel Twitchen, Matthew Markham, Roman Kolesov, Norikazu Mizuochi, Junichi Isoya, Jocelyn Achard, Johannes Beck, Julia Tissler, Vincent Jacques, Philip R. Hemmer, Fedor Jelezko, and Jörg Wrachtrup. Ultralong spin coherence time in isotopically engineered diamond. *Nat. Mater.*, 8(5):383–387, May 2009.

[122] D. P. L. Aude Craik, P. Kehayias, A. S. Greenspon, X. Zhang, M. J. Turner, J. M. Schloss, E. Bauch, C. A. Hart, E. L. Hu, and R. L. Walsworth. Microwave-Assisted Spectroscopy Technique for Studying Charge State in Nitrogen-Vacancy Ensembles in Diamond. *Phys. Rev. Appl.*, 14(1):014009, July 2020.

[123] Boris Naydenov, Friedemann Reinhard, Anke Lämmle, V. Richter, Rafi Kalish, Ulrika F. S. D'Haenens-Johansson, Mark Newton, Fedor Jelezko, and Jörg Wrachtrup. Increasing the

coherence time of single electron spins in diamond by high temperature annealing. *arXiv*, December 2010.

[124] Hang Chen, Shahidul Asif, Kapildeb Dolui, Yang Wang, Jeyson Támara-Isaza, V. M. L. Durga Prasad Goli, Matthew Whalen, Xinhao Wang, Zhijie Chen, Huiqin Zhang, Kai Liu, Deep Jariwala, M. Benjamin Jungfleisch, Chitraleema Chakraborty, Andrew F. May, Michael A. McGuire, Branislav K. Nikolic, John Q. Xiao, and Mark J. H. Ku. Above-Room-Temperature Ferromagnetism in Thin van der Waals Flakes of Cobalt-Substituted Fe5GeTe2. *ACS Appl. Mater. Interfaces*, 15(2):3287–3296, January 2023.

[125] Andrew F. May, Dmitry Ovchinnikov, Qiang Zheng, Raphael Hermann, Stuart Calder, Bevin Huang, Zaiyao Fei, Yaohua Liu, Xiaodong Xu, and Michael A. McGuire. Ferromagnetism Near Room Temperature in the Cleavable van der Waals Crystal Fe5GeTe2. *ACS Nano*, 13(4):4436–4442, April 2019.

[126] Andrew F. May, Mao-Hua Du, Valentino R. Cooper, and Michael A. McGuire. Tuning magnetic order in the van der Waals metal Fe_5GeTe_2 by cobalt substitution. *Phys. Rev. Mater.*, 4(7):074008, July 2020.

[127] Andrew F. May, Craig A. Bridges, and Michael A. McGuire. Physical properties and thermal stability of $Fe_{5-x}GeTe_2$ single crystals. *Phys. Rev. Mater.*, 3(10):104401, October 2019.

[128] Hang Chen, Shahidul Asif, Matthew Whalen, Jeyson Támara-Isaza, Brennan Luetke, Yang Wang, Xinhao Wang, Millicent Ayako, Saurabh Lamsal, Andrew F. May, Michael A. McGuire, Chitraleema Chakraborty, John Q. Xiao, and Mark J. H. Ku. Revealing room temperature ferromagnetism in exfoliated Fe5GeTe2 flakes with quantum magnetic imaging. *2D Mater.*, 9(2):025017, March 2022.

[129] Arne Wickenbrock, Sarunas Jurgilas, Albert Dow, Luca Marmugi, and Ferruccio Renzoni. Magnetic induction tomography using an all-optical 87Rb atomic magnetometer. *Opt. Lett.*, 39(22):6367–6370, November 2014.

[130] Cameron Deans, Luca Marmugi, Sarah Hussain, and Ferruccio Renzoni. Electromagnetic induction imaging with a radio-frequency atomic magnetometer. *Appl. Phys. Lett.*, 108(10), March 2016.

[131] Yechezkel Schlussel, Till Lenz, Dominik Rohner, Yaniv Bar-Haim, Lykourgos Bougas, David Groswasser, Michael Kieschnick, Evgeny Rozenberg, Lucas Thiel, Amir Waxman, Jan Meijer, Patrick Maletinsky, Dmitry Budker, and Ron Folman. Wide-Field Imaging of Superconductor Vortices with Electron Spins in Diamond. *Phys. Rev. Appl.*, 10(3):034032, September 2018.

[132] L. Rondin, J.-P. Tetienne, P. Spinicelli, C. Dal Savio, K. Karrai, G. Dantelle, A. Thiaville, S. Rohart, J.-F. Roch, and V. Jacques. Nanoscale magnetic field mapping with a single spin scanning probe magnetometer. *Appl. Phys. Lett.*, 100(15), April 2012.

[133] David A. Broadway, James D. A. Wood, Liam T. Hall, Alastair Stacey, Matthew Markham, David A. Simpson, Jean-Philippe Tetienne, and Lloyd C. L. Hollenberg. Anticrossing Spin Dynamics of Diamond Nitrogen-Vacancy Centers and All-Optical Low-Frequency Magnetometry. *Phys. Rev. Appl.*, 6(6):064001, December 2016.

[134] Arne Wickenbrock, Huijie Zheng, Lykourgos Bougas, Nathan Leefer, Samer Afach, Andrey Jarmola, Victor M. Acosta, and Dmitry Budker. Microwave-free magnetometry with nitrogen-vacancy centers in diamond. *Appl. Phys. Lett.*, 109(5), August 2016.

[135] S. V. Anishchik and K. L. Ivanov. A method for simulating level anti-crossing spectra of diamond crystals containing NV- color centers. *J. Magn. Reson.*, 305:67–76, August 2019.

[136] Huijie Zheng, Zhiyin Sun, Georgios Chatzidrosos, Chen Zhang, Kazuo Nakamura, Hitoshi Sumiya, Takeshi Ohshima, Junichi Isoya, Jörg Wrachtrup, Arne Wickenbrock, and Dmitry Budker. Microwave-Free Vector Magnetometry with Nitrogen-Vacancy Centers along a Single Axis in Diamond. *Phys. Rev. Appl.*, 13(4):044023, April 2020.

[137] Reinis Lazda, Laima Busaite, Andris Berzins, Janis Smits, Florian Gahbauer, Marcis Auzinsh, Dmitry Budker, and Ruvin Ferber. Cross-relaxation studies with optically detected magnetic resonances in nitrogen-vacancy centers in diamond in external magnetic field. *Phys. Rev. B*, 103(13):134104, April 2021.

[138] C. Pellet-Mary, M. Perdriat, P. Huillery, and G. Hétet. Spin-Relaxation of Dipolar-Coupled Nitrogen-Vacancy Centers : The role of Double-flip Processes. *arXiv*, July 2022.

[139] Jean□Philippe Tetienne, Loïc Rondin, Piernicola Spinicelli, Mayeul Chipaux, Thierry Debuisschert, Jean-François Roch, and Vincent Jacques. Magnetic-field-dependent photodynamics of single nv defects in diamond: an application to qualitative all-optical magnetic imaging. *New Journal of Physics*, 14, 2012.

[140] Viktor Ivády, Huijie Zheng, Arne Wickenbrock, Lykourgos Bougas, Georgios Chatzidrosos, Kazuo Nakamura, Hitoshi Sumiya, Takeshi Ohshima, Junichi Isoya, Dmitry Budker, Igor A. Abrikosov, and Adam Gali. Photoluminescence at the ground-state level anticrossing of the nitrogen-vacancy center in diamond: A comprehensive study. *Phys. Rev. B*, 103(3):035307, January 2021.

[141] Marcis Auzinsh, Andris Berzins, Dmitry Budker, Laima Busaite, Ruvin Ferber, Florian Gahbauer, Reinis Lazda, Arne Wickenbrock, and Huijie Zheng. Hyperfine level structure in nitrogen-vacancy centers near the ground-state level anticrossing. *Phys. Rev. B*, 100(7):075204, August 2019.

[142] G. Kucsko, S. Choi, J. Choi, P. C. Maurer, H. Zhou, R. Landig, H. Sumiya, S. Onoda, J. Isoya, F. Jelezko, E. Demler, N. Y. Yao, and M. D. Lukin. Critical Thermalization of a Disordered Dipolar Spin System in Diamond. *Phys. Rev. Lett.*, 121(2):023601, July 2018.

[143] Omkar Dhungel, Till Lenz, Muhib Omar, Joseph Shaji Rebeirro, Viktor Ivady, Adam Gali, Arne Wickenbrock, and Dmitry Budker. Zero-field microwave-free magnetometry with ensembles of nitrogen-vacancy centers in diamond. *arXiv*, January 2023.

[144] Chul-Ho Lee, Gwan-Hyoung Lee, Arend M. van der Zande, Wenchao Chen, Yilei Li, Minyong Han, Xu Cui, Ghidewon Arefe, Colin Nuckolls, Tony F. Heinz, Jing Guo, James Hone, and Philip Kim. Atomically thin p–n junctions with van der Waals heterointerfaces. *Nat. Nanotechnol.*, 9(9):676–681, September 2014.

[145] J. Fransson, A. M. Black-Schaffer, and A. V. Balatsky. Magnon Dirac materials. *Phys. Rev. B*, 94(7):075401, August 2016.

[146] S. A. Owerre. A first theoretical realization of honeycomb topological magnon insulator. *J. Phys.: Condens. Matter*, 28(38):386001, July 2016.

[147] Oliver Gröning, Shiyong Wang, Xuelin Yao, Carlo A. Pignedoli, Gabriela Borin Barin, Colin Daniels, Andrew Cupo, Vincent Meunier, Xinliang Feng, Akimitsu Narita, Klaus Müllen, Pascal Ruffieux, and Roman Fasel. Engineering of robust topological quantum phases in graphene nanoribbons. *Nature*, 560(7717):209–213, August 2018.

[148] Motohiko Ezawa. Valley-polarized metals and quantum anomalous hall effect in silicene. *Phys. Rev. Lett.*, 109:055502, Aug 2012.

[149] L. Thiel, Z. Wang, M. A. Tschudin, D. Rohner, I. Gutiérrez-Lezama, N. Ubrig, M. Gibertini, E. Giannini, A. F. Morpurgo, and P. Maletinsky. Probing magnetism in 2D materials at the nanoscale with single-spin microscopy. *Science*, 364(6444):973–976, June 2019.

[150] David A. Simpson, Jean-Philippe Tetienne, Julia M. McCoey, Kumaravelu Ganesan, Liam T. Hall, Steven Petrou, Robert E. Scholten, and Lloyd C. L. Hollenberg. Magneto-optical imaging of thin magnetic films using spins in diamond. *Sci. Rep.*, 6(22797):1–8, March 2016.